Department of Precision and Microsystems Engineering

Tunable Magnets: Modeling and Validation for Dynamic and Precision Applications

S.G. Viëtor

Report no	: 2018.019
Coaches	: Dr. S.H. HosseinNia, Ir. J.W. Spronck
Specialisation	: Mechatronic System Design
Type of report	: Master Thesis
Date	: August 28, 2018

Delft University of Technology

Tunable Magnets

Modeling and Validation for Dynamic and Precision Applications

by

S.G. Viëtor

to obtain the degree of Master of Science

at the Delft University of Technology,

to be defended publicly on Tuesday August 28, 2018 at 13:00.

Student number:	4112679	
Project duration:	December 1, 2016 – August 28, 2018	
Thesis committee:	Ir. J.W. Spronck,	TU Delft, supervisor
	Dr. S.H. HosseinNia,	TU Delft, supervisor
	Dr. ir. Simone Baldi,	TU Delft
	Dr. ir. Winfred Mugge,	TU Delft

An electronic version of this thesis is available at `http://repository.tudelft.nl/`.

Summary

Actuator self-heating limits achievable force and can cause unwanted structural deformations that adversely affect the accuracy in precision actuation systems. This is especially apparent in quasi-static actuation systems that require a stable constant actuation force over an extended period. As a solution, we propose to use the concept of a Tunable Magnet (TM). TMs rely on in-situ magnetization state tuning of AlNiCo to create an infinitely adjustable magnetic flux. They consist of an AlNiCo permanent magnet together with a coil to create an external demagnetizing field. After tuning, the AlNiCo retains its magnetic field without further energy input. Therefore, TMs can eliminate static heat dissipation and improve general energy efficiency in actuators. A schematic of a TM actuator is shown in Fig. 1. Magnetization state tuning of AlNiCo has been used before by MIT (Electropermanent Magnets) and more recently by Carl Zeiss in an adjustable magnetic gravity compensator. However, both implementations make use of a lookup table to determine the correct magnetizing current at a single fixed air-gap. This method not robust against disturbances, and not viable to use in actuators. Predicting the correct magnetizing current is difficult, due to hysteresis and the complex non-linear relation between magnetizing current and magnet flux density.

In this thesis, a magnetization state tuning method is developed that can achieve robust magnetization state tuning in the presence of a varying actuator air-gap. This method consists of 3 steps. First, a desired operating point for the magnet is predicted using a magnetic circuit model of the actuator. This operating point yields the required actuator force at the required air-gap. Next, if the predicted magnetization is higher than the present value, the AlNiCo is saturated using a short but large current pulse. If the required magnetization is lower, the magnet is immediately demagnetized to the required value. The correct demagnetization current is generated using an air-gap flux feedback controller, with a set-point that is computed using hysteresis measurement data of the AlNiCo. Using a feedback controller ensures that the correct magnetization is always reached, even in the presence of external disturbances. The developed method is implemented in an experimental test setup, and measurements confirm its viability. A typical example of a tuning cycle starting at zero magnetization is shown in Fig. 2. With the obtained tuning accuracy and precision, actuator heating is already almost eliminated during static periods.

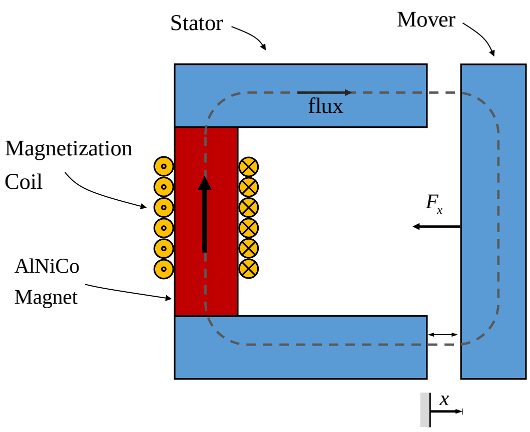

Figure 1: Tunable Magnet actuator.

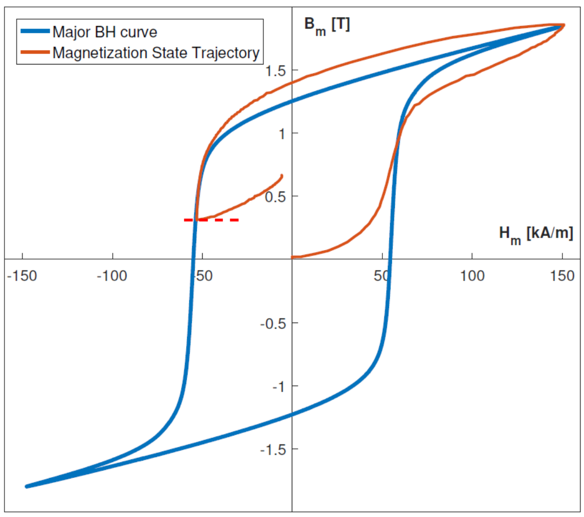

Figure 2: Typical magnetization state trajectory for a tuning cycle starting in zero magnetization

The second part of this thesis concerns the investigation of Tunable Magnets actuators. Using in-situ magnetization state tuning for actuation has the potential to improve energy efficiency, but there is a limit to the efficiency gain, depending on the application. To investigate this, a metric called the break-even tuning interval is derived. This is the time between magnetization tuning cycles, such that a tunable magnet actuator has the heat dissipation as a similar normal reluctance actuator, while generating the same force at an identical air-gap. Resulting from this analysis, are some recommendations for suitable TM actuator applications. Actuation systems where these actuators can improve energy efficiency can be characterized by a low actuation bandwidth or only incidentally required actuation, together with large air-gaps and/or large required constant bias forces. Also, scaling analysis shows that tunable magnet actuators are more energy efficient compared to conventional reluctance actuators at small length scales.

Contents

Summary iii

List of Figures vii

List of Tables xi

Glossary xiii
- List of Acronyms . . . xiii
- List of Symbols . . . xiv

1 Introduction 1
- 1.1 Motivation . . . 1
- 1.2 Prior Art . . . 2
- 1.3 Problem Definition . . . 3
- 1.4 Research Goal & Objectives . . . 5
- 1.5 Thesis Outline . . . 6

2 Tunable Magnets: Modeling and Validation for Dynamic and Precision Applications 7

3 Tunable Magnet Actuators: Break-Even Tuning Interval 21

4 Conclusions & Recommendations 31
- 4.1 Conclusions . . . 31
- 4.2 Towards the Realization of Tunable Magnet Actuators . . . 33
- 4.3 Recommendations for Future Work . . . 35

A DSPE Conference Paper 37

B Tunable Magnet Material Alternatives 43
- B.1 Introduction . . . 43
- B.2 Ideal Tunable Magnet Material . . . 43
- B.3 Experimental Results . . . 44
- B.4 Conclusion . . . 44

C Extended Literature Review 47
- C.1 Magnetic Clamping Applications . . . 47
- C.2 PM Motors and Gears . . . 49
- C.3 Magnetic Actuators . . . 50
- C.4 Determining Magnetization Current . . . 52
  - C.4.1 Switchable Magnets . . . 53
  - C.4.2 Tunable Magnets . . . 53
  - C.4.3 Conclusion . . . 55

D Measurement Setup Design 57
- D.1 Magnetic Circuit . . . 57
- D.2 Magnetizing Coil . . . 58
- D.3 Driving Electronics . . . 60
- D.4 Sensors and Signal Conditioning . . . 62

E Measurement Setup Specifications 65
- E.1 Setup Overview . . . 66
- E.2 Tunable Magnets . . . 67
- E.3 dSPACE RTI . . . 69
- E.4 Current Sensor . . . 69
- E.5 Magnetic Field Sensor Fixture . . . 71

E.6 Signal Conditioning 74
E.7 Linear Power Amplifier 76
E.8 H-bridge 78

F Modeling Hysteresis **79**
F.1 Preisach Model Derivation 79
F.2 Preisach Model Properties 82
F.3 Hui Implementation 83
F.4 Results & Conclusion 86
F.5 Matlab Code 87

G Model identification **93**
G.1 Model Identification in COMSOL 93
G.2 Parameter Sensitivity Study 96
G.3 Measurement Based Identification 99
G.4 Conclusion 101

H Recommended Literature **103**

I Material Data **105**
I.1 Steel 37 106
I.2 AlNiCo 107

Bibliography **111**

List of Figures

1 Tunable Magnet actuator. iii
2 Typical magnetization state trajectory for a tuning cycle starting in zero magnetization . iii

1.1 Tunable Magnet, consisting of an AlNiCo magnet and magnetizing coil, implemented in a gap closing reluctance actuator topology. 1
1.2 Example of a deformable mirror developed by [27] for adaptive optics in space. 2
1.3 ASML NXE3400 extreme UV lithography system. Shown in purple is the UV light being reflected by mirrors onto the wafer. 3
1.4 BH curve with load-lines and operating points that correspond to different air-gap widths l_g, under the influence of a field $H_{m,coil}$ imposed by a demagnetizing coil current. 4

4.1 Closed loop actuation system with a parallel combination of a TM actuator and a regular EM actuator. 33
4.2 Parallel combination of a TM actuator and a conventional actuator. 34

B.1 2nd quadrant BH-curves for several grades of AlNiCo. Data taken from [62]. 44
B.2 AlNiCo 6 TM measurement setup 45
B.3 AlNiCo 6 TM measurement setup response. Shown are the coil current I_c and air-gap flux B_g as a result of a sinusoidal input voltage 45

C.1 Electroperment Magnet (EPM) [26] 47
C.2 EPM working principle [26] 47
C.3 Holding force of the Electropermanent magnet as a function of the length of the 20V pulses used to switch the magnet [26]. 48
C.4 Robot designed by [38] that uses only AlNiCo magnets to provide adjustable clamping force. 49
C.5 Memory Motor with separate magnetization windings, as introduced by [64] 50
C.6 Linear magnetic gear with adjustable gear ratio, as introduced by [30] 50
C.7 Magnet unit consisting of an AlNiCo Magnet and magnetizing coil, from [40]. 51
C.8 Mirror mounted on flexures with magnet unit to facilitate vertical displacement adjustment, from [40]. 51
C.9 Wobble stepper motor based on EPMs, as proposed by [25] 51
C.10 EPM linear actuator, as proposed by [25]. 52
C.11 Magnetic gravity compensator based on soft electro-permanent magnets for adjustable reluctance force [17]. 52
C.12 Resulting force-displacement curves for different levels of magnetization of the AlNiCo magnet. 52
C.13 Measurement data from [36] to determine the magnetization pulse length and/or energy needed to achieve a required clamping force at a fixed air-gap. Initial magnetization before each measurement was stated as fully demagnetized. 54
C.14 Method of determining magnetization current as introduced by [63]. The parallelogram BH curve approximation is coupled to a magnetic FEM analysis of the motor topology to determine the magnetization look-up graph. 54
C.15 Back EMF waveform during flux weakening for the memory motor implementation of Fig. C.5, as simulated by [63]. 55
C.16 Magnetization and Demagnetization characteristics for the adjustable magnetic gravity compensator shown in Fig. C.11 [17]. 55

D.1 AlNico 5 TM measurement setup. Annotated are pole pieces [B] and mover [C]. 57

D.2 Schematic view of the TM reluctance actuator measurement setup. The magnetization coil is driven by a voltage source U_s and the current I_c is measured by a current sensor. Magnetic flux density in the air-gap is measured by a sense coil and a hall sensor. Denoted are the AlNICo magnet [A], the pole pieces [B] and mover [C]. 58
D.3 Cross section of magnetizing coil with AlNiCo PM. 59
D.4 Realized magnetizing coil and AlNiCo 5 PM 59
D.5 Design graph showing the relation between the number of coil turns, as well as the voltage and current required to produce a saturating MMF. Valid for the AlNiCo 5 TM actuator setup. 60
D.6 2nd quadrant major BH curve of AlNico 5 with maximum sensitivity line. Data from [7] . 61
D.7 Schematic of H-bridge with inductive load. Switches $S_1 - S_4$ are usually implemented using MOSFETs 62
D.8 An example H-bridge from Pololu [50], capable of supplying 21 A without a heatsink while being just $30 \times 33\text{mm}$. 62
D.9 Sensor fixture with hall sensor and sense coil. 63
D.10 Sensor fixture placed over pole face. 63

E.1 Overview of the TM measurement setup. 66
E.2 TM actuator with AlNiCo magnet and magnetizing coil. 67
E.3 dSPACE RTI unit. 69
E.4 Current Sensor 69
E.5 Current Sensor Schematics, designed by DEMO 70
E.6 Sensor fixture with hall sensor and sense coil 71
E.7 HE144 hall sensor calibration curve. 71
E.8 HE144 hall sensor datasheet, from [2]. 73
E.9 Signal Conditioning PCB. 74
E.10 Signal conditioning board schematics, designed by DEMO. 75
E.11 Linear Power Amplifier 76
E.12 Amplifier PCB Layout. Blue is the bottom layer and red the top layer. 76
E.13 OPA549 power amplifier schematics. 77
E.14 H-bridge from [50]. 78

F.1 *Preisach Hysteron*. Basic mathematical relay characterized by the thresholds α and β. The output v(t) is +1 if the input is larger then α and -1 if it is smaller than β. When the input is in range (β, α) the output remains unchanged. 80
F.2 Preisach hysteresis model described by a superposition of infinite hysterons, each weighted with Preisach density function $\mu(\alpha_n, \beta_n)$. The subscript n denotes that the thresholds belong to the n-th hysteron, with $n = 1 ... \infty$ 80
F.3 Effect of an monotonic increase of input $v(t)$ 81
F.4 Effect of a monotonic decrease of input $v(t)$ 81
F.5 Preisach plane with memory curve 81
F.6 Reversal point sequence that determines the state of the Preisach operator. Adapted from [3] 83
F.7 Wiping-out property illustrated. Adapted from [3] 83
F.8 Flow diagram of Preisach model implementation. Adapted from [19] 85
F.9 Measured AlNiCo 5 ascending and descending hysteresis curves from [7], fitted with (F.8). 86
F.10 AlNiCo 5 magnetization state trajectory (blue) for specified input signal. The model is initialized at zero magnetization, so it starts on the virgin BH curve (brown). 86
F.11 Simulink implementation of the Preisach model (basic overview). 87
F.12 Simulink implementation of the preisach model (details). 87

G.1 3D model with magnet and air-gap domains (marked in blue), used to evaluate flux and field values. 94
G.2 Slice plot of the 3D model after simulation with flux density distribution (color scale) and direction (arrows). 95
G.3 2D COMSOL model for parameter sensitivity study. 96
G.4 Sensitivity of k_1 on different parameters, specified in Fig. G.3 97

G.5 Sensitivity of k_2 on different parameters, specified in Fig. G.3 98
G.6 Estimated AlNiCo 5 hysteresis curves based on measurement data, for different values of k_1 and $k_2 = 1.09$. The reference curve is based on data taken from [7] 99
G.7 Estimated AlNiCo 5 hysteresis curves based on measurement data, for different values of k_2 and $k_1 = 2.44$. The reference curve is based on data taken from [7]. 100

I.1 St.37 magnetization curves from literature to evaluate μ_r [5, 20, 28, 29, 44] 106
I.2 AlNiCo material datasheet from [12]. 107
I.3 Demagnetization curves of AlNiCo 1 t/m 6. Data from [62]. 108
I.4 Demagnetization curves of AlNiCo 5a, 5b, 5c and 7 t/m 9. Data from [62]. 109

List of Tables

4.1 Tuning performance for AlNiCo 5 TM with $1\,\mathrm{mm} \leq l_g \leq 1.5\,\mathrm{mm}$. 33

C.1 Summary of the magnetization tuning methods used in prior research and their tuning performance. 55

D.1 AlNiCo 5 magnetizing coil dimensioning. 60
D.2 Sensor design requirements. 63

E.1 Test setup parameter values for the AlNiCo 5 TM. 67
E.2 Test setup parameter values for the AlNiCo 6 TM. 68
E.3 dSPACE hardware properties 69
E.4 Current Sensor properties 69
E.5 Magnetic field sensor properties. 71
E.6 Specifications of the channels on the signal conditioning board. Board power supply is max $\pm 15\,\mathrm{V}$. 74
E.7 Amplifier properties 76
E.8 H-bridge properties. 78

F.1 Identified coefficients of (F.8) for the ascending and descending AlNiCo 5 major BH curves. 85

G.1 COMSOL identification results. 95
G.2 Nominal values for parameters in sensitivity study. 96
G.3 Identified model coeffients 101

Glossary

List of Acronyms

TU	Technische Universiteit
PME	Precision and Microsystems Engineering
MSD	Mechatronic System Design
DSPE	Dutch Society for Precision Engineering
TM	Tunable Magnet
EM	Electromagnet
PM	Permanent Magnet
EPM	Electropermanent Magnet
MMF	Magnetomotive Force
EMF	Electromotive Force
BTI	Break-Even Tuning Interval
AlNiCo	Aluminium Nickel Cobalt
FEA	Finite Element Analysis
FEM	Finite Element Method
PPC	Power PC
MGC	Magnetic Gravity Compensator
PWM	Pulse Width Modulation
ADC	Analog to Digital Converter
DAC	Digital to Analog Converter
OpAmp	Operational Amplifier
RTI	Real Time Interface
DEMO	Dienst Elektrische en Mechanische Ontwikkeling (hardware support division TU Delft)
LPF	Low Pass Filter
PCB	Printer Circuit Board
VSM	Vibrating Sample Magnetometer

List of Symbols

Symbol	SI Unit	Name
α	-	upper threshold preisach hysteron
β	-	lower threshold preisach hysteron
γ	-	coil wire fill fraction
$\gamma_{\alpha,\beta}$		preisach hysteron function
η	-	efficiency
$\mu(\alpha,\beta)$		preisach density function
μ_0	$\mathrm{H\,m^{-1}}$	permeability of free space
μ_r	-	relative permeability
μ_{rec}	-	recoil permeability
ρ_c	$\Omega\,\mathrm{m}$	resistivity of copper
ρ_{al}	$\Omega\,\mathrm{m}$	resistivity of AlNiCo
σ	-	standard deviation
τ_m	s	magnetic diffusion time
ϕ_m	Wb	magnet flux
ϕ_g	Wb	air-gap flux
ω_c	$\mathrm{rad\,s^{-1}}$	crossover frequency
ω_{cl}	$\mathrm{rad\,s^{-1}}$	closed loop bandwidth
A_m	$\mathrm{m^2}$	magnet cross section
A_g	$\mathrm{m^2}$	air-gap cross section
A_w	$\mathrm{m^2}$	wire cross section
b_c	m	coil width
B_c	T	corner point flux density
B_g	T	air-gap flux density
B_g^{set}	T	air-gap flux density set-point
B_m	T	magnet flux density
B_o	T	magnet operating-point flux density
B_r	T	maximum remanent flux density
B_r'	T	intermediate remanent flux density
B_{sat}	T	saturation flux density
$C(s)$	-	controller
d_c	m	average coil diameter
$d_{contact}$	m	magnet-pole piece contact distance
d_{cm}	m	magnet position w.r.t. pole pieces
d_m	m	magnet diameter
d_w	m	wire diameter
E	J	energy
f	Hz	frequency
f_{bw}	Hz	bandwidth
f_{pwm}	Hz	PWM switching frequency
f_s	Hz	sampling frequency
f_{-3dB}	Hz	$-3\,\mathrm{dB}$ cut-off frequency
F_x	N	force in x direction
F_0	N	constant bias force
$\mathcal{F}_s$	AT	saturating MMF
$G(s)$	-	plant
G_0	-	DC gain

Symbol	SI Unit	Name
h_p	m	pole piece height
H_c	A m^{-1}	magnet coercivity
H_g	A m^{-1}	air-gap field intensity
h_k	m	mover height
H_m	A m^{-1}	magnet field intensity
H_o	A m^{-1}	magnet operating point field intensity
H_{sat}	A m^{-1}	saturation field intensity
I	A	current
I_c	A	coil current
ΔI_{pp}	A	peak-to-peak current noise
k_1	-	flux leakage coefficient
k_2	-	MMF loss factor
l_g	m	air-gap length
l_w	m	wire length
$L(s)$		loop gain
L	H	selft inductance
L_m	m	magnet length
L_k	m	mover length
L_p	m	pole piece length
N		coil number of turn
p_k		polynomial coefficients
P	J s^{-1}	power
P_+		region on preisach plane with positive hysterons
P_-		region on preisach plane with negative hysterons
R	Ω	resistance
t	s	time
T_{be}	s	*Break-Even Interval*
T_s	s	sampling period
$u(t)$	-	input preisach hysteron
U_{ADC}	V	analog to digital voltage range
U_s	V	power source voltage
ΔU_{pp}	V	peak-to-peak voltage noise
$v(t)$	-	output preisach hysteron
w_k	m	mover width
w_p	s	pole piece width

1

Introduction

1.1. Motivation

One of the challenges in modern precision actuation systems is thermal stability. Heat dissipated in the actuator coils limits the achievable force and can cause unwanted structural deformations [33] [17]. This is especially a concern in quasi-static actuation systems, where the actuator needs to maintain a stable and stationary position over an extended period. During this time, the actuator is still dissipating heat to produce a mostly static force.

Traditionally, the most widely used actuator for precision actuation was the Lorentz actuator, mainly due to its favorable linear relation between force and current. However, actuator self-heating is especially problematic for this type of actuator owing to its low force density. Advances in modern control techniques have allowed reluctance actuators, which have a non-linear force current relation, to be used as well. They have a force density of up to 10 times higher then Lorentz actuators [58]. The next development was the hybrid reluctance actuator [43], which combines high force density with a more linear response. This improvement in force predictability makes the hybrid reluctance actuator more suitable for implementation in systems where a high degree of precision is required. The linearization of the response is accomplished by a constant bias flux, supplied by one or more NdFeB permanent magnets in the actuator.

In this work, we propose a variation on the hybrid reluctance actuator called the *Tunable Magnet* (TM) actuator, where a low coercivity AlNiCo magnet replaces the NdFeB magnet. To vary the force, the

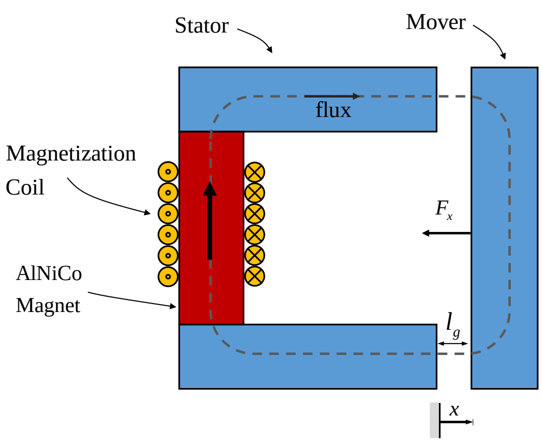

Figure 1.1: Tunable Magnet, consisting of an AlNiCo magnet and magnetizing coil, implemented in a gap closing reluctance actuator topology.

actuator coils are now only used to modify the magnetization of the AlNiCo, which acts as the main source of controllable magnetic flux. After magnetization, the AlNiCo retains its magnetic field without further energy input. TM actuators, therefore, have little to no heat dissipation during stationary periods. This concept has the potential to greatly increase energy efficiency, and thus decrease adverse thermal effects, in quasi-static actuation applications. Figure 1.1 shows the basic TM actuator implementation. It consists of an AlNico magnet with a magnetization coil, placed in simple gap-closing reluctance actuator topology.

Example Applications:

An example of a system where this can be beneficial is the deformable mirror used in adaptive optics for space applications [10]. It consists of a mirror (shown in Fig. 1.2a) of which an array of actuators controls the shape. Figure 1.2b shows the reluctance actuators currently used for this purpose. These adaptive optics systems can have a sampling period in the range from seconds up to months, during which time the actuator needs to maintain a position which is stable to within a dozen nanometers. Because the whole system is in space, the actuators have to operate in a vacuum, so convective cooling is impossible. This makes limiting the heat dissipation even more important.

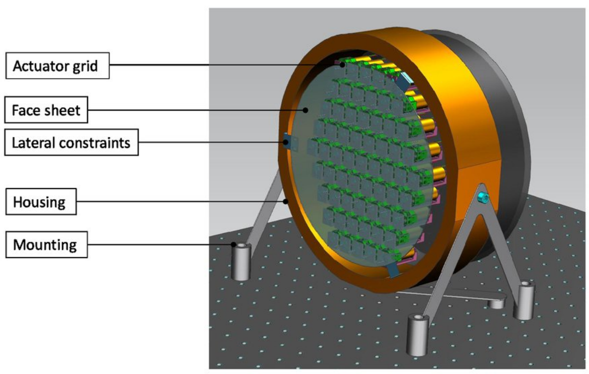

(a)

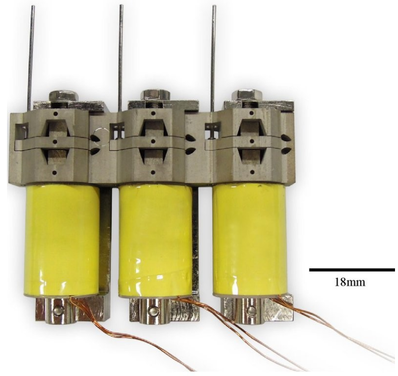

(b)

Figure 1.2: Example of a deformable mirror developed by [27] for adaptive optics in space.

Another quasi-static actuation application where thermal dissipation is a challenge is the alignment of optical components in lithographic projection machines. The EUV lithography machine from ASML which is shown in Fig. 1.3 uses extreme ultra-violet light to project a pattern onto a silicon wafer. The projection is done using a set of mirrors that guide the light from the source, over the reticle where it picks up a pattern, onto the wafer. Figure 1.3 shows the optical system in purple. Of paramount importance is the accuracy and stability of the mirrors. During wafer exposure, they have to be positioned with sub-nanometer precision [23]. The mirror alignment actuator, therefore, has to be highly stable and very precise. As with the previous example, this system is also in vacuum.

Both of these applications could potentially benefit from the implementation of an energy efficient TM actuator since they both require extreme stability and don't allow for convective cooling.

1.2. Prior Art

Using in-situ magnetization adjustment of AlNiCo has been the subject of prior research. In 2010, A.N. Knaian [26] introduced the Electropermanent Magnet (EMP) concept. It consists of an AlNiCo 5 magnet in parallel with a NdFeB magnet, together with a magnetizing coil. Changing the polarization of the low coercivity AlNiCo magnet with a pulsed external field effectively switches the magnet assembly 'On' and 'Off'. The main intended use of this concept is to provide a switchable, energy efficient magnetic connection. Devices that rely on in-situ tuning, as opposed to switching, of the magnetization of AlNiCo have been used for magnetic clamping [38] and flux weakening/boosting in electric motors [9, 46, 59, 64]. Recently a magnetic gravity compensator concept was investigated that uses magnetization state tuning to adjust the compensation force [17, 61]. Although it has been proposed to use magnetization

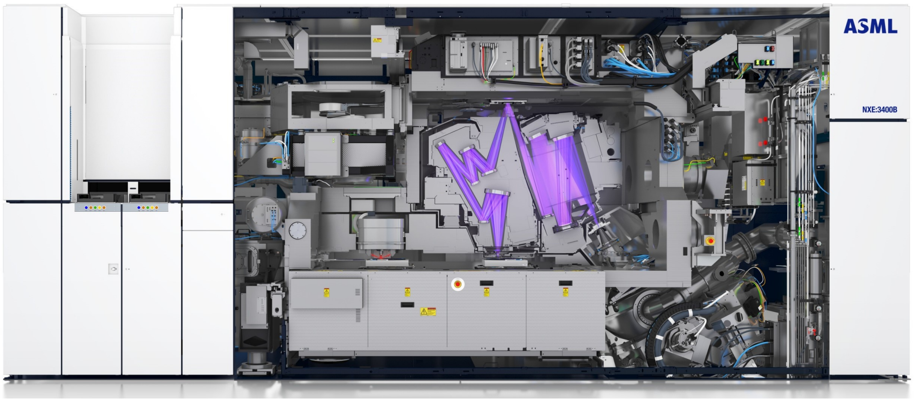

Figure 1.3: ASML NXE3400 extreme UV lithography system. Shown in purple is the UV light being reflected by mirrors onto the wafer.

state tuning for actuation [17, 25, 26, 40], other than the mentioned magnetic gravity compensator, none of these were actually implemented as far as public knowledge goes.

A more comprehensive review of prior research that makes use of in-situ magnetization state tuning of permanent magnets can be found in Appendix C.

1.3. Problem Definition

When it comes to magnetization tuning, the main challenge is to determine the necessary magnetizing current to reach a certain required remanent magnetization. The relation between current and resulting magnetization is very complex, involving non-linear magnetization curves and hysteresis.

Because of this complex relation, the required magnetization current depends on:

- the magnetization history
- the magnetic circuit reluctance

In prior research, several methods have been used to determine the correct magnetization current. Most implementations rely on lookup tables or curves determined either by magnetic FEA or measurements. In flux weakening/boosting applications, feedback is used in the form of motor back EMF that immediately shows the result of the magnet tuning. What they all have in common, however, is that the magnetization tuning is done at constant system reluctance. If a fixed starting magnetization is used (usually zero or saturation), only one measured or simulated characteristic magnetization curve is necessary for determining the correct magnetization current.

In actuation applications, however, the magnetic circuit reluctance is variable. Either by a changing air-gap in the case of a gap-closing type actuator or by a varying pole surface overlap, when a side drive actuator topology is used. To illustrate how the required magnetizing current changes with the TM actuator air-gap, the following example is considered.

Magnet Tuning Example:

Suppose we have the TM, as shown in Fig. 1.1, and want to change its magnetization by supplying a current through the coil. The coil generates a demagnetizing field in the magnet of $H_{m,coil}$. In addition, the presence of an air-gap in the magnetic circuit also imposes a demagnetizing field on the magnet, which we will denote by $H_{m,gap}$. The total demagnetizing field on the magnet is the summation of the two:

$$H_{demag} = H_{m,gap} + H_{m,coil} \tag{1.1}$$

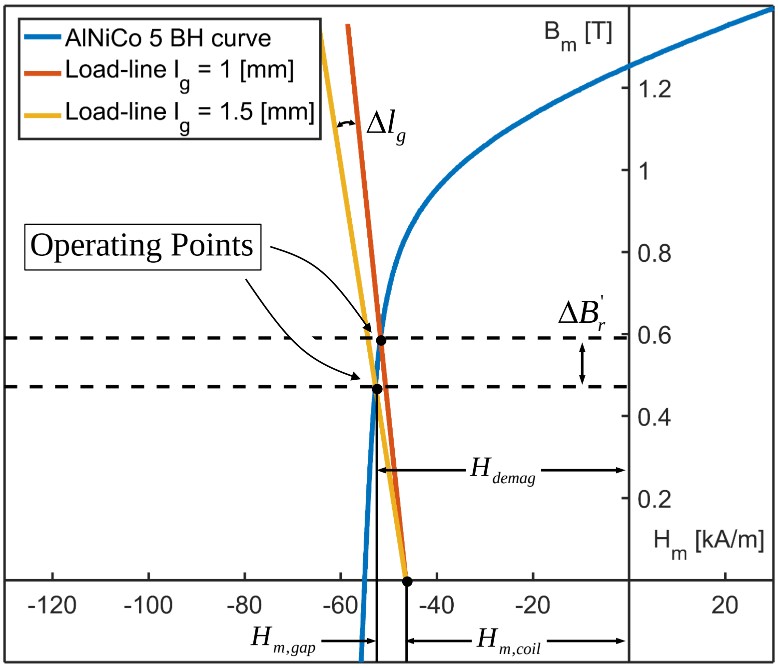

Figure 1.4: BH curve with load-lines and operating points that correspond to different air-gap widths l_g, under the influence of a field $H_{m,coil}$ imposed by a demagnetizing coil current.

This means that the air-gap width influences the total demagnetization resulting from a magnetizing coil current.

To determine how much this influence is, the BH curve of AlNiCo 5 (Fig.1.4) is considered, which shows these different demagnetization fields. The instantaneous magnetization of the AlNiCo is visually determined by the operating point, which is the point where the load-line intersects the major BH curve. Figure 1.4 shows two load-lines, corresponding to an air-gap of $l_g = 1$ mm and $l_g = 1.5$ mm. In general, an air-gap variation Δl_g affects the slope of the load-line, and an applied magnetizing current affects the position on the horizontal axis.

Comparing the operating points these two load-lines result in, it is clear that the acquired magnetization is significantly affected by the difference in air-gap. Demagnetizing the magnet with the same current, at two different air-gaps, varying Δl_g yields a difference in acquired magnetization of:

$$\Delta B_r' = 0.12\,\mathrm{T} \tag{1.2}$$

which comes down to $9.6\,\%$ of the remanent flux density of AlNICo 5 ($1.25\,\mathrm{T}$).

This example calculation shows that the air-gap, or in general the reluctance, of the magnetic circuit in which the TM is placed significantly influences the magnetization. When determining the magnetizing current, this effect cannot be neglected.

1.4. Research Goal & Objectives

In this thesis, the use of *Tunable Magnets* in precision actuation applications is proposed. It has the potential to increase energy efficiency and therefore decrease adverse thermal effects in quasi-static actuation applications.

The research goal of this thesis is stated as follows:

> *Develop a Tunable Magnet that can be robustly tuned in the presence of a dynamically varying air-gap, and investigate its use in precision actuation systems*

To achieve this, the following objectives are defined:

1. **Model the Tunable Magnet to gain insight into its behavior and for testing possible magnetization state tuning methods**
   The relation between magnetizing current and resulting magnetization is very complex. It involves non-linear magnetization curves and hysteresis. This behavior has to be understood thoroughly in order to come up with a magnetization state tuning method.
2. **Develop a method for robust magnetization state tuning under a dynamically varying air-gap**
   The biggest part of this work is the development of a magnetization state tuning method, with which the magnet can be robustly tuned in the presence of a dynamically varying air-gap.
3. **Investigate the implementation of Tunable Magnets in actuators and define in what type of applications they can improve energy efficiency**
   In-situ magnetization state tuning for actuation has been proposed but only implemented in one occasion [17], this means that there is almost no performance data available. Part of this work is, therefore, to investigate the implementation of TM actuators and define in what applications their use has merit.
4. **Build a prototype Tunable Magnet and validate the proposed tuning method**
   To validate the performance of the proposed magnetization state tuning method, a test setup with a prototype TM has to be built.

1.5. Thesis Outline

The most important part of the work I did is reported in the form of two scientific papers. The first paper (Chapter 2) goes into the details of the Tunable Magnet concept and presents the derivation and experimental validation of the magnetization state tuning method. A summarized version of this paper is submitted to the DSPE Conference on Precision Mechatronics 2018 (Appendix A). The second paper (Chapter 3) investigates the use of TMs in actuators and in what type of actuation applications they can improve energy efficiency. Chapter 4 summarizes the most important conclusion of both papers and gives an outlook on the realization of practical TM actuators.

Appendix B investigates potential alternatives for AlniCo 5 as a TM material. A thorough literature review of the state-of-the-art in applications using in-situ magnetization state tuning is presented in Appendix C. Appendix F describes the derivation and implementation of the Preisach hysteresis model mentioned in the paper in of Chapter 2. The identification of part of the magnetic circuit model used in the paper is described in detail in Appendix G. Appendices D and E report on the design and the complete specifications of the experimental setup used in this project. Appendix I contains the datasheet and demagnetization curves of several grades of AlNiCo and the soft steel (st. 37) used in the measurement setup.

Although the thesis describes and explains the necessary theory to understand the TM concept, interested readers may refer to Appendix H for a list of recommended literature. These books provide more details on several topics within the field of permanent magnets.

2

Tunable Magnets: Modeling and Validation for Dynamic and Precision Applications

This chapter has been written as a scientific paper. It describes the general concept of the Tunable Magnet and presents the derivation and experimental validation of the magnetization state tuning method. More information on the identification of the flux leakage coefficient and the MMF loss factor is described in Appendix G. The Preisach hysteresis model mentioned in the paper to simulate ferromagnetic hysteresis behavior is derived and implemented in Appendix F.

A condensed version of this paper (Appendix A), is submitted for the DSPE Conference on Precision Mechatronics, taking place 4 & 5 September in Sint Michielsgestel, The Netherlands.

Tunable Magnets: Modeling and Validation for Dynamic and Precision Applications

I. Introduction

One of the challenges in modern precision actuation systems is thermal stability. Heat dissipated in the actuator coils limits the achievable force and can cause unwanted structural deformations [1] [2]. This is especially a concern in quasi-static actuation systems, where the actuator needs to maintain a stable and stationary position over an extended period. During this time, the actuator is still dissipating heat to produce a largely static force.

Traditionally, the most widely used actuator for precision actuation was the Lorentz actuator, mainly due to its favorable linear relation between force and current. However, actuator self-heating is especially problematic for this type of actuator owing to its low force density. Advances in modern control techniques have allowed reluctance actuators, which have a non-linear force current relation, to be used as well. They have a force density of up to 10 times higher then Lorentz actuators [3]. The next development was the hybrid reluctance actuator [4], which combines high force density with a more linear response. This improvement in force predictability makes the hybrid reluctance actuator more suitable for implementation in systems where a high degree of precision is required. The linearization of the response is accomplished by a constant bias flux, supplied by one or more NdFeB permanent magnets in the actuator.

In this work, we propose a variation on the hybrid reluctance actuator called the *Tunable Magnet* actuator, where a low coercivity AlNiCo magnet replaces the NdFeB magnet. To vary the force, the actuator coils are now only used to modify the magnetization of the AlNiCo, which acts as the primary source of controllable magnetic flux. After magnetization, the AlNiCo retains its magnetic field without further energy input. TM actuators, therefore, have little to no heat dissipation during stationary periods. Possible application areas include; adjustable component mounts, magnetic gravity compensators [2], [5], highly stable microscope stages and adaptable-optics mirror actuators [6].

A. Prior Art

The idea of using in-situ magnetization adjustment of AlNiCo has been the subject of prior research. In 2010, A.N. Knaian [7] introduced the Electropermanent Magnet (EPM). It consists of an AlNiCo 5 magnet in parallel with a NdFeB magnet, together with a magnetizing coil. Changing the polarization of the low coercivity AlNiCo magnet with a pulsed external field effectively switches the magnet assembly On and Off. Devices that rely on in-situ tuning, as opposed to switching, of magnetization of AlNiCo have been realized for magnetic clamping applications [8], flux weakening/boosting in PM motors [9]–[12] and force tuning in a magnetic gravity compensator [2], [5].

The main challenge in implementing the TM concept is how to determine the correct coil current to tune the magnet to the desired strength. This magnetizing current depends on both the present magnetization and the reluctance of the magnetic circuit in which the TM is placed. For clamping applications, the air-gap width is usually constant, which simplifies the situation. In that case, the TM can be implemented using a single-input look-up table based on measurements for the magnetizing current. This is done by [7], [13]–[15]. In reluctance actuator applications, however, the circuit reluctance is variable by definition, either by a changing air-gap (gap-closing actuator) or a varying pole surface overlap (side drive actuator). In this case, the look-up table would need to have two inputs and extensive measurements at various starting magnetizations and system reluctances to implement. Some research has been done on trying to predict the magnetizing current using models or measurements. For example, [12] and [11] base their estimate on a parallelogram-shaped hysteresis curve approximation, combined with a simple magnetic circuit model. However, small deviations due to model inaccuracy and geometry tolerances can lead to substantial differences in resulting magnet strength, because the magnetization of the AlNiCo 5 magnet being used is very sensitive to variations in the applied field. Also, they do not give any results however on the precision and accuracy with which they achieve the magnetization tuning. To overcome this, [2] uses measurements of the AlNiCo BH characteristic to determine the magnetizing current. By entirely demagnetizing before each tuning step, only a single measured curve is needed, because the starting magnetization condition is always identical. This leads to good accuracy and repeatability at the fixed actuator position for which the system was calibrated. However, for a varying air-gap, this approach is not suitable.

B. Paper Contributions

This work aims to develop a TM that can be robustly tuned in the presence of a varying system reluctance, to enable implementation in actuation applications. We achieve this by introducing a magnetization state tuning method based on measurements of AlNiCo material properties, a magnetic circuit model, and air-gap flux feedback control.

The rest of this paper is organized as follows: In section II a model of the TM is derived, including a linearized version for controller design. In section III this model is used to develop the magnetization state tuning method. Part of this method is a demagnetization controller which is elaborated in section IV. The experimental setup and measurement results are reported in section V. Section 6 concludes on these results and gives an outlook on the use of TMs in precision actuation systems.

II. Modeling and Permanent Magnet Operation

This section investigates the behavior of permanent magnets in magnetic circuits. Based on this, a model of the TM, applied in an actuator, is derived. For control design purposes a linear model is also presented, which approximates the system behavior around a chosen operating point.

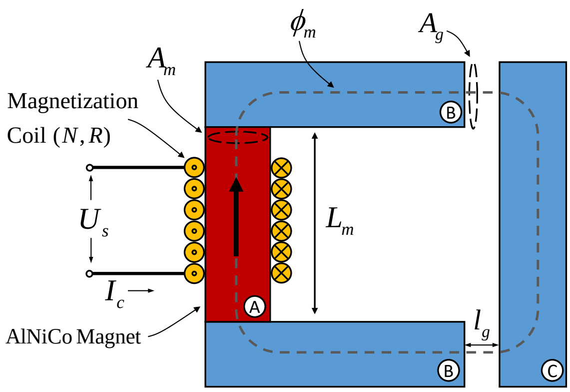

Fig. 1: Schematic of gap closing reluctance actuator with AlNiCo magnet [A] and soft steel pole pieces [B] and mover [C].

In this research, we assume that the TM is applied in a standard gap closing reluctance actuator topology, as shown in Fig 1. The system consists of the AlNiCo PM [A] with length L_m and cross-section A_m, with a magnetizing coil wrapped around it. The coil has N number of turns which carry a current I_c supplied by a voltage source U_s. The coil resistance is denoted by R. Soft steel pole pieces [B] with cross section A_g are on both sides of the magnet, and a soft steel mover [C] completes the magnetic circuit.

A. Magnetic circuit model with load-line

A lumped parameter model of the actuator can be derived by evaluating *Ampere's Circuit Law* over the flux path denoted by ϕ_m [16]:

$$H_m L_m + 2H_g l_g = NI \tag{1}$$

Where H_m and H_g are the magnetic field intensities in the magnet and the air-gaps. *Gauss's law* states conservation of flux throughout the magnetic circuit. It relates the magnetic flux density in the magnet B_m to that in the air-gap B_g as [16]:

$$B_m A_m = B_g A_g \tag{2}$$

The relation between B_g and H_g is given by:

$$B_g = \mu_0 H_g \tag{3}$$

Combining (1), (2) and (3) gives what is commonly known as a *load-line* [16]:

$$B_m = -\mu_0 \frac{A_g L_m}{2A_m l_g}\left(H_m - \frac{NI}{L_m}\right) \tag{4}$$

It relates the field intensity H_m in the magnet to the resulting magnetic flux density B_m. Another such relation is needed to determine the magnet's operating point. This is provided by the magnet's hysteresis characteristic, or BH-curve, shown in Fig. 2. The magnet operates at a point where the load-line intersects this curve. The angle of the load line only depends on the magnet and magnetic circuit geometry. Applying a current through the coil has the effect that the load-line is shifted over the horizontal axis. Both effects are depicted in Fig. 2. If the air-gap is brought to zero, the load-line becomes vertical and, if also no current is applied, the magnetic flux density is equal to the remanent flux B_r. In this state, the magnet is said to be short-circuited, since there is no reluctance in the magnetic circuit. In practice there are always small demagnetizing fields, so the magnet without magnetizing current can only operate in the 2nd or 4th quadrant of the BH-curve.

B. Magnet demagnetization

Figure 3 shows the so-called *knee-point* in the hysteresis characteristic, the point after which demagnetization becomes permanent. Suppose that the magnet is operating at point [a]. As mentioned before, a closing of the air-gap will move the operating point to B_r. Opening the air-gap again moves the operating point back to [a]. This is called a *reversible* change in magnetization. Next, the operating point is shifted to the left by applying a demagnetizing current through the coil such that the magnet operates at point [b]. If the current is removed, the load-line shifts back again, but the magnet's operating point will go to [c] instead of [a], since it has surpassed the knee point. The magnet is said to be *irreversibly* demagnetized and

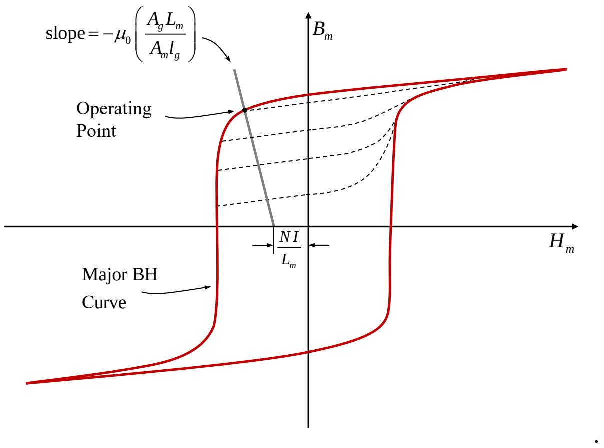

Fig. 2: AlNiCo major BH-curve with load-line. The magnet operates at a point where the load-line intersects the BH-curve. Adapted from: [17].

from then on will operate over a *recoil-line* with a different remanent flux density $B_r^{'}$.

Within the major BH-curve as, shown in Fig. 2, there exist a continuum of these recoil lines. Each of which constitutes a possible level of magnetization with its own remanent flux density. These recoil lines have a slope that is equal to the recoil permeability, given as a relative permeability μ_{rec}, which is a fundamental characteristic of the magnet [16].

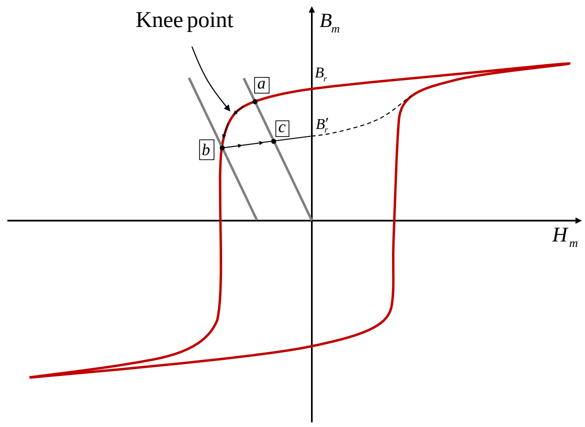

Fig. 3: AlNiCo BH-curve with load-line and knee-point, showing an irreversible demagnetization sequence [a][b][c].

C. Flux leakage and MMF loss coefficients (modeling non-idealities)

The above derived magnetic circuit model assumes that the flux is completely confined within the circuit elements and that there is no magnetization of the pole pieces or the mover. In reality though, there will be fringing and leakage fluxes, especially with large air-gaps, and some MMF loss due to the finite permeability of the circuit. To account for these effects, correction factors can be defined [16]:

$$k_1 = \frac{\text{magnet flux}}{\text{useful flux}} = \frac{A_m B_m}{A_g B_g} \tag{5}$$

$$k_2 = \frac{\text{magnet MMF}}{\text{useful MMF}} = \frac{H_m L_m}{2 H_g l_g} \tag{6}$$

Parameter k_1 is known as the *flux leakage coefficient* and is a measure of how much of the flux going through the magnet arrives in the air-gap as useful flux. Some authors use the inverse of k_1 as the *leakage factor* λ [4]. Parameter k_2 is the *MMF loss factor*, which accounts for the unwanted magnetization of the circuit components. It relates the total magnet MMF to the MMF that is used to establish a magnetic field in the air-gap.

Combing (4) with (5) and (6) gives the corrected load-line equation:

$$B_m = -\mu_0 \left(\frac{k_1}{k_2} \right) \frac{A_g L_m}{2 A_m l_g} \left(H_m - \frac{NI}{L_m} \right) \tag{7}$$

D. Non-linear simulation model

To get a better understanding of the behavior of TMs and to test the magnetization state tuning method, a full simulation model of the TM actuator of Fig. 1 is implemented. In the previous section, the relation between the magnetic field intensity and the flux density in the PM, $B_m = f(H_m)$, was evaluated graphically using a load-line and the BH-curve. This is a very convenient method for understanding the complex behavior of permanent magnets in magnetic circuits. For simulation purposes though, it is not a very suitable approach. To simulate the TM reluctance actuator, we use the *Hui* implementation [18] of the well-known *Preisach* ferromagnetic hysteresis model. Although more accurate implementations exist, the advantage of the *Hui* implementation is that it only requires measurement data of the major BH-curve to calibrate. Once calibrated it is also capable of simulating the traversal of recoil-lines. The use of the Preisach model allows us to solve (7) numerically, for example using Simulink [19]. A block diagram implementation is shown in Fig. 4.

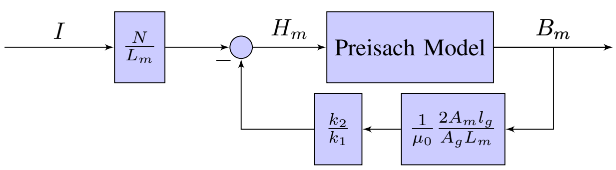

Fig. 4: Magnetic Model, block diagram implementation of (7)

The model in Fig. 4 relates the current through the magnetizing coil I_c to the flux density B_m. We can extend this by also considering the electrical behavior, modeling the effect of a voltage U_s on the flux density B_m.

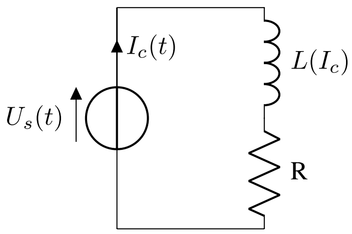

Fig. 5: Equivalent electric circuit of the TM reluctance actuator.

The equivalent electric circuit of the reluctance actuator is given by Fig. 5. The coil inductance $L(I)$ is nonlinear and depends on the magnetization of the AlNiCo and therefore the current I_c. Combining *Kirchoff's Voltage Law* and *Ohm's law* yields the electric behavior of the system:

$$U_s = I_c R + A_m N \frac{dB_m}{dt} \tag{8}$$

Using the magnetic model from Fig. 4, the electrical model (8) can be solved numerically using the block diagram implementation in Fig. 6.

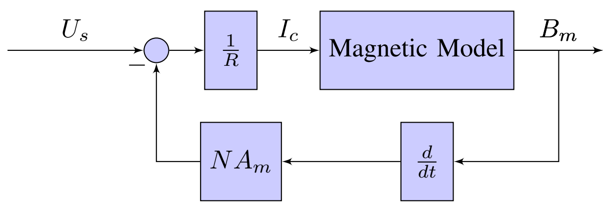

Fig. 6: Electric model, block diagram implementation solving (8)

E. Linear Model

For a better understanding of the system's dynamics and to design a controller it is helpful to derive a linear model of the system. To do this, the BH relation inside the AlNiCo magnet is modeled as:

$$B_m = H_m \mu_0 \mu_r(H_m) \tag{9}$$

Where $\mu_0\mu_r(H_m)$ is the magnet's permeability, expressed as a relative permeability, which is equal to the slope of hysteresis characteristic describing $B_m = f(H_m)$. This relative permeability varies with H_m, but writing it like this allows the evaluation of linearized system dynamics around specific operating points.

Combining (7) and (9) and simplifying $\mu_r(H_m)$ to μ_r for readability yields:

$$B_m = \frac{NI_c}{A_m}\left(\frac{k_2}{k_1}\frac{2l_g}{\mu_0 A_g} + \frac{L_m}{A_m\mu_0\mu_r}\right)^{-1} \tag{10}$$

Next, (10) is written explicit for I_c and substituted in (8) to get to the following differential equation:

$$U_s = B_m A_m \left[\frac{R}{N}\left(\frac{k_2}{k_1}\frac{2l_g}{\mu_0 A_g} + \frac{L_m}{A_m\mu_0\mu_r}\right) + N\frac{dB_m}{dt}\right] \tag{11}$$

Taking the Laplace transform of (11) gives the transfer function from the applied voltage U_s to the flux density in the magnet B_m:

$$G(s) = \frac{B_m(s)}{U_s(s)} = G_0 \frac{1}{\frac{L}{R}s + 1} \tag{12}$$

where G_0 is the DC gain of the system and L the linearized coil inductance. Note that this relation is only valid for a constant air-gap l_g, since it ignores the motion back-EMF. The DC gain and self inductance are given by:

$$G_0 = \frac{\frac{N}{A_m}}{R\left(\frac{k_2}{k_1}\frac{2l_g}{A_g\mu_0} + \frac{L_m}{A_m\mu_0\mu_r}\right)} \tag{13}$$

$$L = N^2\left[\left(\frac{k_1}{k_2}\frac{A_g\mu_0}{2l_g}\right)^{-1} + \left(\frac{A_m\mu_0\mu_r}{L_m}\right)^{-1}\right]^{-1} \tag{14}$$

The inductance can be seen as a parallel combination of the inductance resulting from the AlNiCo core and the inductance caused by the magnetic circuit reluctance.

F. Magnetization dynamics

Until now it was assumed that an applied H_m instantaneously produced the expected B_m inside the magnetic material. In reality though, this process is governed by a time constant called the *Magnetic Diffusion Time* [20]. It is defined as the time required for the magnetic flux density B_m, inside every point of the magnet, to rise to at least 63% of the steady-state value. This time constant is caused by induced eddy current effects that limit the speed at which the applied magnetic field H_m diffuses into the magnet. Figure 7 schematically shows this process, where the externally applied field H_0 only exists at the surface at t_1 and is fully diffused into the magnet at t_4. An estimate of this time constant is given by [21], for a simplified 'step' hysteresis characteristic with a maximum flux density B_{sat}:

$$\tau_m = \frac{d_m^2 B_{sat}}{16\rho_{al} H_{sat}} \tag{15}$$

where H_{sat} is the applied saturating field to reach B_{sat}. The diameter and the electrical resistivity of the AlNiCo are denoted by d_m and ρ_{al} respectively.

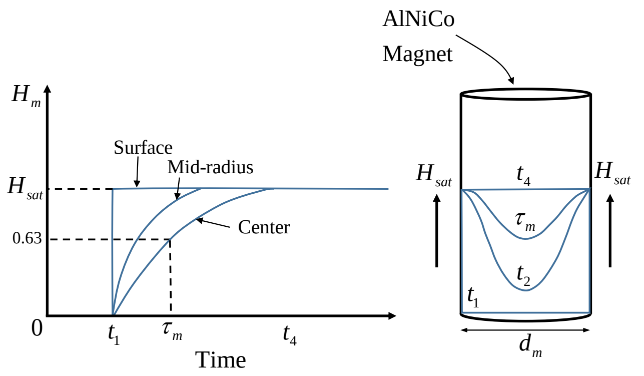

Fig. 7: Visualization of an applied field H_0 diffusing into a cylindrical, to illustrate magnetic diffusion time τ. Adapted from [22]

The significance of τ_m for the TM is that it gives a maximum speed at which the magnet can be tuned. The magnetic field has to be diffused into to entire material volume in order to modify the magnetization. One of the manifestations of this magnetization time constant is the effect of loop-widening [19]. An example of this phenomenon can be seen in the measurement results in Fig. 19. Most of the magnetization state trajectory followed during this tuning cycle is not equal to the statically measured major BH curve. The extra H-field that 'widens' the BH curve, is produced by the induced eddy-currents inside the AlNiCo and the other electrically conductive magnetic circuit components.

III. Magnetization State Tuning Method

The previous section elaborated on modeling the TM. This section introduces a magnetization state tuning method based on this model. We assume that the air-gap of l_g the TM actuator from Fig. 1 is variable but accurately known. This is often the case for an actuator, where the position of the mover is measured to be used in motion feedback control. The proposed tuning process is visualized in Fig. 8. It can be summarized as follows: if a new level of air-gap flux density B_g^{set} is required the system predicts at what recoil-line the magnet needs to operate to achieve this for a given air-gap width l_g. If this recoil-line is higher than the present one, the magnet is saturated by a saturating voltage pulse on the coil. If not, the magnet is immediately tuned to the correct recoil line, where a demagnetization controller generates the required voltage. The reason for completely saturating the magnet is twofold. Demagnetizing from saturation ensures that the operating point always follows the same curve in the 2nd quadrant. This way only one curve needs to be accurately measured beforehand to determine the correct demagnetization controller set-point. If not properly saturated, the material is demagnetized over a different minor loop curve, leading to tuning errors. See Sec. V for examples of this. Another advantage of the proposed method is magnetization stability. If demagnetized from saturation, the most sensitive magnetic domains will rotate first, leaving only the more stable domains. The resulting magnetization state is, therefore, more robust against settling of the domains that can lead to slight demagnetization over time [22]

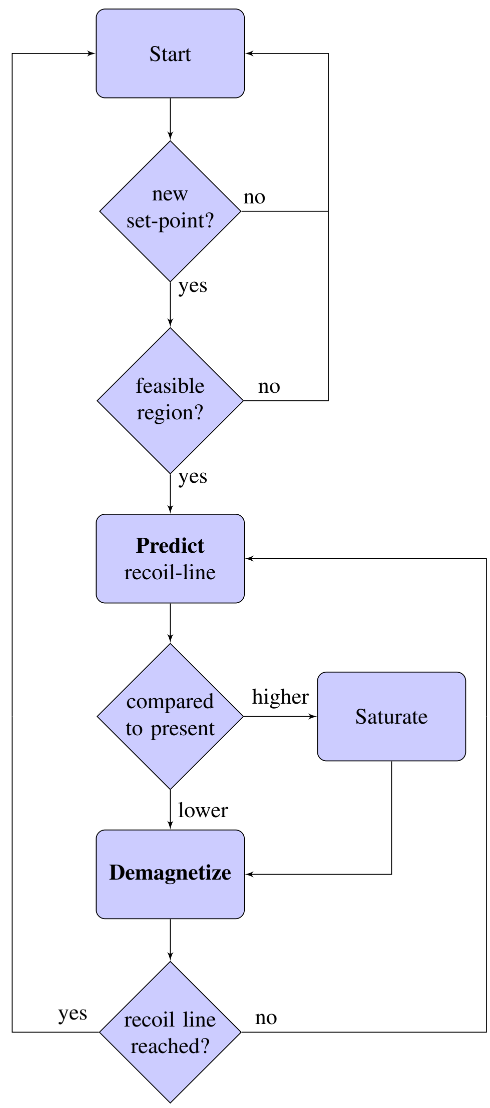

Fig. 8: Magnetization state tuning algorithm

A. Predict recoil-line

The level of magnetization that can be supported by the magnet without an additional magnetizing current is visualized by the feasible region in Fig. 9. It is dependant on the system reluctance and thus the slope of the load-line. The region is bounded above by the recoil line with remanence $B_{r,max}$ that starts at the point of intersection between the major BH curve and the load-line starting in the origin.

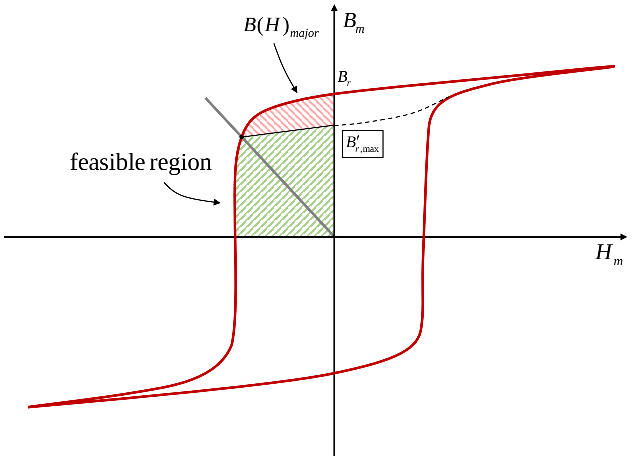

Fig. 9: BH curve showing recoil line that separates feasible from in-feasible region for given load-line

The point (H_o, B_o) where the magnet has to operate to yield a certain required air-gap flux density B_g^{set} is calculated using (3), (5) and (6):

$$B_o = k_1 \frac{A_g}{A_m} B_g^{set} \tag{16}$$

$$H_o = -k_2 \frac{2\, l_g}{L_m} \frac{B_g^{set}}{\mu_0} \tag{17}$$

Figure 10 shows this operating point on with the associated recoil-line. The recoil-line is identified by remanent magnetization $B'_{r,i}$, which can be determined by:

$$B'_{r,i} = B_o - \mu_{rec} H_o \tag{18}$$

B. Saturate

If the required operating recoil-line is higher than the one where the magnet is currently operating on, the AlNiCo is first saturated using a current pulse through the coil. The required current can be calculated by replacing B_m and H_m in (7) with saturation values H_{sat} and $B_{sat} = B_r + \mu_0 H_{sat}$. This yields the expression for the saturation current in terms of system parameters:

$$I_{max} = \frac{L_m}{N} \left[H_{sat} + 2 \left(\frac{k_2}{k_1} \right) \left(\frac{B_r}{\mu_0} + H_{sat} \right) \frac{A_m}{A_g} \frac{l_g}{L_m} \right] \tag{19}$$

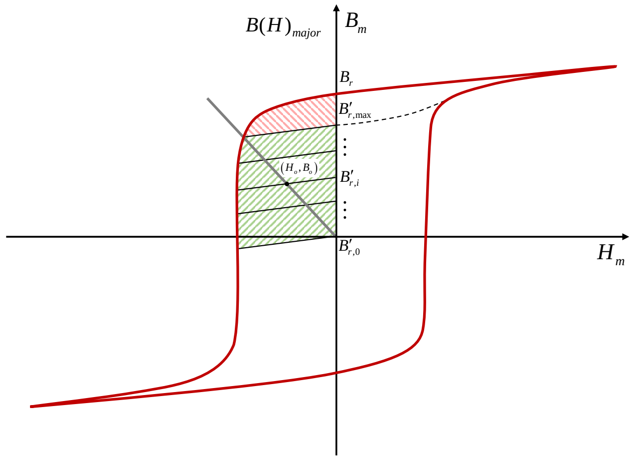

Fig. 10: BH curve with a collection of recoil lines, identified by their respective recoil permeabilities $B'_{r,i}$, together with a load-line and operating point (H_o, B_o)

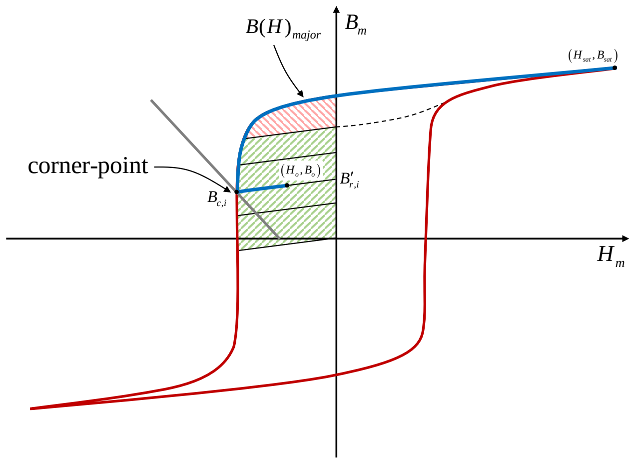

Fig. 11: Example magnetization state trajectory from (H_{sat}, B_{sat}) to (H_o, B_o)

C. Demagnetize

During demagnetization, the operating point is shifted over the major BH curve in the 2nd quadrant. The demagnetization controller reference is, therefore, corner-point $B_{c,i}$, i.e., the point where the desired recoil line intersects the major hysteresis loop. Demagnetizing to this point guarantees subsequent operation over the correct recoil line. This is illustrated in Fig. 11, where the blue line indicates the trajectory followed by the operating point from saturation (H_{sat}, B_{sat}), over the major BH-curve, to corner-point $B_{c,i}$. Next, the controller is switched off, and the current decays to zero. This causes the operating point to arrive at (H_o, B_o) on the recoil line identified by $B'_{r,i}$.

The next section covers the design of the demagnetization controller.

IV. Controller design

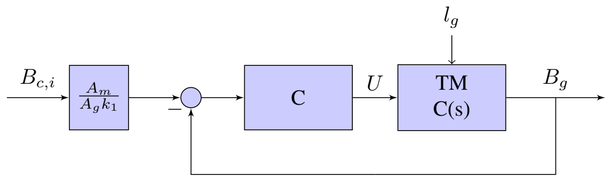

Fig. 12: Tuning Controller

The demagnetizing controller proposed in this paper is a simple air-gap flux feedback controller, with a structure as shown in Fig. 12. The reference input $B_{c,i}$ is first translated to the corresponding air-gap flux density value using (5).

The reason for using feedback control instead of feed-forward is increased robustness. As already mentioned, small disturbances or uncertainties in the model parameters or BH data can have a significant effect on the final magnetization state. Also, in actuation applications, the air-gap will change during the tuning cycle. This can be seen as a disturbance entering the system, which the controller should reject and still arrive at the correct magnetization.

As derived earlier, the TM implemented in a gap closing reluctance actuator topology will behave like coil with a nonlinear core. Its inductance being dependent on the AlNiCo permeability and the air-gap width:

$$G(s) = \frac{B_m(s)}{U(s)} = \frac{G_0(\mu_r, l_g)}{\frac{L(\mu, l_g)}{R}s + 1} \tag{20}$$

During tuning the relative permeability varies between 1 and $\mu_{r,max}$ as the state transitions from saturation to the correct corner point: $1 \leq \mu_r \leq \mu_0\mu_{r,max}$ This varying permeability manifests itself as a non-constant plant gain that the controller has to be able to handle, while still having a good performance.

Since demagnetization along the major BH curve is irreversible, it is imperative that the controlled system has zero overshoot. Otherwise, the correct corner-point is passed, and the magnet will end up operating on the wrong recoil-line. This also requires the step response to have zero steady state error.

A. Inverse-based controller

For control design, we consider a simple inverse based approach [23], since our plant is invertible. The following loop shape fulfills the demands on the step response characteristics:

$$L(s) = G(s)C(s) = \frac{\omega_c}{s} \tag{21}$$

where $G(s)$ is the plant as defined in (20) and $C(s)$ the controller. The closed-loop system bandwidth is equal to the crossover frequency ω_c. It provides high gain at low frequencies to remove the steady-state error and has a phase-margin of 90° that results in a damped step-response without overshoot.

The corresponding controller can be written as:

$$C(s) = \frac{\omega_c}{s} G^{-1}(\mu_r, l_g)(s) \tag{22}$$

To bias the controlled system towards stability in the presence of a varying plant gain, we use the maximum permeability value μ_{max} for the design, giving L_{max} and $G_{0,max}$ as model parameters. Actual values for these parameters, based on the AlNiCo 5 TM experimental setup (Tab.II) are given in Tab. I.

TABLE I: Tuning controller parameters for AlNiCo 5 TM experimental setup (Sec. V)

Parameter	Value	Comment
ω_c	$550\,\mathrm{rad\,s^{-1}}$	Controller bandwidth
$G_{0,max}$	$0.268\,\mathrm{T\,V^{-1}}$	Max system DC-gain
L_{max}	$48.6\,\mathrm{mH}$	Max coil self-inductance
R	$3.5\,\Omega$	Coil resistance

The resulting controller then has the following form:

$$C(s) = \frac{\omega_c}{s} G_{0,max} \left(\frac{L_{max}}{R} s + 1 \right) \tag{23}$$

We set the closed-loop bandwidth, defined by the crossover frequency ω_c to $550\,\mathrm{rad\,s^{-1}}$. The maximum achievable control bandwidth is limited by the available coil supply voltage and hardware sampling rate.

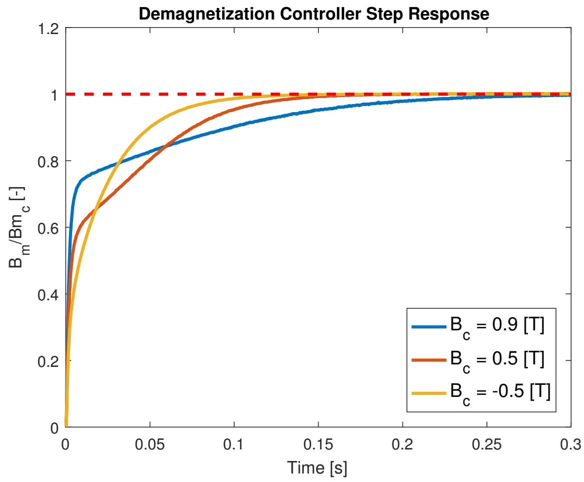

Fig. 13: Measured step responses of AlNiCo 5 TM with designed controller (23) for different set-points B_c.

Figure 13 shows typical measured step responses of the controlled system for different set-point values B_c, based on the

AlNiCo 5 TM experimental setup (Sec. V). Their difference in shape is due to the non-linear nature of the system. However, they all have the desired damped response with negligible steady-state error, so the controller performance is good.

V. Hardware Implementation

In this section, we present the hardware implementation of the Tunable Magnet.

A. Hardware Design

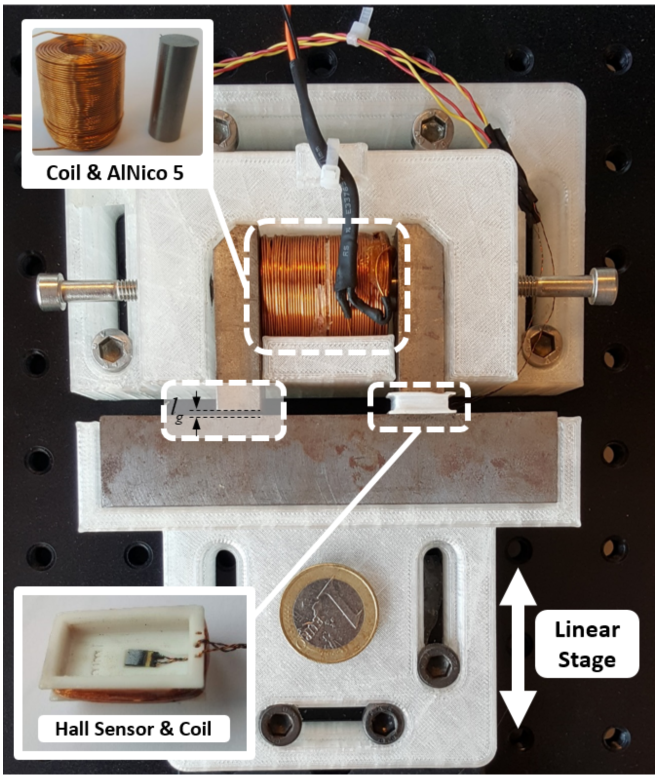

Fig. 14: AlNico 5 experimental setup with TM and sensor fixture

The experimental setup consists of a reluctance actuator topology, similar to Fig. 1 with a fixed 1 mm nominal air-gap as shown in Fig. 14. The pole pieces and mover are machined from soft steel (st. 37) and placed in 3D printed fixtures. The pole-pieces are then clamped to the TM by screws. The fixture for the mover is mounted a ThorLabs manual linear precision stages with a resolution of 10 µm [24] in order to vary the air-gap width. We measure air-gap flux density using an Asensor technology HE144 hall sensor [25] together with a sense coil to capture both DC and AC values accurately. Both are placed in the air-gap using a sensor fixture as shown in Fig. 14. The sensor fixture has a thickness of 1 mm and accurately fixes the nominal air-gap width. For the sense coil, magnetic flux density is determined by integrating the induced voltage, $U_{sense} = N_s \frac{dB_g}{dt}$, where N_s is the number of copper turns. We determine the current by measuring the voltage drop over a sense resistor. All sensor signals are amplified by instrumentation amplifiers and then low-pass filtered at 3 kHz to avoid aliasing. Interfacing the signals with the computer and implementing the tuning algorithm is done using a dSPACE [26] 1005 PPC real-time controller, sampling at 10 kHz.

TABLE II: Test setup parameter values for the AlNiCo 5 TM

AlNiCo 5 Test Setup Parameters			
Symbol	Value	Comment	Source
AlNiCo 5 magnet		Other names: LNG44, Alcomax 3	
L_m	$30.20\,\mathrm{mm}$	Magnet length	
d_m	$9.83\,\mathrm{mm}$	Magnet diameter	
B_r	$1.25\,\mathrm{T}$	Remanent flux density	[27]
H_c	$50\,\mathrm{kA\,m^{-1}}$	Coercive force	[27]
H_{sat}	$150\,\mathrm{kA\,m^{-1}}$	Saturation field intensity	
$\mu_{r,max}$	270	Maximum relative permeability	[17]
ρ	$4.75 \times 10^{-7}\,\Omega\,\mathrm{m}$	Electrical resistivity	[27]
Coil			
N	668	Number of coil windings	
R	$3.5\,\Omega$	Coil resistance	
Magnetic Circuit			
A_g	$200\,\mathrm{mm}^2$	Air-gap surface	
l_g	$1.00\,\mathrm{mm}$	Nominal air-gap width	
$\mu_{r,avg}$	1000	Average relative permeability St. 37	

TABLE III: Non-ideal model coefficient values, determined using COMSOL and experimental verification

Coefficient	COMSOL	Experimental
AlNiCo 5 setup		
k_1	2.68	2.44
k_2	1.09	1.09

The magnetization coils are dimensioned using (19) such that they can generate sufficient MMF to saturate the AlNiCo magnet. The current to the coils is provided by a TI OPA549 linear-power amplifier, capable of supplying up to 10 Amperes with 30 Volts, which is enough to create a saturating magnetic field. The complete specifications of the measurement setup can be found in Tab. II.

VI. Experimental Results

Using the TM experimental setup described in the last section, the magnetization state tuning method proposed in this paper is experimentally verified.

A. Model identification

In order to use the earlier derived magnetic circuit model, we first need to identify coefficients k_1 and k_2. This is done using magnetic FEA in COMSOL, with a detailed 3D model of the TM actuator. Using (5) and (6) this yields the values shown in Tab. III under COMSOL.

The major BH curve is determined by using a 0.5 Hz input voltage signal on the coil and taking the cyclic average of the

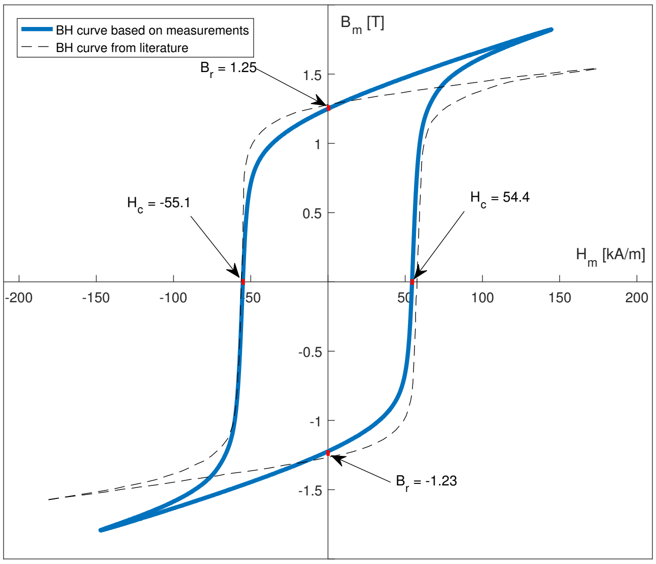

Fig. 15: Estimate of AlNiCo 5 major BH curve using measurements of B_g and I_c together with (5) (6). Also shown is a reference characteristic from literature [17]

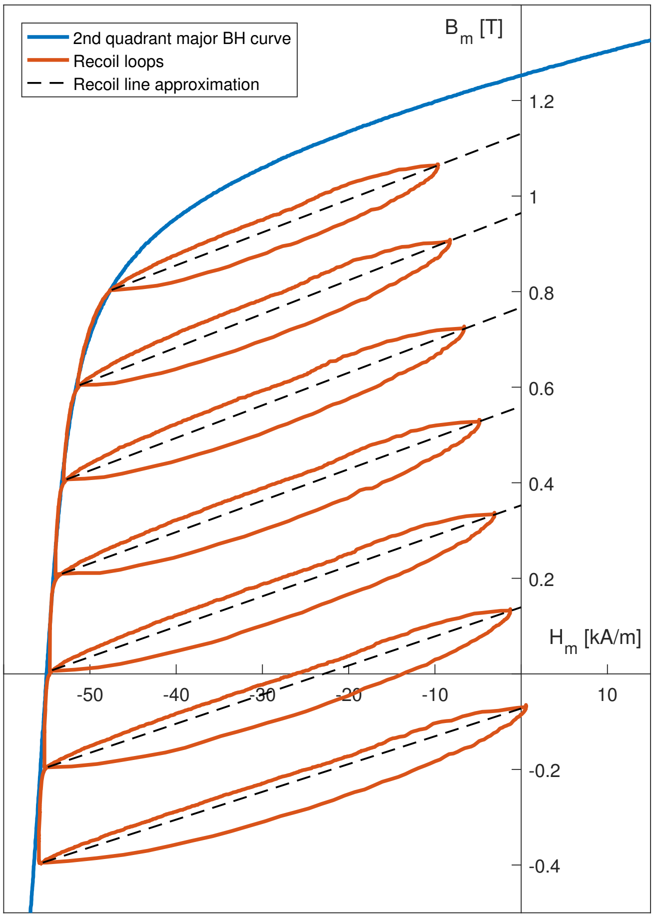

Fig. 16: Measured recoil loops and their line approximation in the 2nd quadrant of the AlNiCo 5 BH Curve.

measured current and gap flux density. The identified magnetic circuit model is then used to estimate H_m and B_m. The identified value of k_1, however, does not yield the expected value for the remanence flux B_r for AlNiCo 5 according. A sensitivity analysis shows that it is susceptible to changes in air-gap, so a slight mismatch between the simulation and the physical setup can cause a large difference. To complete the model identification, k_1 is modified such that the resulting BH curve shows approximately the correct remanent magnetization B_r, as shown in Fig. 15.

Note that the estimated major loop is quite steep towards positive and negative saturation and does not match the reference curve from literature. This can be attributed to the limited accuracy of the magnetic circuit model used to estimate H_m and B_m. The tuning accuracy is not influenced, however, as long as the hysteresis characteristic is identified with the same system as used for the magnetization state tuning.

B. Recoil-line measurements

Using the calibrated model, we can now characterize the complete BH-curve, including recoil lines. This data is then used to implement the magnetization state tuning method.

Figure 16 shows the fully populated BH-curve for AlNiCo 5. Note that the earlier described recoil-lines are actually small loops, of which the recoil permeability μ_{rec} and the associated remanence $B_r^{'}$ can be approximated by connecting corners with a straight line.

Figure 17 shows measurements of the recoil permeability μ_{rec} for recoil loops at different positions in the 2nd quadrant of the BH curve. The position is defined by the remanent magnetization $B_r^{'}$ associated with the recoil loop in question, i.e., the point where the line approximation crosses the vertical axis. As seen in the figure, the recoil-line distribution has a distinctive shape that can be approximated with a 10th order polynomial:

$$\mu_{rec} = \sum_{k=0}^{10} p_k B_r^k \qquad (24)$$

where p_k are the polynomial coefficients. This relation is only valid over the range shown in Fig. 17.

C. Magnetization State Tuning

Combining (18) and (24) and solving numerically for $B_r^{'}$ gives the required magnetization level for a desired B_g^{set}. Intersecting the associated recoil-line (18) with the estimated major BH curve, gives the corner-point and demagnetization controller reference input B_c. This visualized in Fig. 18 for an air-gap of $l_g = 1\,\mathrm{mm}$ and a range of air-gap flux density set-points B_g^{set} as denoted in Tab. IV. This table also

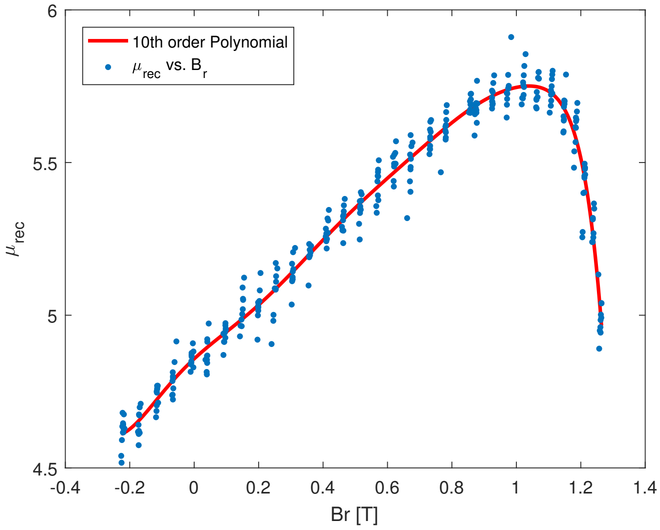

Fig. 17: Distribution of permeabilities μ_{rec}, for recoil-loops at different remanent magnetizations $B_r^{'}$ in the 2nd quadrant. Approximated by a 10th order polynomial.

TABLE IV: Air-gap flux density set-points B_g^{set} with associated recoil-line parameters ($B_r^{'}$, μ_{rec}) and the corner points B_c that serve as demagnetization controller set points. These values correspond to the recoil lines in Fig. 18

$B_g^{set}[T]$	$B_c[T]$	$\mu_{rec}[-]$	$B_r^{'}[T]$
0.175	0.889	5.537	1.195
0.150	0.659	5.750	1.027
0.125	0.479	5.674	0.855
0.100	0.310	5.526	0.683
0.075	0.144	5.363	0.511
0.050	-0.018	5.180	0.340
0.025	-0.181	5.006	0.170
0.000	-0.343	4.857	0.000

shows the corresponding recoil line parameters μ_{rec}, $B_r^{'}$ and demagnetization controller set-points B_c needed to reach the respective recoil-lines.

The Magnetization State Tuning algorithm is programmed on a dSPACE real-time interface using code compiled from Simulink [28]. The demagnetization controller set-points are pre-programmed. In a real application though, they will need to be determined in real-time, based on a prediction of the required actuator force.

Figures 19, 20 and 21 show the air-gap flux density B_g over time together with the corresponding magnetization state trajectory in terms of H_m and B_m, for three different air-gap widths l_g. Starting from $B \approx 0\,\mathrm{T}$, the magnet is driven to saturation B_{sat} and demagnetized to the correct corner-point B_c. When the coil voltage is removed, the current decays and the magnetization approaches the desired operating point B^{set}.

Note that in the case of $l_g = 1.2\,\mathrm{mm}$ and $l_g = 1.5\,\mathrm{mm}$, the system is not able to saturate to magnet to the same state

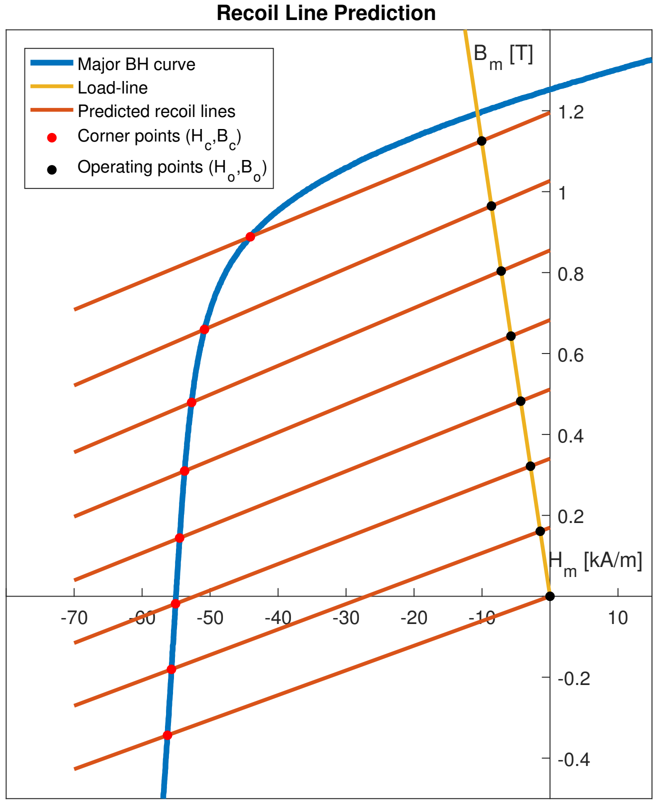

Fig. 18: Predicted operating points (air-gap width $l_g = 1\,\mathrm{mm}$) and the recoil-lines they are on, for the air-gap flux density set-points $B_{g,i}^{set}$ noted in Tab. IV. These recoil-lines intersect the major BH curve at corner-points $B_{c,i}$

as for $l_g = 1\,\mathrm{mm}$. This is due to a limitation in the power supply. It does not have the voltage capacity to generate the necessary magnetizing current through the coil. The result is that for these larger air-gaps the magnet operating point follows a different curve during demagnetization It arrives at the correct B_c, but with a different value for H_m. Because of this, a slightly different recoil-loop is reached, giving an error in the resulting air-gap flux B_g.

To evaluate the robustness of the TM implementation, we recorded 50 tuning cycles for each B_g^{set}, at the three different air-gap widths. Tables V, VI and V show the achieved accuracy, in terms of the MAE (mean absolute error), and the precision (3σ).

Comparing the general results for all air-gaps, we see that the error increases with increasing l_g. This is because of the earlier explained error caused by insufficient saturation current, but also due to the limited accuracy of the used magnetic circuit model. For example, the flux leakage and fringing effects will increase with increasing air-gap, i.e., (5) is air-gap dependent. The more the air-gap deviates from the nominal value at which the model was identified ($l_g = 1\,\mathrm{mm}$), the larger the operating point prediction error and consequently the tuning

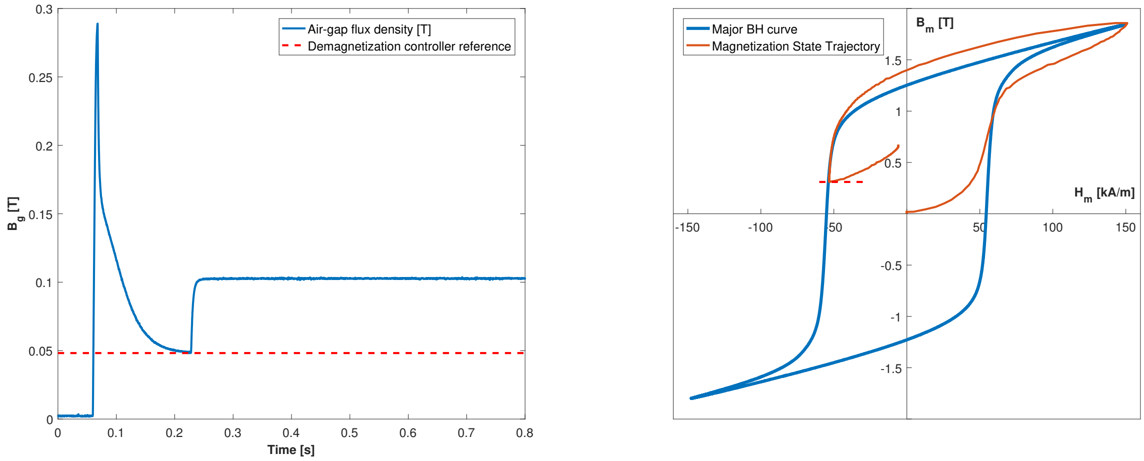

Fig. 19: Tuning cycle with $l_g = 1\,\mathrm{mm}$ and $B_g^{set} = 0.1\,\mathrm{T}$. Shown are the time response of the air gap flux density B_g and the associated magnetization state trajectory.

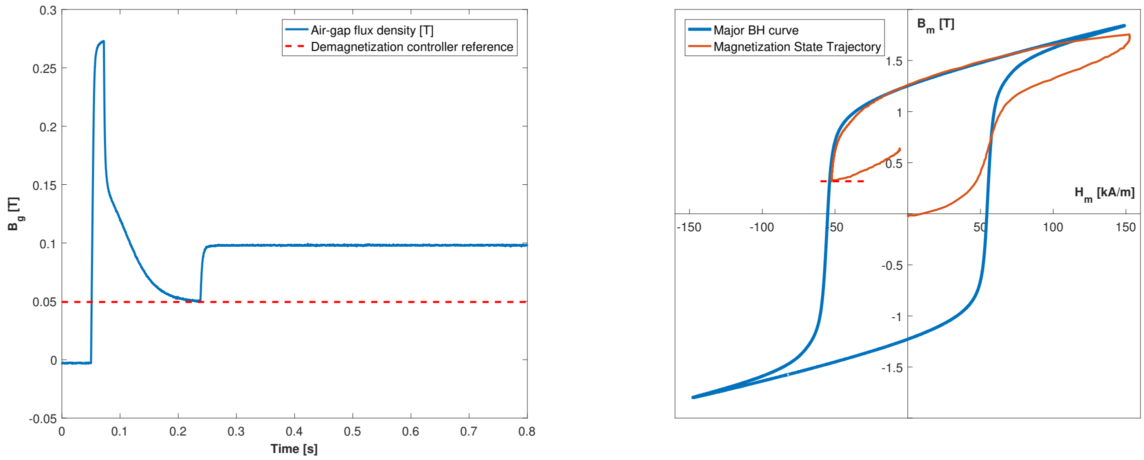

Fig. 20: Tuning cycle with $l_g = 1.2\,\mathrm{mm}$ and $B_g^{set} = 0.1\,\mathrm{T}$. Shown are the time response of the air gap flux density B_g and the associated magnetization state trajectory.

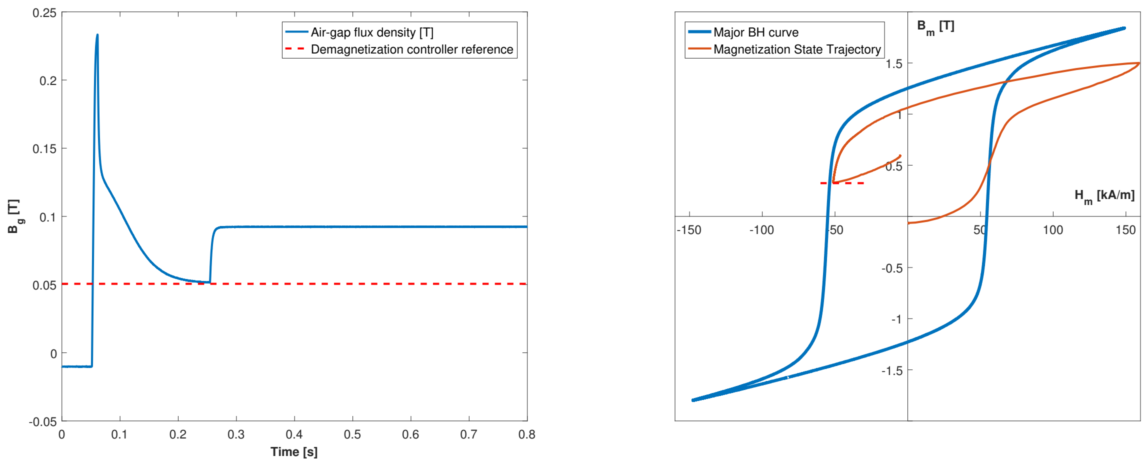

Fig. 21: Tuning cycle with $l_g = 1.5\,\mathrm{mm}$ and $B_g^{set} = 0.1\,\mathrm{T}$. Shown are the time response of the air gap flux density B_g and the associated magnetization state trajectory.

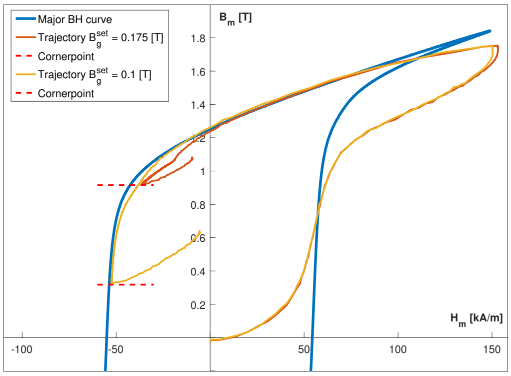

Fig. 22: Magnetization state trajectories for tuning cycles with $l_g = 1.2\,\mathrm{mm}$. Comparing different set-points B_g^{set}.

error. In addition to these effects, the real air-gap width is also uncertain, since it is not measured. This also contributes to the tuning error. How much of the error is associated with each of these error sources cannot be determined from these measurements.

For each air-gap, the error at $B_g^{set} = 0.175\,\mathrm{T}$ is relatively large compared to the error at other set-points. These outliers can be explained by a combination between the insufficient saturation current and the loop widening effect. Figure 22 compares the magnetization state trajectories for $B_g^{set} = 0.175\,\mathrm{T}$ and $B_g^{set} = 0.1\,\mathrm{T}$ at an air-gap of $l_g = 1.2\,\mathrm{mm}$. Carefully examining the curves shows that the trajectory for $B_g^{set} = 0.175\,\mathrm{T}$ converges quicker to the static version of the minor loop it is demagnetizing over. Therefore, when reaching the corner-point value of the magnet flux density, i.e. $B_m = B_c$, it enters a different recoil-line than predicted. Because of the loop widening effect, the trajectory for $B_g^{set} = 0.1\,\mathrm{T}$ remains closer to the static major BH curve. Therfore, the resulting recoil-line, while still slightly off, is closer to the predicted recoil-line. To state it differently, the loop widening effect offsets the error introduced by having insufficient saturation current, but it does so better for the lower magnetization set-points.

The precision values, do not seem to change for different values of the air-gap. This suggests that the precision is only determined by the noise in the control system.

For the current implementation of the magnetization state tuning method, tuning times in the order of $500\,\mathrm{ms}$ are achieved, depending on the set-point chosen. For a TM in an actuator generally holds that the faster the magnetization state can be tuned the better. Faster tuning means that the tuning process itself causes less of a disturbance on the system it is actuating. Also, the faster the magnetization, the lower the energy dissipation in the coil due to resistive losses. Tuning speed can be increased by increasing the bandwidth of the demagnetizing controller (23). Ultimately, however, it is limited by the magnetic diffusion time constant (15) as explained in Sec. II.

TABLE V: Tuning performance results over $n = 50$ tuning cycles for each B_g^{set} and $l_g = 1\,\mathrm{mm}$

B_g^{set}	Realized Values		$l_g = 1.00\,\mathrm{mm}$
	Mean	Error	Repeatability (3σ)
$0.175\,\mathrm{T}$	$0.178\,\mathrm{T}$	$2.87\,\mathrm{mT}$	$0.42\,\mathrm{mT}$
$0.150\,\mathrm{T}$	$0.152\,\mathrm{T}$	$2.40\,\mathrm{mT}$	$0.67\,\mathrm{mT}$
$0.125\,\mathrm{T}$	$0.128\,\mathrm{T}$	$2.52\,\mathrm{mT}$	$0.61\,\mathrm{mT}$
$0.100\,\mathrm{T}$	$0.103\,\mathrm{T}$	$2.86\,\mathrm{mT}$	$1.07\,\mathrm{mT}$
$0.075\,\mathrm{T}$	$0.078\,\mathrm{T}$	$3.12\,\mathrm{mT}$	$1.17\,\mathrm{mT}$
$0.050\,\mathrm{T}$	$0.053\,\mathrm{T}$	$3.16\,\mathrm{mT}$	$1.08\,\mathrm{mT}$
$0.025\,\mathrm{T}$	$0.028\,\mathrm{T}$	$2.88\,\mathrm{mT}$	$1.12\,\mathrm{mT}$
$0.000\,\mathrm{T}$	$0.003\,\mathrm{T}$	$2.59\,\mathrm{mT}$	$1.08\,\mathrm{mT}$

TABLE VI: Tuning performance results over $n = 50$ tuning cycles for each B_g^{set} and $l_g = 1.2\,\mathrm{mm}$

B_g^{set}	Realized Values		$l_g = 1.20\,\mathrm{mm}$
	Mean	Error	Repeatability (3σ)
$0.175\,\mathrm{T}$	$0.168\,\mathrm{T}$	$7.47\,\mathrm{mT}$	$0.60\,\mathrm{mT}$
$0.150\,\mathrm{T}$	$0.147\,\mathrm{T}$	$3.01\,\mathrm{mT}$	$0.88\,\mathrm{mT}$
$0.125\,\mathrm{T}$	$0.123\,\mathrm{T}$	$2.15\,\mathrm{mT}$	$0.98\,\mathrm{mT}$
$0.100\,\mathrm{T}$	$0.098\,\mathrm{T}$	$1.74\,\mathrm{mT}$	$1.27\,\mathrm{mT}$
$0.075\,\mathrm{T}$	$0.073\,\mathrm{T}$	$1.94\,\mathrm{mT}$	$0.93\,\mathrm{mT}$
$0.050\,\mathrm{T}$	$0.047\,\mathrm{T}$	$2.79\,\mathrm{mT}$	$0.42\,\mathrm{mT}$
$0.025\,\mathrm{T}$	$0.022\,\mathrm{T}$	$3.19\,\mathrm{mT}$	$0.34\,\mathrm{mT}$
$0.000\,\mathrm{T}$	$-0.004\,\mathrm{T}$	$3.68\,\mathrm{mT}$	$0.34\,\mathrm{mT}$

VII. Conclusion

In this paper, we have presented a way of implementing a Tunable Magnet, which enables it to be used in actuation applications. It was shown that robust magnetization state tuning for a variable but known air-gap could be achieved. This is accomplished by predicting the right operating point for the AlNiCo 5 PM, based on measured BH data and a magnetic circuit model. An air-gap flux feedback controller is then used to generate the demagnetizing current such that the magnet approaches this operating point. If necessary, the magnet is saturated first.

Using this method we have achieved magnetization state tuning with a maximum error of $25.35\,\mathrm{mT}$ and a minimum repeatability of $1.27\,\mathrm{mT}$, for air-gap flux density set-points in the range of $0\,\mathrm{T} \leq B_g^{set} \leq 0.175\,\mathrm{T}$. This was done for air-gaps in the range of $1\,\mathrm{mm} \leq l_g \leq 1.5\,\mathrm{mm}$. Part of the tuning error is due to insufficient saturation current because of the limited power supply voltage. Selecting a better power amplifier will already improve this. Another error source is the limited accuracy of the magnetic circuit model used in the operating point prediction.

With the tuning results achieved in this research, actuator heating during static periods is already almost eliminated. Only a small bias current is needed to compensate for the tuning error.

TABLE VII: Tuning performance results over $n = 50$ tuning cycles for each B_g^{set} and $l_g = 1.5\,\mathrm{mm}$

B_g^{set}	Realized Values		$l_g = 1.5\,\mathrm{mm}$
	Mean	Error	Repeatability (3σ)
$0.175\,\mathrm{T}$	$0.150\,\mathrm{T}$	$25.35\,\mathrm{mT}$	$0.49\,\mathrm{mT}$
$0.150\,\mathrm{T}$	$0.138\,\mathrm{T}$	$11.86\,\mathrm{mT}$	$0.29\,\mathrm{mT}$
$0.125\,\mathrm{T}$	$0.117\,\mathrm{T}$	$8.19\,\mathrm{mT}$	$0.35\,\mathrm{mT}$
$0.100\,\mathrm{T}$	$0.092\,\mathrm{T}$	$7.61\,\mathrm{mT}$	$0.36\,\mathrm{mT}$
$0.075\,\mathrm{T}$	$0.067\,\mathrm{T}$	$7.91\,\mathrm{mT}$	$0.37\,\mathrm{mT}$
$0.050\,\mathrm{T}$	$0.042\,\mathrm{T}$	$8.34\,\mathrm{mT}$	$0.35\,\mathrm{mT}$
$0.025\,\mathrm{T}$	$0.016\,\mathrm{T}$	$8.89\,\mathrm{mT}$	$0.31\,\mathrm{mT}$
$0.000\,\mathrm{T}$	$-0.010\,\mathrm{T}$	$9.85\,\mathrm{mT}$	$0.36\,\mathrm{mT}$

Tuning times are in the order of $500\,\mathrm{ms}$ per cycle but can be decreased by modifying the demagnetization controller. Ultimately though, the tuning speed is limited by the magnetization dynamics of the AlNiCo PM used.

Future work includes improving the tuning speed of the magnet for more versatile applicability and improving the accuracy of the model to account for air-gap dependencies. This will enable reliable tuning over a greater range of motion. To enable the use of *Tunable Magnets* in actuation applications, the robustness of the proposed magnetization state tuning method needs to be evaluated in a real actuator where the air-gap can vary during the tuning cycle. Also, the type of applications where TM actuators can improve energy efficiency needs to be better defined.

REFERENCES

[1] E. A. Lomonova, "Advanced Actuation Systems -State of the Art: Fundamental and Applied Research," in *International Conference on Electrical Machines and Systems (ICEMS), 2010*. Incheon: IEEE, 2010, pp. 13–24.

[2] T. Hüfner, O. Radler, T. Ströhla, T. Sattel, J. Wesselingh, A. Vogler, and D. Eicher, "A note on electromagnetic gravity compensation actuators based on soft electro- permanent magnets for adjustable reluctance force," in *17th International EUSPEN Conference Proceedings*. Hannover: EUSPEN, 2017. [Online]. Available: www.euspen.eu

[3] N. H. Vrijsen, J. W. Jansen, and E. A. Lomonova, "Comparison of linear voice coil and reluctance actuators for high-precision applications," in *Proceedings of EPE-PEMC 2010 - 14th International Power Electronics and Motion Control Conference*, 2010, pp. 6–8.

[4] R. Munnig Schmidt, G. Schitter, A. Rankers, and J. Van Eijk, *The Design of High Performance Mechatronics*, 2nd ed. Ios Press, 2014.

[5] J. Wesselingh, "Anordnung zur Halterung eines Bauteils in einer Lithographieanlage sowie Lithographieanlage," 7 2015. [Online]. Available: https://google.com/patents/DE102015201096A1

[6] S. Kuiper, N. Doelman, E. Nieuwkoop, T. Overtoom, T. Russchenberg, M. van Riel, J. Wildschut, M. Baeten, J. Human, H. Spruit, S. Brinkers, and M. Maniscalco, "Electromagnetic deformable mirror development at TNO," in *Proc.SPIE*, 2016, pp. 9912 – 9912 – 7.

[7] A. N. Knaian, "Electropermanent magnetic connectors and actuators : devices and their application in programmable matter," Ph.D. dissertation, Massachusetts Institute of Technology, 2010.

[8] A. D. Marchese, "Controlling the Locomotion of a Separated Inner Robot from an Outer Robot using Electropermanent Magnets," Ph.D. dissertation, Massachesetts Institute of Technology, 2012.

[9] V. Ostovic, "Memory motors-a new class of controllable flux PM machines for a true wide speed operation," in *Conference Record of the 2001 IEEE Industry Applications Conference. 36th IAS Annual Meeting*, vol. 4. IEEE, 2001, pp. 2577–2584.

[10] C. Yu, K. T. Chau, X. Liu, and J. Z. Jiang, "A flux-mnemonic permanent magnet brushless motor for electric vehicles," *Journal of Applied Physics*, vol. 103, no. 7, p. 07F103, 4 2008.

[11] Chunhua Liu, K. T. Chau, and Chun Qiu, "Design and Analysis of a New Magnetic-Geared Memory Machine," *IEEE Transactions on Applied Superconductivity*, vol. 24, no. 3, pp. 1–5, 6 2014.

[12] Q. Wang and S. Niu, "Electromagnetic design and analysis of a novel fault-tolerant flux-modulated memory machine," *Energies*, vol. 8, no. 8, pp. 8069–8085, 2015.

[13] A. D. Marchese, H. Asada, and D. Rus, "Controlling the locomotion of a separated inner robot from an outer robot using electropermanent magnets," in *2012 IEEE International Conference on Robotics and Automation*. IEEE, 5 2012, pp. 3763–3770.

[14] P. Ward and D. Liu, "Design of a high capacity Electro Permanent Magnetic adhesion for climbing robots," in *IEEE International Conference on Robotics and Biomimetics (ROBIO)*. IEEE, 2012, pp. 217–222.

[15] F. Ochoa-Cardenas and T. J. Dodd, "Design of an active magnetic wheel with a varying Electro-Permanent Magnet adhesion mechanism," in *IEEE International Conference on Intelligent Robots and Systems*. IEEE, 2015, pp. 3340–3345.

[16] P. Campbell, *Permanent Magnet Materials and their Design*. Cambridge University Press, 1994.

[17] P. Campbell and S. Al-Murshid, "A model of anisotropic Alnico magnets for field computation," *IEEE Transactions on Magnetics*, vol. 18, no. 3, pp. 898–904, 1982.

[18] S. Hui, J. Zhu, and V. Ramsden, "A generalized dynamic circuit model of magnetic cores for low- and high-frequency applications. II. Circuit model formulation and implementation," *IEEE Transactions on Power Electronics*, vol. 11, no. 2, pp. 251–259, 3 1996.

[19] I. R. Mackenzie, "Design and control methods for high-accuracy variable reluctance actuators," Ph.D. dissertation, Massachusetts Institute of Technology, 2015.

[20] J. R. Brauer, *Magnetic Actuators and Sensors*. Wiley-IEEE Press, 2006.

[21] J. Brauer and I. Mayergoyz, "Finite-Element Computation of Nonlinear Magnetic Diffusion and Its Effects When Coupled to Electrical, Mechanical, and Hydraulic Systems," *IEEE Transactions on Magnetics*, vol. 40, no. 2, pp. 537–540, 3 2004.

[22] B. D. Cullity and C. D. Graham, *Introduction to Magnetic Materials*. Wiley, 2011.

[23] S. Skogestad and I. Postlethwaite, *Multivariable feedback control: analysis and design*, 2nd ed. Wiley New York, 2010.

[24] Thorlabs Inc., "Thorlabs Linear Translation Stage," 2018. [Online]. Available: https://www.thorlabs.com/thorproduct.cfm?partnumber=XR25C/M

[25] Asensor Technology AB, "Linear High Precision Analog Hall Sensors."

[26] dSPACE GmbH, "dSPACE RTI," 2018. [Online]. Available: https://www.dspace.com

[27] "Technical Data Sheet - AlNiCo Magnets," Eclips Magnetics, Tech. Rep. [Online]. Available: www.eclipsemagnetics.com

[28] The MathWorks Inc., "Simulink," 2018. [Online]. Available: https://nl.mathworks.com/

3

Tunable Magnet Actuators: Break-Even Tuning Interval

This chapter has been written in the form of a scientific paper. It investigates the use of TMs in actuators and in what type of actuation applications they can improve energy efficiency. This is done by making an energy dissipation comparison between a TM actuator and a normal actuator of identical geometry. Derived from the analysis is a metric called the break-even tuning interval, that can be used to evaluate potential TM actuator applications.

Some expressions used in this paper are derived in other parts of this thesis: The derivation of the expressions for saturation current I_{max} and the coil inductance L can be found in chapter 2. The derivation of the coil resistance R can be found in appendix D.

Tunable Magnet Actuators: Break-Even Tuning Interval

I. Introduction

Tunable Magnet (TM) actuators have the potential to increase the energy efficiency in certain actuation systems. Better energy efficiency decreases actuator self-heating and improves thermal stability. The reason that the TM actuator is more efficient for some applications comes from the fact that it requires only a short current pulse to set the magnetization of an AlNiCo permanent magnet (PM), after which a static force is maintained without further energy input. A regular reluctance actuator on the other hand, when not preloaded, requires a continuous current input even to maintain a constant force.

However, there is a limit to the efficiency gain of using TM actuators, depending on their applications. If the application requires constant magnetization state tuning of the AlNiCo PM, the TM actuator always dissipates more energy then a similar actuator without a TM. Independent of the way the magnetization state tuning is achieved, there is always extra hysteresis loss. On the other hand, if the TM actuator needs to supply a constant force over an extended period and only needs incidental magnetization state tuning, the efficiency gain compared to a conventional actuator can be significant. The longer the interval between required tuning cycles, the more efficient the TM actuator becomes compared to a conventional reluctance actuator.

To evaluate this, we introduce a metric called the *Break-even Tuning Interval* or T_{be}. It is defined as the interval between magnetization tuning cycles, such that a TM actuator dissipates the same amount of energy as a comparable normal actuator while generating the same air-gap flux density at an identical air-gap. This metric can then be used to evaluate potential TM actuation applications. If the TM requires magnetization state tuning in that particular application less often then T_{be}, it is likely to improve the energy efficiency.

In this paper we will derive T_{be} in terms of actuator properties and perform a sensitivity study to evaluate the dependencies on air-gap width l_g, air-gap flux density B_g and magnetizing voltage U. We'll also derive a scaling law to evaluate how T_{be} is effected by actuator dimension. Next, the energy dissipation for the different actuators is evaluated for some example force profiles, to compare the efficiency gain in real applications. The influence of the dynamic system in which the TM actuator is applied is also discussed, as the interaction between the

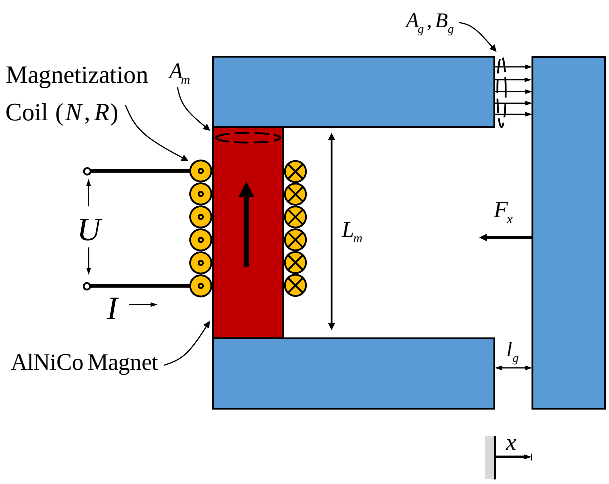

(a) Schematic of TM reluctance actuator

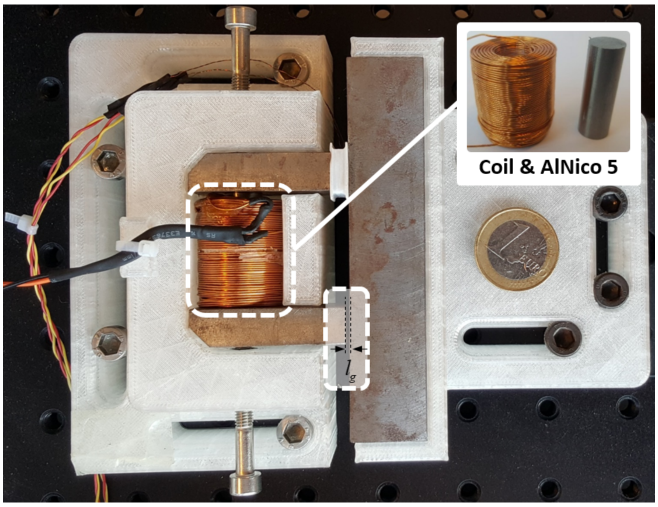

(b) Experimental realization of TM reluctance actuator

Fig. 1: Schematic overview of a gap closing reluctance actuator with a TM, together with the experimental realization. See [1] for further details. Table I shows the associated parameter values.

TABLE I: Parameters for TM actuator implementation shown in Fig. 1a

AlNiCo 5 TM actuator parameters			
Symbol	Value	Comment	Source
AlNiCo 5 magnet		Other names: LNG44, Alcomax 3	
L_m	30.20 mm	Magnet length	
d_m	9.83 mm	Magnet diameter	
A_m	75.89 mm^2	Magnet surface	
B_r	1.25 T	Remanent flux density	[3]
H_c	50 $\mathrm{kA\,m^{-1}}$	Coercive force	[3]
H_{sat}	150 $\mathrm{kA\,m^{-1}}$	Saturation field intensity ($3 \times H_c$)	[4]
$\mu_{r,max}$	270	Maximum relative permeability	[5]
Coil			
N	668	Number of coil windings	
R	3.5 Ω	Coil resistance	
Magnetic Circuit			
A_g	200 mm^2	Air-gap surface	

two poses some challenges. To conclude, we give some recommendations for suitable TM actuator applications.

The derivation of the Break-even Tuning Interval is similar to the derivation of the break-even switching time analysis done by [2] for the electropermanent magnet.

II. Basis for Comparison

To be able to compare the TM actuator with a similar standard actuator, some assumptions are made. These are elaborated in this section. In general, for all calculations, we will assume ideal magnetic circuit models with soft iron circuit components that have infinite permeability. Also, fringing and leakage flux effects are neglected.

A. Actuator Force

For comparison, the standard gap closing reluctance actuator topology is used. Figure 1a shows a schematic of such a reluctance actuator containing a TM, consisting of an AlNiCo magnet with a magnetizing coil around it. The experimental realization of the actuator [1] is shown in Fig. 1b. The regular reluctance actuator is the same except it contains a conventional electromagnet (EM), consisting of a coil with a soft iron core. Both actuators are assumed to have the same dimensions, as shown in Tab. I.

The relation between air-gap flux density and force in this type of actuator can be written as [2]:

$$F_x = \frac{B_{gap}^2 A_g}{\mu_0} \tag{1}$$

To be able to compare the 2 actuators, we assume that both actuators sample the same reference force profile with the sampling period T_s, as shown in Fig. 2. For the EM actuator, this means that the actuator current is regulated according to (1). The TM actuator has to go through a tuning cycle each period T_s. A qualitative sketch of the resulting force profile is shown in Fig. 2 by the red, dotted line. Note the force peaks due to magnet saturation. In this analysis, we assume that the tuning time, T_{tune} is much smaller than T_s, such that the force of both actuators is equal most of the time between samples.

Although the TM actuator can be used to control a dynamic system, for this comparison we make the assumption that the air-gap is fixed.

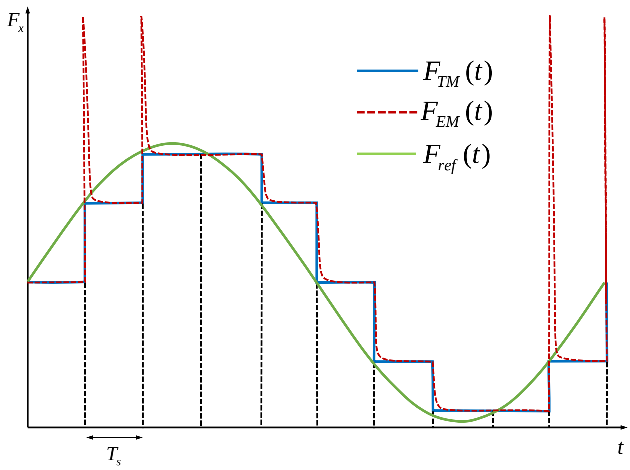

Fig. 2: Qualitative force profile as sampled by the TM and EM actuators at fixed air-gap. Note the force disturbance peaks caused by the magnet saturation when transitioning to a higher magnetization.

B. Hysteresis behaviour

One of the differences in energy dissipation between the 2 actuators is the additional hysteresis loss in the TM actuator. To estimate this, we assume the BH curve to be parallelogram shaped, as shown in Fig. 3. This loop is uniquely defined by the AlNiCo material parameters B_r, H_c and the minimum and maximum permeability values μ_0 and μ_{max}, so the analysis can easily be used for all grades of AlNiCo.

The permeability of AlNiCo $\frac{dB_m}{dH_m} = \mu$ varies during the tuning process. For this analysis however it is assumed constant, with a value of:

$$\mu_{r,avg} = \frac{1}{2}\mu_{r,max} \tag{2}$$

where μ_r is the permeability expressed as a relative value.

C. Magnetization State Tuning

For the magnet tuning process, we assume a simplified version of the one proposed in [1]. It can be summarized as follows: If

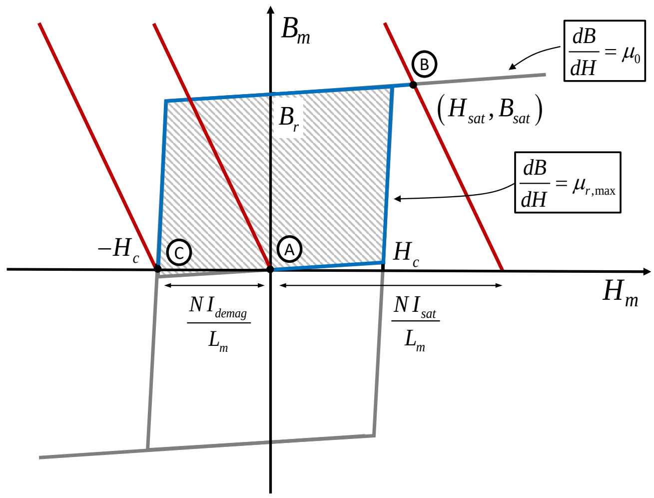

Fig. 3: Schematic overview of the simplified parallelogram shaped BH characteristic of the AlNiCo PM. Drawn in blue is a worst case magnetization state tuning trajectory, with load-lines (red) showing the starting magnetization [A], the saturation point [B] and the demagnetization [C].

the desired magnetization level is above the present level, the magnet is first saturated and then demagnetized to the desired level. This is achieved by a saturation voltage pulse and an opposite demagnetization pulse, both of constant voltage. If the desired magnetization level is below the present level, only the demagnetization pulse is necessary.

The effect of a magnetizing current on the magnetization of the AlNiCo PM is best visualized using the BH curve and a load-line [1]. The magnet operating point is defined as the point where the load-line intersects the BH curve. A magnetizing current affects the magnet operating point by shifting the base of the load-line over the horizontal axis.

The magnetization state trajectory for a worst case tuning cycle is shown in Fig. 3 in blue. Shown in red are the load-lines that determine the operating points at different steps in the tuning cycle. Starting at zero magnetization $(0, 0)$ [A], the magnet is first saturated to (H_{sat}, B_{sat}) [B] and then demagnetized to $(-H_c, 0)$ [C]. This tuning cycle gives the highest energy dissipation possible and is used in the rest of this analysis.

A qualitative sketch of a voltage and corresponding current profile belonging to a tuning cycle with 2 pulses is shown in Fig. 4.

D. Summary of Assumptions

The assumptions underlying this analysis can be summarized as:

1) Ideal magnetic circuit models.
2) Fixed air-gap width l_g.
3) EM actuator samples discrete flux density signal with period T_s.

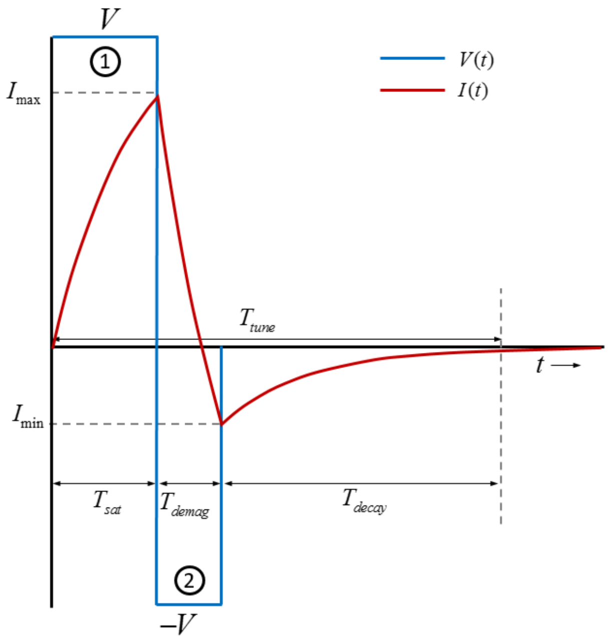

Fig. 4: Saturation [A] and demagnetization voltage pulses [B] shown in blue with the corresponding current shown in red.

4) $T_{tune} \ll T_s$.
5) Parallelogram shaped BH-curve, defined by B_r, H_c, μ_{max} and μ_0.
6) permeability during tuning is constant and equal to μ_{avg}
7) Magnetization state tuning using 2 constant voltage pulses of U_c.

E. Energy analysis

The break-even tuning interval is derived by comparing energy dissipation of both actuators during a sample T_s:

$$E_{TM} = E_{hyst} + E_{TM,copper} \tag{3}$$
$$E_{EM} = E_{EM,copper} \tag{4}$$

Where E_{TM} is the energy dissipation in the TM actuator and E_{EM} is the energy dissipated in the EM reluctance actuator. The TM actuator has resistive losses, denoted by $E_{TM,copper}$, during the magnetization state tuning and an additional hysteresis loss E_{hyst}. The EM actuator has only the resistive losses $E_{EM,copper}$, however, they are continuous over the whole period T_s.

F. TM actuator

In general, energy dissipation in a resistor, due to a current $I(t)$ over a period T is defined as:

$$E_{copper} = \int_0^T I^2(t)\, R \;\, \mathrm{d}t \tag{5}$$

To determine the current needed for magnetization state tuning, the parallelogram-shaped hysteresis loop in Fig.3 is used. The current needed to saturate the AlNiCo magnet, in terms of system parameters can be written as [1]:

$$I_{max} = \frac{L_m}{N}\left[H_{sat} + 2\left(\frac{B_r}{\mu_0} + H_{sat}\right)\frac{A_m}{A_g}\frac{l_g}{L_m}\right] \tag{6}$$

The magnitude of the demagnetization current depends on the desired level of magnetization. In a worst case, the material is demagnetized to a level close to zero, corresponding to a shift of the base of the load-line to point H_c (see Fig.3). This requires a demagnetization current of:

$$I_{min} = -\frac{L_m}{N}H_c \tag{7}$$

The magnetizing coil is voltage driven with saturation and demagnetization pulses as shown in Fig. 4. The current profile $I(t)$ as a result of applied voltages U and $-U$ is a piece-wise continuous set of exponential curves described by:

$$I_{sat}(t) = \frac{U}{R}\left(1 - \mathrm{e}^{-\frac{tR}{L}}\right) \tag{8}$$

$$I_{demag}(t) = I_{max}\,\mathrm{e}^{-\frac{tR}{L}} - \frac{U}{R}\left(1 - \mathrm{e}^{-\frac{tR}{L}}\right) \tag{9}$$

$$I_{decay}(t) = I_{min}\,\mathrm{e}^{-\frac{tR}{L}} \tag{10}$$

where L and R are the coil self-inductance and resistance. Writing these equations explicit for t gives the saturation, demagnetization and decay times as a function of I_{max} and I_{min} as:

$$T_{sat} = \frac{L}{R}\ln\left(\frac{U}{U - I_{max}R}\right) \tag{11}$$

$$T_{demag} = \frac{L}{R}\ln\left(\frac{U + I_{max}R}{U - I_{min}R}\right) \tag{12}$$

$$T_{decay} = \frac{L}{R}\ln\left(\frac{I_{min}}{I_{zero}}\right) \tag{13}$$

$$T_{tune} = T_{sat} + T_{demag} + T_{decay} \tag{14}$$

where I_{zero} is just a current value close to zero to mark the end of the exponential current decay.

The self inductance L, based on the average permeability $\mu_{r,avg}$ can be written in terms of TM parameters as [1]:

$$L = N^2\left[\left(\frac{A_g\mu_0}{2l_g}\right)^{-1} + \left(\frac{A_m\mu_0\mu_{r,avg}}{L_m}\right)^{-1}\right]^{-1} \tag{15}$$

The resistance R of the coil can be estimated as [1]:

$$R = 16\frac{\rho N^2}{L_m} \tag{16}$$

The I^2R losses from the tuning cycle are then be evaluated by performing the integral of (5) as:

$$\begin{aligned} E_{copper,TM} = &\int_0^{T_{sat}} I_{sat}^2(t)\, R \;\, \mathrm{d}t + \\ &\int_0^{T_{demag}} I_{demag}^2(t)\, R \;\, \mathrm{d}t + \\ &\int_0^{T_{decay}} I_{decay}^2(t)\, R \;\, \mathrm{d}t \end{aligned} \tag{17}$$

where the tuning cycle times are defined by by (11), (12) and (13) and magnetizing currents by (8), (9) and (10).

Next, we evaluate the hysteresis loss during a tuning cycle using the parallelogram shaped BH curve in Fig. 3. The hysteresis energy dissipation is proportional to the surface of the hysteresis characteristic that is traversed and the volume of the magnetic material:

$$E_{hyst} = A_m L_m \int H dB \tag{18}$$

$$\tag{19}$$

In a worst-case scenario, the total area of loop traversed during tuning is equal to half of the complete loop, marked by the grey area in Fig. 3. The maximum hysteresis loss per tuning cycle is then evaluated by:

$$E_{hyst} = 2 \cdot B_r H_c A_m L_m \tag{20}$$

G. EM actuator

To evaluate the relation between coil current I and gap flux density B_g for the EM reluctance actuator, the AlNiCo PM in Fig. 1 is replaced by a soft iron core, such that *Ampere's Circuit Law* evaluates to [4]:

$$2H_g l_g = NI \tag{21}$$

With $B_g = \mu_0 H_g$ in the air-gap this gives the following expression for calculating the required coil current:

$$I_{EM} = \frac{2B_g l_g}{\mu_0 N}. \quad (22)$$

The energy dissipation associated with the EM reluctance actuator, which is only resistive in nature, can now be calculated for a period T_s as:

$$E_{EM} = P_{EM} \cdot T_s \quad (23)$$

$$P_{EM} = I_{EM}^2 R \quad (24)$$

H. Break-even Tuning Interval

To determine the break-even tuning interval, we equate the energy losses of both actuators and evaluate for which period they are equal:

$$T_{be} = \frac{E_{hyst} + E_{TM,copper}}{P_{EM}} \quad (25)$$

To calculate T_{be}, (22) needs values for B_g and l_g, i.e. the state of the EM actuator at which it is compared with the TM actuator. These values vary, depending on the actuator force and position. Also, the voltage U with which the magnetization state tuning is done needs to be defined. Table II shows T_{be}, evaluated for 3 scenarios. The rest of the general actuator parameters are taken from from Tab. I. Table III shows values for the different dissipation terms from (3) and (4) for the nominal scenario. These scenario's are based on reasonable values for the TM actuator parameters. In the 'Best' scenario, for example, the actuators are compared using the maximum air-gap flux density value $B_{g,max} \approx 0.2$ which AlNiCo 5 can supply in the TM actuator of Fig. 1.

Notwithstanding the names of the shown scenario's, the entire break-even tuning time analysis is based on a worst case in terms of energy dissipation. For example, it is assumed that the magnet is fully saturated and demagnetized every tuning cycle, so every cycle takes into account the highest possible magnetizing current dissipation and the full hysteresis loss.

	U[V]	B_g[T]	l_g[mm]	T_{be}[s]
Worst	30	$\frac{1}{2}B_{g,max}$	1	7.10
Nominal	300	$\frac{1}{2}B_{g,max}$	1.5	1.19
Best	500	$B_{g,max}$	1.5	0.26

TABLE II: The break-even tuning interval evaluated for different scenarios

Looking at the data in Tab. III, it is clear that the biggest contribution to the tuning cycle time comes from the decay time T_{decay}. This time is not influenced by the tuning voltage as shown in (13). However the energy dissipated during the decay is independent of T_{dec}, namely $E_{decay} = \frac{1}{2}LI_{min}^2$. This dissipation is associated with the energy that comes from the collapsing magnetic field in the coil. The slow decay, therefore, does not influence the associated dissipation.

T_{be} Analysis Results		
TM actuator		
Saturation	$T_{sat} = 0.96\,\mathrm{ms}$	$E_{TM,sat} = 0.088\,\mathrm{J}$
Demagnetization	$T_{demag} = 1.1\,\mathrm{ms}$	$E_{TM,demag} = 0.077\,\mathrm{J}$
Decay	$T_{decay} = 29\,\mathrm{ms}$	$E_{TM,decay} = 0.079\,\mathrm{J}$
Hysteresis	n/a	$E_{hyst} = 0.29\,\mathrm{J}$
EM actuator		
Dissipated power	$P_{EM} = 0.45\,\mathrm{J\,s^{-1}}$	

TABLE III: break-even tuning time analysis results for the nominal scenario (see Tab. II

The other fixed dissipation term is the AlNiCo hysteresis loss. This is significantly higher than the magnetizing current dissipation for the nominal scenario. If the coil driving voltage where to be decreased, such as in the worst scenario in Tab. II, the contribution of the magnetizing current becomes dominant in T_{be}.

III. Parameter Sensitivity & Scaling

A parameter study is performed to better investigate the influence of the magnetizing voltage U and the state of the actuator (B_g,l_g). Figure 5 plots the tuning interval against a variation in these parameters. The green regions represent tuning intervals and parameter values for which a TM actuator is more efficient than a comparable regular actuator. The border between the regions therefore represents the variation of the break-even tuning interval. In this analysis, each parameter is individually varied while the others have their specified nominal values.

The sensitivity on the coil voltage U can be explained by considering tuning time. Higher voltages result in faster tuning as shown by (14), which decreases the resistive energy dissipation during a tuning cycle. This significantly lowers T_{be}.

The sensitivity on the air-gap width l_g and the air-gap flux B_g can be understood by considering (22). As the air-gap flux at which the two actuators are compared decreases, the break-even tuning interval increases rapidly. This is because the current required in the EM actuator is proportional to the resulting air-gap flux (22), whereas the TM as considered in this analysis always requires the same current to saturate and demagnetize. The same goes for the air gap width l_g, which is also proportional to the required current in the EM actuator.

From the viewpoint of applicability, it is also interesting to see how the break-even tuning interval scales with TM geometry. To do this, the length scaling of TM properties is analyzed and combined to get the length scaling of T_{be}. We assume that the saturating and demagnetizing voltage remains constant and that the air-gap width l_g also scales proportionally with the TM geometry.

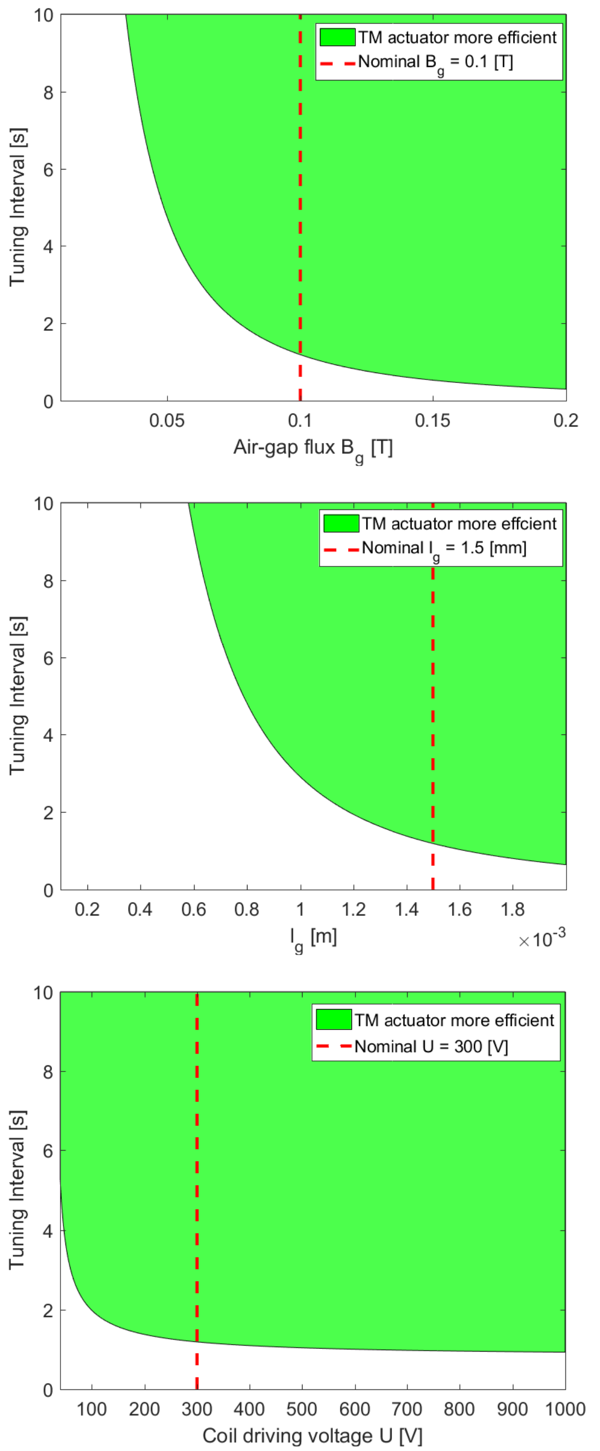

Fig. 5: Sensitivity of T_{be} on the state of the actuator (B_g, l_g) and the magnetizing voltage U.

.

Collecting geometrical dependencies in above-described equations for various TM properties yields the scaling properties in Tab. IV. Combining these terms yields the length scaling law for T_{be}. It turns out that scaling is with the square of the TM length, meaning that a TM actuator is relatively more efficient at smaller length scales.

Parameter	Comment	Length Scaling	Eq.
L	Coil Inductance	l^1	(15)
R	Coil Resistance	l^{-1}	(16)
$I_{max,min}$	(De)magnetizing pulses	l^l	(6)(7)
T_{tune}	Tuning cycle time	l^2	(11)(12)(13)
E_{hys}	Hysteresis tuning loss	l^3	(20)
$E_{TM,copper}$	Resistive tuning loss	l^3	(17)
I_{EM}	EM actuator current	l^1	(22)
P_{EM}	EM actuator power loss	l^l	(24)
F_x	Actuator Force	l^2	(1)
T_{be}	Break-even Tuning Interval	l^2	(25)

TABLE IV: Length scaling of TM properties assuming constant supply voltage U

IV. Force profile Comparison

The break-even tuning interval analysis only compares the two actuators at one level of air-gap flux density and therefore actuator force. In this section, we'll compare some realistic force profiles and see what the energy efficiency gain is if a TM actuator would generate the profile.

The force profiles used for comparison are simple sinusoids, described by:

$$F_x(t) = F_0 \sin(2\pi f t) \tag{26}$$

where f is the frequency and F_0 the constant bias force.

The improvement in energy efficiency is calculated using:

$$\eta = 1 - \frac{\Sigma_1^n E_{TM,n}}{\int_0^T I_{EM}^2(t)\, R\ \mathrm{d}t} \tag{27}$$

where $E_{TM,n}$ is the energy dissipation during a single tuning cycle. Summing over n samples of length T_s that make up the force profile yields the total energy dissipation for the TM actuator. When evaluating E_{TM}, the magnetization state tuning method as described in Sec. II-C is used. The denominator in (27) gives the energy dissipated in the conventional reluctance actuator for the same 'unsampled' force profile, where the current I_{EM} corresponding to the force F_x is evaluated using (1).

Table V gives the the values for the efficiency gain calculated by (27) for the different force profiles. The magnetizing voltage U and actuator state B_g, l_g used to compare the force profiles are of the nominal scenario described by Tab. II. Only now the air-gap flux B_g, varies to produce the force profile. Using a tuning interval $T_s = 1\,\mathrm{s}$, which is about equal to

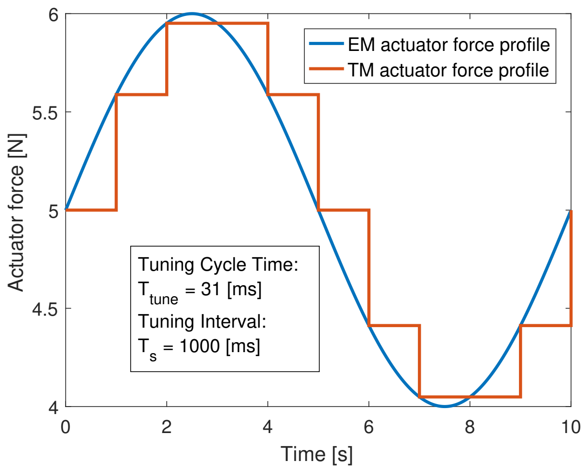

Fig. 6: Sinusoidal force profile with high constant bias force as produced by the EM and TM actuators.

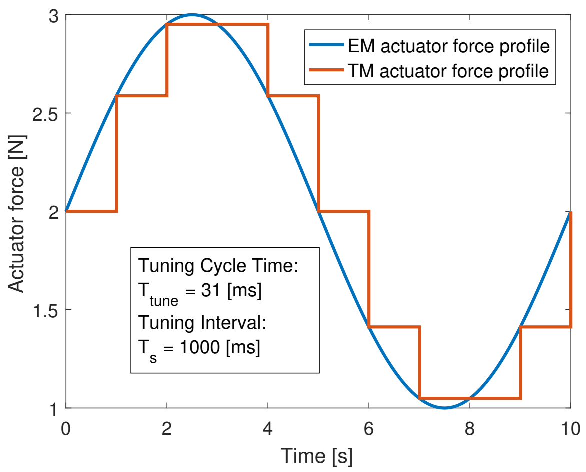

Fig. 7: Sinusoidal force profile with with low constant bias force as produced by the EM and TM actuators.

T_{be} for the nominal scenario, already yields an efficiency gain because not every tuning cycle includes a saturation step. The force profile from Fig. 6 has a higher efficiency gain, because of the higher level of constant bias flux. This is consistent with the sensitivity analysis (Fig. 5).

V. TM Actuator Bandwidth

Compared to the EM actuator, the TM actuator 'samples' the force profile with period T_s (the tuning interval). If we make

Profile	F_0	f	U	l_g	η
Fig. 6	5 N	0.1 Hz	300 V	1.5 mm	66 %
Fig. 7	2 N	0.1 Hz	300 V	1.5 mm	14 %

TABLE V: Caption

the analogy with sampling an electrical signal, the sampling rate should be 10 times the closed loop system bandwidth of the TM actuation system for good control performance. This is according to a rule-of-thumb by [6]. If the T_{be} is used as the sampling period, we get the following rule for the achievable closed-loop bandwidth of a TM actuation system:

$$\omega_{cl} \leq \frac{2\pi}{10\,T_{be}} \tag{28}$$

If the desired system closed-loop bandwidth is higher, it is most likely not more energy efficient to use a TM actuator. Noting that $T_{be} \approx 1\,\mathrm{s}$ for the nominal scenario of Tab. III, the closed loop system bandwidth achievable is $f_{cl} = \frac{\omega_{cl}}{2\pi} \approx 0.1\,\mathrm{Hz}$. This severely limits the applicability of the TM actuator. Especially if you take the high sensitivity of T_{be} on several application specific actuator characteristics into account. However, equation (28) is only valid if every change in actuator force is achieved by tuning the AlNiCo PM (irreversible changing of the magnetization).

A possible way to increase the energy efficient bandwidth of a TM actuation system is to combine the TM actuator in parallel with a conventional actuator such that the control tasks can be divided. The TM actuator would generate the low frequency, large amplitude part of the necessary force, and the conventional actuator would handle the required high-frequency variations. By using this parallel configuration, the combination can still be more energy efficient, while actuation higher bandwidth systems.

VI. Dynamic system interaction

In this analysis so far we have assumed that the air-gap width l_g is constant. In real actuators, however, the air-gap varies with the position of the mover. This means that there is an interaction between the TM actuator and the dynamic system it is actuating. Therefore, the situation as depicted in Fig. 6 is not accurate. The continuously varying air-gap effects the magnetization of the AlNiCo, so the actuator force is not constant between tuning cycles.

A more problematic effect of the dynamic system interaction are tuning disturbances. In other words, disturbances caused by the magnetization state tuning process. Looking at the qualitative force profile in Fig. 2, we see the force pulses caused by AlNiCo saturation. Depending on the dynamic properties of the actuated mechanical system, these force pulses create an actuator position disturbances. To minimize this effect, the mechanical time constant of the actuated system should be small compared to the tuning time, such that it acts as a mechanical low-pass filter. Therefore the application of TM actuators should be limited to systems with sufficiently slow dynamics.

VII. CONCLUSION

In this paper, we have derived a metric called the Break-Even Tuning Interval, which is defined as the interval between magnetization tuning cycles, such that a TM actuator dissipates the same amount of energy as an equivalent regular actuator at a constant force output. This can be used to evaluate potential TM actuation applications. It is however very sensitive to the magnetizing coil voltage used and the state in which the actuators are compared, defined by (B_g, l_g). For a nominal scenario (Tab. II) and the actuator from Fig. 1, $T_{be} \approx 1\,\mathrm{s}$. The break-even tuning interval analysis is however in itself a worst case scenario in terms of energy, since every tuning cycle is assumed to dissipate the energy associated with saturation and full demagnetization. A more realistic simulation of a sinusoidal force profile shows that with a tuning interval $T_s \approx T_{be}$, there is already an energy efficiency gain in using a TM actuator. This is shown in Figs. 6 and 7 and Tab. V. Geometrical scaling analysis shows that $T_{be} \propto l^2$, i.e. T_{be} scales with the square of the TM size. This means that a TM actuator is more efficient at smaller length scales.

The break-even tuning interval has consequences for the maximum achievable bandwidth of TM actuation systems, for which there is still an efficiency gain. As shown in Fig. 2, the TM actuator can 'sample' a force profile using magnetization state tuning. If the maximum sampling period is given by T_{be} then the achievable closed-loop actuation bandwidth can be predicted using (28). As $T_{be} \approx 1\,\mathrm{s}$ the closed loop actuation bandwidth is $f_{bw} \approx 0.1\,\mathrm{Hz}$. This is therefore only useful for systems requiring a very low actuation bandwidth. However, a parallel combination of a TM actuator and a regular can potentially increase the energy efficient actuation bandwidth.

Implementing a real TM has some more complications, coming from the interaction between the TM actuator and the system it is actuating. The most important effect is the tuning disturbance, caused by the saturation current pulse.

The potential energy gain of using a TM is very much application and situation dependent. The break-even tuning interval is very sensitive to the circumstances in which actuators are compared, and the interaction between the TM actuator and the dynamic system it actuates is not yet sufficiently understood. However, based on this paper we can give some general recommendations for suitable TM actuation applications:

- **Low bandwidth actuation** The TM actuator is most suited for tasks requiring a low actuation bandwidth, or a higher bandwidth when reversible and irreversible magnet operation is combined.
- **Incidental actuation** A substantial gain in efficiency can be achieved for systems that are static most of the time and only requiring incidental actuation.
- **Large air-gap applications** The sensitivity analysis (Fig. 5) shows that TM actuators are relatively more efficient for large air-gap widths.
- **Large constant bias force** Applications requiring a large constant bias force benefit more from a TM actuator. This force is delivered without energy expense by the AlNiCo PM.
- **Small scale actuation** T_{be} scales with the square of the TM size. Therefore the TM becomes more efficient or more versatile in its applicability at smaller length scales.
- **High voltage power supply** Using a high voltage power supply results in faster, more energy efficient tuning. Faster tuning also decreases the effect of the disturbances on the mechanical system caused by the tuning process. The maximum tuning achievable speed is, however, is limited by the magnetization time constant of the AlNiCo magnet. [7].

REFERENCES

[1] S. G. Vietor, Spronck Jo W., and S. H. HosseinNia, "Tunable Magnets: modeling and validation for dynamic and precision applications," Master's thesis, Delft University of Technology, 2018.

[2] A. N. Knaian, "Electropermanent magnetic connectors and actuators : devices and their application in programmable matter," Ph.D. dissertation, Massachusetts Institute of Technology, 2010.

[3] "Technical Data Sheet - AlNiCo Magnets," Eclips Magnetics, Tech. Rep. [Online]. Available: www.eclipsemagnetics.com

[4] P. Campbell, *Permanent Magnet Materials and their Design*. Cambridge University Press, 1994.

[5] P. Campbell and S. Al-Murshid, "A model of anisotropic Alnico magnets for field computation," *IEEE Transactions on Magnetics*, vol. 18, no. 3, pp. 898–904, 1982.

[6] R. Munnig Schmidt, G. Schitter, A. Rankers, and J. Van Eijk, *The Design of High Performance Mechatronics*, 2nd ed. Ios Press, 2014.

[7] J. R. Brauer, *Magnetic Actuators and Sensors*. Wiley-IEEE Press, 2006.

4

Conclusions & Recommendations

4.1. Conclusions

The research goal of this thesis was stated as follows:

> *Develop a Tunable Magnet that can be robustly tuned in the presence of a dynamically varying air-gap, and investigate its use in precision actuation systems*

Regarding the objectives, the following conclusions can be drawn.

Model the Tunable Magnet to gain insight into its behavior and test possible magnetization state tuning methods

An analytic model of the TM reluctance actuator has been derived, using a graphical hysteresis representation. Using this model the effect of a coil voltage on the magnetization state of the AlNiCo can be predicted. To enable computer simulation, the graphical hysteresis representation is replaced by a *Preisach* ferromagnetic hysteresis model. This hysteresis model can fully describe permanent magnet behavior, including minor loops and recoil-lines. For control design, a linearized model of the TM has been derived that describes the behavior around a chosen operating point.

Develop a method for robust magnetization state tuning under a dynamically varying air-gap

A magnetization state tuning method has been developed, consisting of the following steps:

1. **Predict** Using an analytical model of the TM actuator, a suitable magnet operating point is determined that will result in the required air-gap flux, at the given air-gap length. Next, the recoil-line needed to arrive at this operating point is calculated.
2. **Saturate** If the present recoil-line is lower then the predicted one, the AlNiCo is first saturated by a large enough current pulse through the magnetization coil.
3. **Demagnetize** A flux-feedback controller is used to demagnetize the AlNiCo until such a point that it will subsequently operate on the predicted recoil-line. The right controller set-point is determined using measured hysteresis data.

The flux feedback controller is meant to ensure that, even when the air-gap varies during the tuning cycle, the right magnetization state is still reached. However, this air-gap disturbance rejection capability is not yet tested, since the measurement setup is static only.

Investigate the implementation of Tunable Magnets in actuators and define in what type of applications they can improve energy efficiency

An important objective of this work was to investigate the implementations of TMs in actuation applications. Tunable magnets can provide significant efficiency improvements in quasi-static actuation applications, i.e., applications with slow movement or more extended periods of constant actuator force. If the actuator force has to be constantly modulated, however, it is almost certainly less efficient then a conventional or hybrid reluctance actuator.

To evaluate the efficiency of a TM actuator compared to a conventional actuator, we have introduced a metric called *Break-Even Tuning Interval* or T_{be}. This is defined as the period in which two comparable reluctance actuators, one with a TM and one without, dissipate the same amount of energy while outputting a constant force at equal air-gap width. For the reluctance actuator topology used throughout this thesis, the break-even tuning interval is in the order of $T_{be} \approx 1\,\text{s}$. Sampling a force profile with constant force levels of this duration gives an idea of what closed loop actuation bandwidths can be achieved with the TM actuator. If we use the rule of thumb that the closed-loop system bandwidth has to be at least ten times lower then the sampling time, the maximum actuation bandwidth for which a TM actuator is still more energy efficient is in the range of $f_{bw} = 0.1\,\text{Hz}$.

However, this value is dependant on many factors. First of all, it is a worst-case scenario, derived with the specific magnetization state tuning method proposed in this thesis. It assumes that every tuning cycle always consists of a saturating pulse and a complete demagnetization. This is a significant overestimate of the dissipated energy. Secondly, a sensitivity study shows that T_{be} is very sensitive to certain parameters used in the comparison. In particular the state (B_g, l_g) at which the two actuators are compared and the magnetizing voltage U_s. A scaling analysis shows that the break-even tuning interval is also very sensitive to actuator dimensions, as it scales with the square of the actuator length, i.e., $T_{be} \propto l^2$.

Based on the break-even tuning interval analysis, the following recommendations can be made for suitable TM applications:

- **Low bandwidth & incidental actuation**
  The TM actuator is most suited for applications requiring a low actuation bandwidth. The same goes for systems that are static most of the time and only requiring incidental actuation.
- **Large air-gap applications** A sensitivity analysis shows that TM actuators are relatively more efficient for large air-gap widths compared to regular reluctance actuators.
- **Large constant bias force**
  Applications requiring a large constant bias force benefit more from a TM actuator. This force is delivered without energy expense by the AlNiCo PM.
- **Small scale actuation**
  T_{be} scales with the square of the TM length. Therefore the TM becomes more efficient and more versatile in its applicability at smaller length scales.
- **High voltage power supply**
  Using a high voltage power supply results in faster, more energy efficient tuning. Faster tuning also decreases the effect of the disturbances on the actuated dynamic system caused by the tuning process.

Build a prototype Tunable Magnet and validate the proposed tuning method

A setup has been build with two TM actuators. One based on AlNiCo 5 and one based on AlNiCo 6 to also evaluate the possible improvement in TM performance due to using a different magnetic material. Both implementations are based on the simple gap-closing reluctance actuator topology, used for analysis throughout this thesis (Fig. 1.1). However, the mover is placed on a manual linear precision stage and is therefore not able to move freely. This limits the evaluation of the proposed magnetization state tuning method to the case where the air-gap is constant during a tuning cycle.

Using this method we have achieved magnetization state tuning for the AlNiCo 5 TM with maximum error and minimum precision as shown in Tab. 4.1.

B_g^{set}	Max. Error	Min. precision 3σ
$0.175\,\mathrm{T}$	$25.35\,\mathrm{mT}$	$1.27\,\mathrm{mT}$
$0 - 0.15\mathrm{T}$	$11.86\,\mathrm{mT}$	

Table 4.1: Tuning performance for AlNiCo 5 TM with $1\,\mathrm{mm} \leq l_g \leq 1.5\,\mathrm{mm}$.

These measurements where conducted for air-gap lengths in the range of $1\,\mathrm{mm} \leq l_g \leq 1.5\,\mathrm{mm}$. In general, the tuning error gets progressively worse with increasing air-gap. This is in part because the power supply is not able to fully saturate the magnet at air-gaps larger than $l_g \geq 1\,\mathrm{mm}$. This effect is especially apparent in set-points close to the remanence magnetization, as is shown in Tab. 4.1, where the tuning error for $B_g^{set} = 0.175$ is more then twice the maximum error for the lower set-points. Another source of tuning error is the limited accuracy of the magnetic circuit model used in the operating point prediction step. For example, the flux leakage and fringing effects will increase, with increasing air-gap. This air-gap dependency needs to be incorporated to increase the accuracy of the prediction step.

The value for the tuning precision is determined by the noise in the control system.

Magnetization state measurements on the AlNiCo 6 TM were not possible because of vibrations in the measurement setup. The finite stiffness of the magnetic circuit components and mounting fixture, combined with the high reluctance forces, caused vibrations in the system. The back EMF produced by these vibrations interferes with the sensor signals and makes magnet tuning impossible. This can be solved by merely increasing the stiffness of the AlNiCo 6 TM measurement setup.

4.2. Towards the Realization of Tunable Magnet Actuators

This research has taken the first step towards the realization of TM actuators. These actuators have the potential to be very efficient in quasi-static actuation tasks and can provide a constant holding force without energy dissipation.

To enable the implementation of TM in actuators, a method has been proposed and implemented to achieve robust magnetization state tuning in the presence of a variable but known air-gap. With the achieved accuracy and precision, already much of the static heat dissipation would be mitigated in a TM actuator since only a small constant bias current is necessary to compensate for the tuning error. However, the robustness of the proposed magnetization tuning method still has to be tested in a situation where the air-gap varies during a tuning cycle, which would be the case in a real actuator.

We have also investigated the use of TMs in actuation systems and have derived the break-even tuning interval metric to evaluate which type of actuation systems can benefit from it. Following this analysis, we concluded that, with a lot of assumptions and in a nominal scenario, the closed loop actuation bandwidth at which the TM actuators can become more energy efficient is in the range of $0.1\,\mathrm{Hz}$. A scaling analysis has shown that this bandwidth increases with decreasing actuator size.

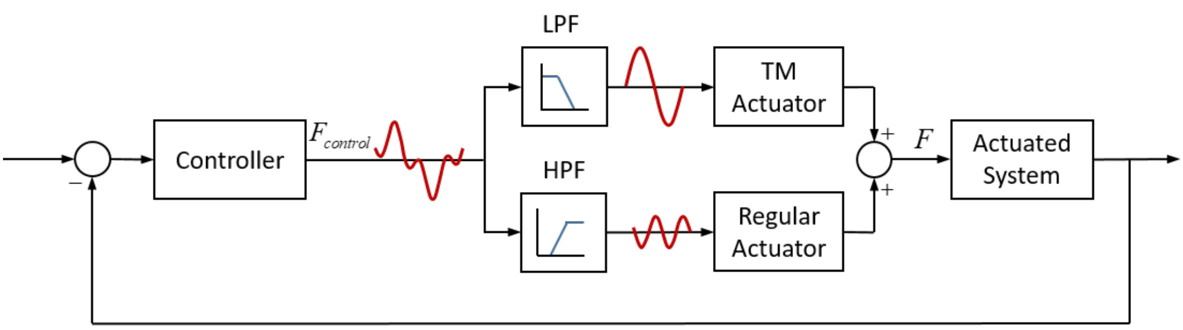

Figure 4.1: Closed loop actuation system with a parallel combination of a TM actuator and a regular EM actuator.

So far, we have only considered a single actuator. However, combining a TM actuator with a conventional actuator as shown in Fig. 4.2 might solve some of the problems associated with both. If a parallel combination of these actuators is used, the control tasks can be divided. The TM actuator can efficiently generate the low-frequency large amplitude part of the required actuator force, while the conventional actuator handles the high-frequency, low amplitude force variations. Using this method yields an actuation system that is both energy efficient through the use of the TM, and at the same time able to have a closed loop bandwidth that is higher than the limits currently predicted by the break-even tuning interval. The parallel actuator can also be used to compensate for the tuning disturbances caused by the TM actuator.

A block diagram representation of a closed loop actuation system that uses this concept is shown in Fig. 4.1. The controller outputs a required control force $F_{control}$. This signal is then split into a high and a low-frequency part using filters, and both are generated by a different actuator. Because the actuators are placed in parallel on the same system, their effect is combined, creating the resulting force F.

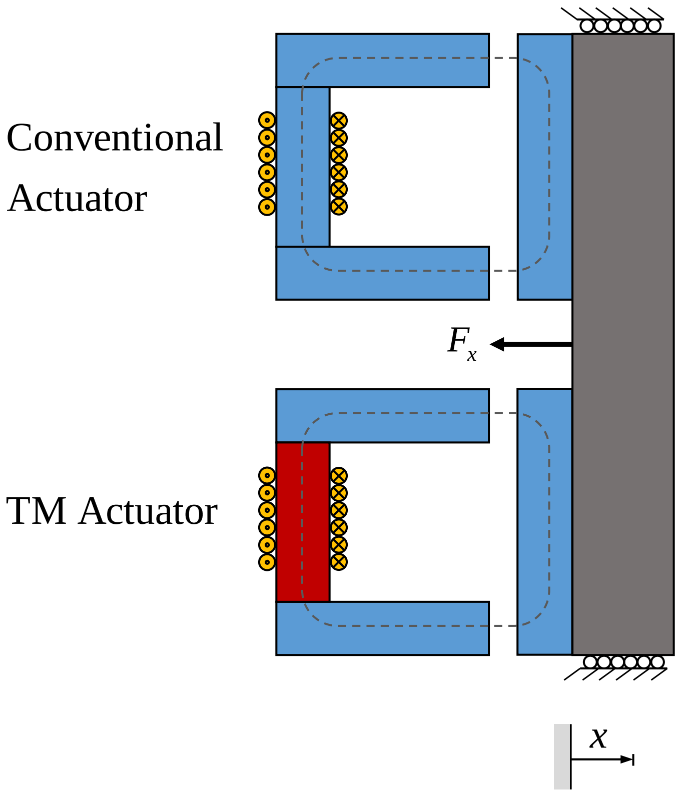

Figure 4.2: Parallel combination of a TM actuator and a conventional actuator.

4.3. Recommendations for Future Work

The TM actuator concept is very promising for energy efficient actuation. However, before it can be practically implemented, a lot of research and development still has to be done. In the hope that the work on TMs will be continued, some recommendations on future work are proposed:

- Increase the magnetization state tuning accuracy by:
  - Developing better electronics such that the magnet can be fully saturated at larger air-gaps.
  - Improving the TM model to enable better operating point prediction.
  - Further investigating the limitations imposed by magnetization dynamic effects.
- Develop a demonstrator of a real TM actuator to investigate:
  - Robustness of the magnetization state tuning method against air-gap variation during a tuning cycle.
  - General interaction between the TM actuator and the actuated dynamic system.
  - Validation of the *Break-Even Tuning Interval*
- Explore the concept of combining a TM actuator with a conventional actuator to increase the energy efficient actuation bandwidth.

A

DSPE Conference Paper

This is a summarized version of the paper in chapter 2, which we submitted for the DSPE Conference on Precision Mechatronics, taking place 4 & 5 September in Sint Michielsgestel, The Netherlands.

DSPE YOUR PRECISION PORTAL
Conference on Precision Mechatronics
4 & 5 September | www.dspe-conference.nl
2018

Tunable Magnets: modeling and validation for dynamic and precision applications

Silvan G. Viëtor, Jo W. Spronck, S. Hassan HosseinNia

Department of Precision and Microsystems Engineering (PME)
Faculty of Mechanical, Maritime and Materials Engineering (3mE)
Delft University of Technology

s.g.vietor@student.tudelft.nl

Abstract

Actuator self-heating limits the achievable force and can cause unwanted structural deformations. This is especially apparent in quasi-static actuation systems that require the actuator to maintain a stable position over an extended period. As a solution, we use the concept of a Tunable Magnet. Tunable magnets rely on in-situ magnetization state tuning of AlNico to create an infinitely adjustable magnetic flux. They consist of an AlNiCo low coercivity permanent magnet together with a magnetizing coil. After tuning, the AlNiCo retains its magnetic field without further energy input, which eliminates the static heat dissipation. To enable implementation in actuation systems, the AlNiCo needs to be robustly tunable in the presence of a varying system air-gap. We achieve this by implementing a magnetization state tuning method, based on a magnetic circuit model of the actuator, measured AlNiCo *BH* data and air-gap flux feedback control. The proposed tuning method consists of 2 main steps. The prediction step, during which the required magnet operating point is determined, and the demagnetization step, where a feedback controller drives a demagnetization current to approach this operating point. With this method implemented for an AlNiCo 5 tunable magnet in a reluctance actuator configuration, we achieve tuning with a maximum error of $15.86\ \mathrm{mT}$ and a minimum precision of $0.67\ \mathrm{mT}$ over an air-gap range of $200\ \mu\mathrm{m}$. With this tuning accuracy, actuator heating during static periods is almost eliminated. Only a small bias current is needed to compensate for the tuning error.

Keywords: tunable magnet, electropermanent, magnetization state tuning, thermal stability, precision actuation, AlNiCo 5, recoil permeability

1. Introduction

One of the challenges in modern precision actuation systems is thermal stability. Heat dissipated in the actuator coils can cause unwanted structural deformations and therefore limits the achievable force and accuracy of the system [1][2]. This is especially a concern in quasi-static actuation systems, where the actuator needs to maintain a stable stationary position over an extended period. During this time the actuator is still dissipating heat to produce the required static force. In this paper, we use a concept called a *Tunable Magnet* (TM), which has the potential to increase energy efficiency and therefore thermal stability in precision actuation systems. A TM consists of an AlniCo low coercivity permanent magnet (PM) combined with a coil to in-situ adjust its magnetization. After magnetizing, the AlNiCo retains its magnetic field without further energy input. TMs can therefore significantly reduce the constant heat dissipation during stationary periods when used in actuators. Promising applications include set-and-forget alignment systems, adjustable magnetic gravity compensators [2][3] and highly stable microscopy stages.

The idea of using in-situ magnetization adjustment of AlNiCo has been the subject of prior research. In 2010, A.N. Knaian [4] introduced the Electropermanent Magnet. It consists of an AlNiCo 5 magnet in parallel with a NdFeB magnet, together with a magnetizing coil. Changing the polarization of the low coercivity AlNiCo magnet with a pulsed external field effectively switches the magnet assembly 'On' and 'Off'. Devices that rely on in-situ tuning, as opposed to switching, of magnetization of AlNiCo have been realized for magnetic clamping applications [5-7], flux weakening/boosting in PM motors [8-10] and force tuning in a magnetic gravity compensator [2][3].

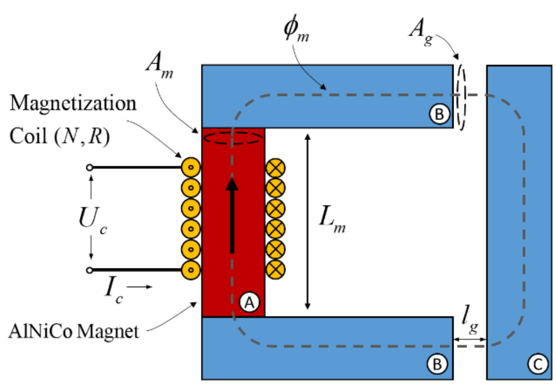

Figure 1: Schematic of Tunable Magnet actuator with AlNiCo magnet [A], soft steel pole pieces [B] and keeper bar [C].

The main challenge in implementing the TM concept is how to determine the correct coil current to tune the magnet to the desired strength. This magnetizing current depends on both the present magnetization state and the reluctance of the magnetic circuit in which the TM is placed. In actuation applications, this reluctance varies, usually due to a changing air-gap. Some research has been done on trying to predict the magnetizing current using models or measurements. For example, [9] and [10] base their estimate on a parallelogram-shaped hysteresis curve approximation, combined with a simple magnetic circuit model. However, small deviations due to model inaccuracy and geometry tolerances can lead to substantial differences in resulting magnet strength, because the magnetization of the AlNiCo 5 magnet being used is very sensitive to variations in the applied field. To overcome this, [2] uses measurements of the AlNiCo *BH* characteristic to determine the magnetizing current. By entirely demagnetizing before each tuning step, only a single measured curve is needed, because the starting magnetization condition is always identical. This leads to good repeatability at a fixed actuator position but attained magnetization values will still change with changing system air-gap.

This work aims to develop a TM that can be robustly tuned in the presence of a varying system reluctance, in order to enable its implementation in actuation applications. We achieve this by implementing a magnetization state tuning method based on measurements of AlNico *BH* data, a magnetic circuit model, and air-gap flux feedback control. In the current implementation, we use AlNiCo 5, but the method presented can be used for other grades of AlNiCo and potentially other low coercivity PMs as well.

The rest of this paper is organized as follows: Section 2 describes the operation of PMs and derives the magnetic circuit model. In section 3 this model is used to develop a magnetization state tuning method. Part of this method is a demagnetization controller which is elaborated in section 4. The experimental setup and measurement results are reported in section 5. Section 6 concludes on these results and gives an outlook on the use of TMs in precision actuation systems.

2. Modeling and Permanent Magnet Operation

In this research, we assume that the *Tunable Magnet* is applied in a standard gap closing reluctance actuator topology, as shown in Fig 1. The system consists of the AlNiCo PM [A] with length L_m and cross-section A_m together with a magnetizing coil. The coil has N number of turns which carry a current I_c supplied by a voltage source U_c. The resulting coil resistance is denoted by R. Soft steel pole pieces [B] with cross section A_g are on both sides of the magnet, and a soft steel keeper bar [C] completes the magnetic circuit. Applying conservation of flux and evaluating Ampere's Law over the contour ϕ_m, gives the following lumped parameter model of the TM actuator [11]:

$$B_m A_m = k_1 B_g A_g \quad (1)$$
$$H_m L_m + 2\, k_2 H_g l_g = N I_c \quad (2)$$
$$B_g = \mu_0 H_g \quad (3)$$

where B_m and B_g are the magnetic flux densities in the magnet and the air-gap respectively. The magnetic field intensities are denoted by H_g and H_m. In the air-gap, H_g and B_g are related through the permeability of free space μ_0. Parameter k_1 is known as the flux leakage coefficient which describes how much of the flux going through the magnet actually arrives in the air-gap. It compensates for the effects of flux leakage and fringing flux. Parameter k_2 is the loss factor, which accounts for the potential magnetomotive force loss due to unwanted magnetization of the steel components.

The behavior of PMs in a magnetic circuit is usually described by a load-line [11]. For the magnetic circuit of Fig. 1, the load-line equation can be written by combining (1), (2) and (3) as:

$$B_m = -\mu_0 \left(\frac{k_1}{k_2}\right) \frac{A_g L_m}{2\, A_m l_g} \left(H_m - \frac{N I_c}{L_m}\right) \quad (4)$$

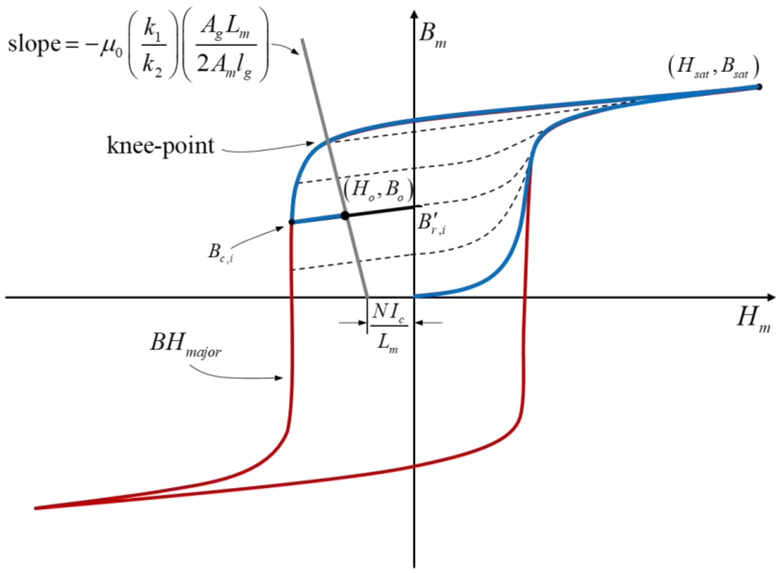

Figure 2: Major *BH* curve (red) with a load-line (grey) and operating point (H_o, B_o). An arbitrary magnetization state trajectory (blue), ending on an example recoil line (black) with associated remanence $B'_{r,i}$ and corner-point $B_{c,i}$ is also drawn. The dashed lines are other possible recoil lines.

It relates the field intensity H_m in the magnet to the resulting magnetic flux density B_m. In order to determine the magnet's operating point, another such relation is required. This is provided by the magnet's hysteresis characteristic, or *BH* curve, shown in Fig. 2. The magnet operates at a point where the load-line intersects this curve, denoted by (H_o, B_o).

Demagnetization of the magnet can be caused by a changing circuit reluctance (slope of the load-line) or an applied magnetizing current (position of the load-line), both of which change the magnet's operating point. An important feature of the *BH* curve is the knee-point, as denoted in Fig. 2. Shifting the operating point past this point will yield a permanent demagnetization and subsequent operation over a recoil line. There exist a continuum of these recoil lines within the major *BH* curve, each of which constitutes a possible level of magnetization with its own associated remanence $B'_{r,i}$. The point where the recoil line intersects the major *BH* curve is denoted by corner-point $B_{c,i}$. The recoil lines are linear with a slope equal to the recoil permeability, noted by relative permeability value μ_{rec} [11].

3. Magnetization State Tuning

The previous section elaborated on modeling the *Tunable Magnet*. This section introduces a magnetization state tuning method based on this model. We assume that the air-gap l_g of the TM actuator from Fig. 1 is variable but accurately known. This is often the case for an actuator, where the position of the mover is measured to be used in motion feedback control. The proposed tuning process is visualized in Fig. 3. It is summarized as follows: if a new level of air-gap flux density B_g^{set} is required, the system predicts at what recoil-line the magnet needs to operate to achieve this for a given l_g. If this recoil-line is higher than the present one, the magnet is saturated by a saturating voltage pulse on the coil. If not, the magnet is immediately tuned to the correct recoil line, where the demagnetizing voltage pulse is generated by an air-gap flux feedback controller. The point (H_o, B_o) where the magnet has to operate to yield a certain required air-gap flux density B_g^{set} is calculated using (1), (2) and (3):

$$B_o = k_1 \frac{A_g}{A_m} B_g^{set} \quad (5)$$

$$H_o = -2\, k_2 \frac{l_g}{L_m\, \mu_0} B_g^{set} \quad (6)$$

The recoil-line that corresponds to this operating point, identified by its remanent magnetization is:

$$B'_{r,i} = B_o - \mu_{rec}\, \mu_0\, H_o \quad (7)$$

During demagnetization, the operating point is shifted over the major *BH* curve in the 2nd quadrant. Therefore, the demagnetization controller reference is equal to corner-point $B_{c,i}$ i.e., the point where the desired recoil line intersects the major hysteresis loop. Demagnetizing to this point guarantees subsequent operation over the correct recoil line. An example magnetization state trajectory, corresponding to an arbitrary tuning cycle starting from $B_m = 0$ is depicted in Fig. 2 in blue.

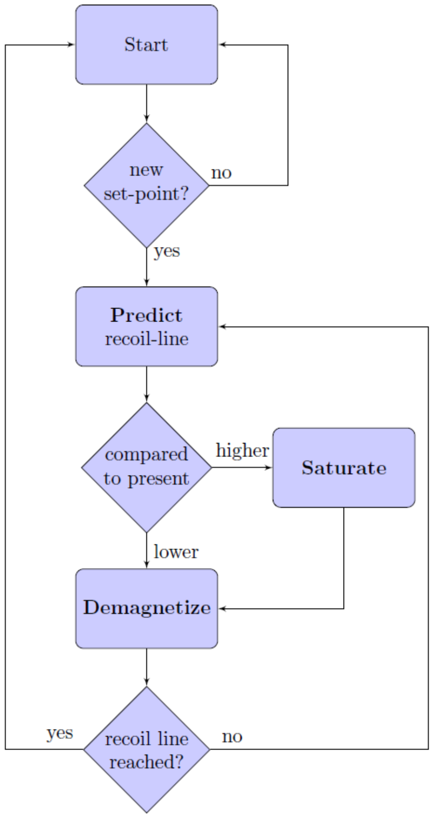

Figure 3: Magnetization State tuning method consisting of 3 steps: **Predict, Saturate and Demagnetize**.

4. Controller Design

To understand the dynamics of the system that the controller is working on, the effect of a coil voltage U_c on the air-gap flux density B_g in the TM actuator is derived. This relation can be described by the following transfer function:

$$G(s) = \frac{B_g(s)}{U_c(s)} = \frac{G_0(\mu, l_g)}{\frac{L(\mu, l_g)}{R} s + 1} \quad (8)$$

where $L(\mu, l_g)$ and $G_0(\mu, l_g)$ are the non-linear inductance and the DC gain of the system. Both are dependent on the magnet permeability $\mu = \frac{dB_m}{dH_m}$, which in term depends on the magnetization state. The plant to be controlled is thus non-linear with a gain that depends on the AlNiCo operating point.

The proposed demagnetization controller has a structure as shown in Fig. 4. Since it uses air-gap flux feedback, the reference input $B_{c,i}$ is first translated to the associated air-gap value using (1). Since demagnetization along the major *BH* curve in the second quadrant is irreversible, it is imperative that the controlled system has zero overshoot. Otherwise, the correct corner-point will be passed, and the magnet will end up operating on an incorrect recoil-line. This also requires the step response to have zero steady state error. A simple PI controller will add 90° of phase, ensuring a damped step response without overshoot. The integrator gives high gain at low frequencies, therefore minimizing steady-state error. The tuned PI controller has the following form:

$$C(s) = k_p + \frac{k_i}{s} \quad (9)$$

where $k_p = 2.07\ \mathrm{V\,T^{-1}}$ and $k_i = 150\ \mathrm{V\,T^{-1}s^{-1}}$. These controller gains give good performance even with the non-linear plant $G(s)$. A typical step-response of the system is shown in Fig. 7 with the reference input $B_{c,i}$ denoted by the dotted red line.

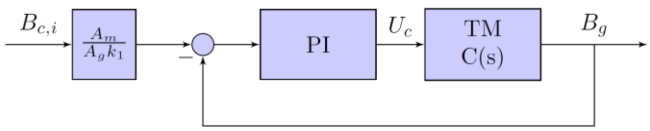

Figure 4: PI demagnetization controller. Reference $B_{c,i}$ is first transformed to the associated air-gap flux density.

5. Experimental results

In this section, we present the hardware implementation of the *Tunable Magnet* and the experimental verification of the proposed magnetization state tuning method. Figure 5 shows the experimental setup with the TM implemented in a reluctance actuator topology, similar to Fig. 1. As PM material we use AlNiCo 5, which is the most common variation with the highest remanent magnetization. The pole pieces and keeper bar are made of soft steel (st. 37). We measure air-gap flux density by combining a hall sensor and a sense coil, to accurately capture both DC and AC values. Both sensors are placed in a 3D printed fixture of 1.00 mm thickness to accurately fix the nominal air-gap width (Fig. 5). The air-gap can then be varied by moving the keeper bar on a manual linear stage (resolution 10 µm). Magnetizing current is provided by a linear power amplifier and measured by the voltage drop over a sense resistor.

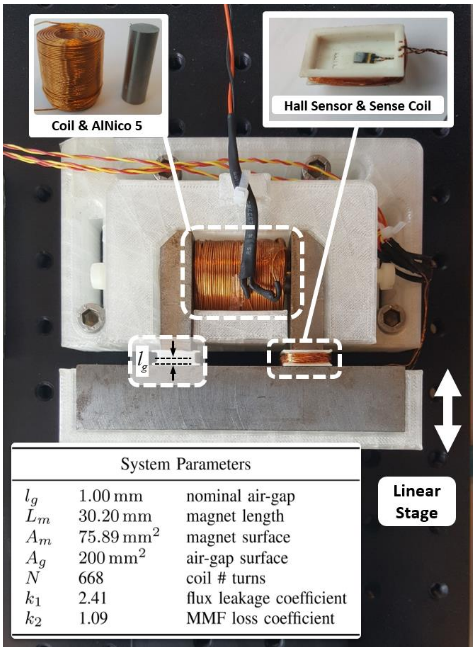

Figure 5: TM measurement setup with parameter values. The keeper bar is mounted on a manual linear precision stage to vary the air-gap.

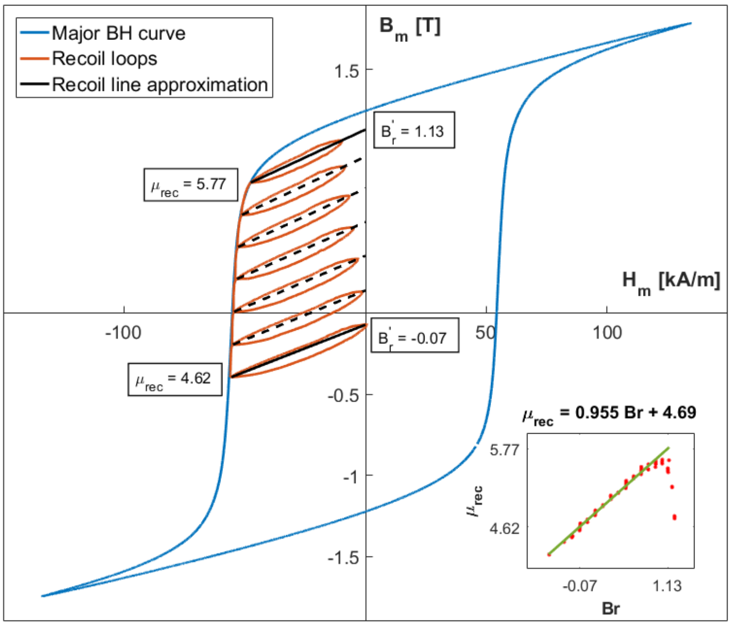

Figure 6: Estimate of the major *BH* curve with recoil-loops using measurements of B_g and I_c together with (1) and (2). The inset shows the distribution of permeabilities μ_{rec} , for recoil-loops at different remanent magnetizations B_r' in the 2nd quadrant.

5.1. BH curve *Characterization:*

To use the earlier derived model, we first need to identify coefficients k_1 and k_2. This is done using magnetic FEA in COMSOL, with a detailed 3D model of the TM reluctance actuator. Next, the AlNiCo 5 is driven through its major *BH* curve at low frequency, as well as several recoil-loops. Current and air-gap measurements from this experiment are then used to estimate H_m and B_m inside the magnet using (1),(2) and (3). This results in the *BH* characteristic shown in Fig. 6. Note that the earlier described recoil-lines are actually small loops, of which the recoil-permeability μ_{rec} and associated remanence $B_{r,i}'$ can be approximated by connecting the corners with a straight line. The inset of Fig. 6 shows the relation between recoil-line position, denoted by B_r' and recoil-line permeability μ_{rec}. Over de second quadrant of the *BH* curve this relation can be approximated as linear:

$$\mu_{rec} = 0.955\, B_r' + 4.69 \tag{10}$$

5.2 Magnetization State Tuning Measurements:

Combining (7) and (10) and solving numerically for B_r' gives the required remanent magnetization for a desired B_g^{set}. Intersecting the associated recoil-line (7) with the measured major *BH* curve gives a value for corner-point and demagnetization controller reference input B_c. With this information the magnetization state tuning method of Fig. 3 can now be implemented.

Figure. 7 shows the air-gap flux density B_g over time for a typical tuning cycle, and Fig. 8 the corresponding magnetization state trajectory in terms of H_m and B_m. Starting from $B \approx 0$ T, the magnet is driven to saturation B_{sat} and demagnetized to the correct corner-point B_c. When the coil voltage is removed the current decays, and the magnetization approaches the desired operating point B^{set}. During the saturation pulse, the BH trajectory does not exactly follow the major *BH* curve. This is due to a dynamic effect called loop-widening [12], caused by induced eddy currents. It does not, however, influence the operating point reached.

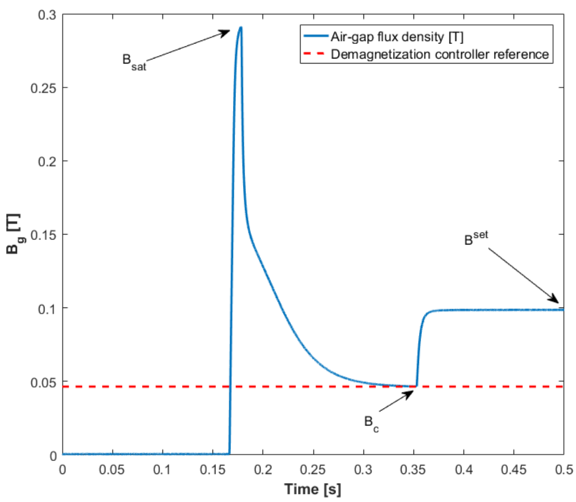

Figure 7: Measured B_g response during a typical tuning cycle, with annotated saturation point, corner point, and flux density set-point.

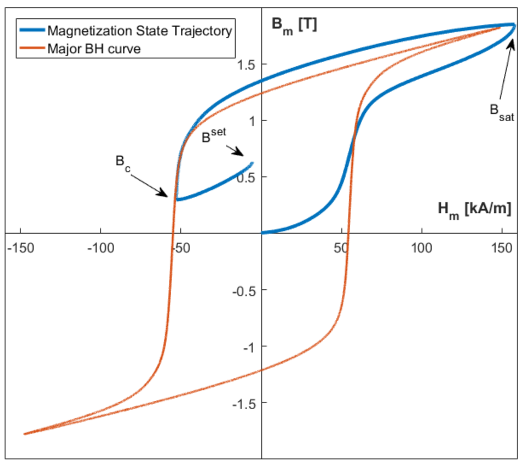

Figure 8: Measured magnetization state trajectory for a typical tuning cycle, with annotated saturation point, corner point and flux density set-point.

With the given demagnetization controller, the time it takes to do a complete tuning cycle is in the order of $500\ \mathrm{ms}$. The exact value depends on B^{set}, l_g and system geometry. The tuning speed can be increased by modifying the controller (9) if enough power supply voltage is available. It is however ultimately limited by dynamic effects such as loop widening.

To evaluate the robustness of the TM implementation, we recorded 44 tuning cycles for different air-gap flux density set-points B_g^{set} at different air-gaps l_g. Tables 1 and 2 show the achieved accuracy, in terms of the MEA (mean absolute error), and the precision (3σ) for $l_g = 1.00\ \mathrm{mm}$ and $l_g = 1.20\ \mathrm{mm}$. Note that the air-gap is constant during tuning. In general, it can be concluded that the tuning error increases with increasing values of B_g^{set}. This is caused by the fact that the absolute value of the error in predicting the operating point is proportional to B_g^{set} according to (5) and (6). The comparatively large error at $B_g^{set} = 0.175\ \mathrm{T}$ can be explained by the added inaccuracy in approximating the distribution of μ_{rec} as linear. For recoil lines approaching the major *BH* curve, this approximation becomes invalid, as shown in Fig. 6. Comparing the results for both air-gaps, we see that the error increases with increasing l_g. This mainly due to the limited accuracy of the used magnetic circuit model. For example, the flux leakage and fringing effects will increase with increasing air-gap i.e., k_1 is air-gap dependent. The more the air-gap deviates from the nominal value at which the model was identified, the larger the operating point prediction error and consequently the tuning error.

Table 1,2: Tuning performance results over n = 44 tuning cycles for each B_g^{set}at different l_g.

B_g^{set}	Realized values		$l_g = 1.00\ \mathrm{mm}$
	Mean	MAE*	Precision (3σ)
0.175 T	0.167 T	7.61 mT	0.67 mT
0.150 T	0.146 T	4.30 mT	0.10 mT
0.125 T	0.122 T	2.62 mT	0.11 mT
0.100 T	0.099 T	1.37 mT	0.13 mT
0.075 T	0.074 T	0.50 mT	0.11 mT
0.050 T	0.050 T	0.16 mT	0.10 mT
0.025 T	0.026 T	0.72 mT	0.14 mT
0.000 T	0.001 T	1.07 mT	0.11 mT

* = Mean Absolute Error

B_g^{set}	Realized values		$l_g = 1.20\ \mathrm{mm}$
	Mean	MAE*	Precision (3σ)
0.175 T	0.159 T	15.86 mT	0.11 mT
0.150 T	0.140 T	9.88 mT	0.60 mT
0.125 T	0.118 T	7.48 mT	0.19 mT
0.100 T	0.094 T	6.04 mT	0.40 mT
0.075 T	0.070 T	5.14 mT	0.53 mT
0.050 T	0.045 T	4.54 mT	0.54 mT
0.025 T	0.021 T	4.10 mT	0.56 mT
0.000 T	−0.004 T	3.81 mT	0.15 mT

6. Conclusion

In this paper, we have presented a way of implementing a *Tunable Magnet*, which enables it to be used in actuation applications. It was shown that robust magnetization state tuning for a variable but known air-gap could be achieved. This is accomplished by predicting the right operating point for the AlNiCo 5 PM, based on measured *BH* data and a magnetic circuit model. An air-gap flux feedback controller is then used to generate the demagnetizing current such that the magnet approaches this operating point. If necessary, the magnet is saturated first. Using this method we have achieved magnetization state tuning with a maximum error of $15.86\ \mathrm{mT}$ and a minimum precision of $0.67\ \mathrm{mT}$, for air-gap flux density set-points in the range of $0 \leq B_g^{set} \leq 0.175\ \mathrm{T}$. This was done for air-gaps in the range of $1.00\ \mathrm{mm} \leq l_g \leq 1.20\ \mathrm{mm}$. With the obtained tuning accuracy, actuator heating during static periods is almost eliminated. Only a small bias current is needed to compensate for the tuning error. Tuning times are in the order of $500\ \mathrm{ms}$ per cycle, but can be increased by modifying the demagnetization controller. Ultimately, the tuning speed is limited by the magnetization dynamics of the AlNiCo PM used.

During the tuning cycle, the air-gap was fixed. The next step toward a functional TM actuator is to evaluate the performance of the proposed tuning method in a situation where the air-gap is actually varying during the tuning cycle. Also, the accuracy of the operating point prediction step can be increased by using a more accurate magnetic circuit model, and a better fit for the recoil permeability distribution. The applicability of the TM can be improved by changing the demagnetization controller to increase the tuning speed. Exact characteristics of the quasi-static applications in which the TM increases energy efficiency also need to be investigated and precisely defined.

References

[1] Lomonova E A 2010 Advanced Actuation Systems -State of the Art: Fundamental and Applied Research *Int. Conf. Electr. Mach. Syst.* 13–24

[2] Hüfner T, Radler O, Ströhla T, Sattel T, Wesselingh J, Vogler A, Eicher D 2017 A note on electromagnetic gravity compensation actuators based on soft electro-permanent magnets for adjustable reluctance force *17th Int. EUSPEN Conf. Proc.*

[3] Wesselingh J 2016 Anordnung zur Halterung eines Bauteils in einer Lithographieanlage sowie Lithographieanlage *Patent DE102015201096A1*

[4] Knaian A 2010 Electropermanent magnetic connectors and actuators : devices and their application in programmable matter *PhD MIT*

[5] Marchese A D, Asada H, Rus D 2012 Controlling the locomotion of a separated inner robot from an outer robot using electropermanent magnets *IEEE Int. Conf. Robot. Autom*. 3763–3770

[6] Ward P, Liu D 2012 Design of a high capacity Electro Permanent Magnetic adhesion for climbing robots *IEEE Int. Conf. Robot. Biomimetics* 217–222

[7] Ochoa-Cardenas F Dodd T J 2015 Design of an active magnetic wheel with a varying Electro-Permanent Magnet adhesion mechanism *IEEE Int. Conf. Intell. Robot. Syst.* 3340-3345

[8] Ostovic V 2001 Memory motors-a new class of controllable flux PM machines for a true wide speed operation *Conf. Proc. 2001 IEEE Ind. Appl. Conf.* **4** 2577–84.

[9] Liu C Chau K T Qiu C 2014 Design and Analysis of a New Magnetic-Geared Memory Machine. *IEEE Trans. Appl. Supercond.* **24** 1–5

[10] Wang Q, Niu S. 2015 Electromagnetic design and analysis of a novel fault-tolerant flux-modulated memory machine *Energies* **8** 8069–8085

[11] Campbell P 1994 Permanent Magnet Materials and their Design (Cambridge University Press)

[12] Mackenzie I 2015 Design and control methods for high-accuracy variable reluctance actuators *PhD thesis MIT*

B

Tunable Magnet Material Alternatives

B.1. Introduction

In previous work, AlNiCo 5 has always been used in devices that require in-situ magnetization state tuning. This has several reasons. First of all, AlniCo 5 has the highest remanence of the existing AlNiCos. Because of that, it is also the best available AlNiCo grade. Other grades are harder to find or need to be custom manufactured. Another factor that makes AlNiCo 5 attractive is that its remanence is comparable to that of NdFeB magnets, so it can be used in electropermanent magnet devices [26].

This chapter elaborates on the material properties that are favorable for TMs. Using these AlNiCo 6 is identified as possibly being a better alternative to AlNiCo 5. An experimental setup was made using AlNiCo 6, its performance as a TM, however, could not be evaluated due to practical difficulties.

B.2. Ideal Tunable Magnet Material

Figure B.1 shows the 2nd quadrant BH-curves, more commonly known as demagnetization curves, of several types of AlNiCo.

An ideal TM material has 3 properties:

- High remanence B_r
- Moderate coercivity H_c
- Low sensitivity $\left(\frac{dB}{dH}\right)_{max}$

A high remanent flux makes the TM more versatile, as it can also be used in applications that require high forces or torques. The coercivity should be low enough to allow modification of the magnetization when required, but high enough to withstand unwanted demagnetization. The slope of the demagnetization curve, $\frac{dB}{dH}$, signifies the sensitivity of the magnetic flux density to a change in the magnetic field intensity. Irreversible demagnetization, used to tune the magnet, usually occurs in the region where this slope has its maximum value. Therefore, a small unwanted perturbation in the applied field will lead to a significant variation in the resulting magnetization state in case of a high $\frac{dB}{dH}$. The effect of this high sensitivity was also demonstrated in the introduction example where the acquired magnetization varied significantly with a change in air-gap (Fig. 1.4). Because of this, the lower the magnetization sensitivity $\frac{dB}{dH}$, the more robust the magnet tuning.

These three properties are however mutually exclusive, so a trade-off has to be made. From Fig. B.1 it can be seen that AlNiCo 6, in general, has the best combination of the desirable features. It combines a still reasonable remanence with a sensitivity that is lower than that of AlNiCo 5. Appendix I contains the demagnetization curves of several more grades of AlNiCo.

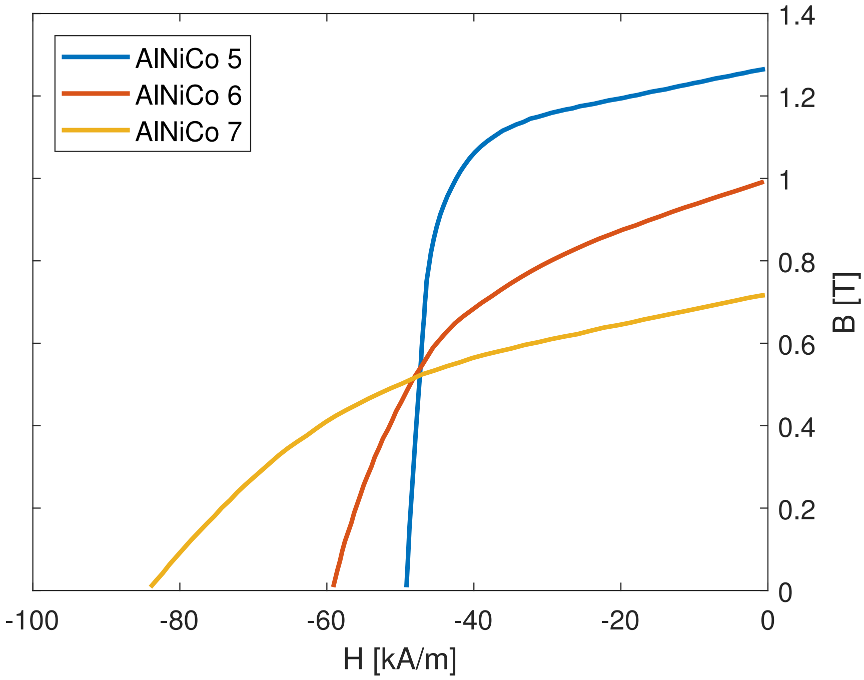

Figure B.1: 2nd quadrant BH-curves for several grades of AlNiCo. Data taken from [62].

B.3. Experimental Results

To evaluate AlNiCo 6 as a TM material and compare the results to AlNiCo 5, we have also implemented a test setup containing an AlNICo 6 TM, as shown in Fig. B.2. The design procedure was similar to the one described for ALNiCo 5 in appendix D and the resulting properties are listed in appendix E.

When doing measurements of the major BH curve, however, some part of the system starts to vibrate. This is most likely a result of the strong reluctance force combined with the finite stiffness of the fixture that holds the magnetic circuit components together. The back EMF resulting from these vibrations makes measuring the hysteresis characteristics impossible. Figure B.3 shows the coil current I_c and the air-gap flux density B_g for a sinusoidal input voltage. The expected shape of the signal is clearly visible, but it is filled with oscillations.

B.4. Conclusion

Due to the shape of its demagnetization curve, AlNiCo 6 better suited as a TM material. It still has a high enough remanent flux density to be useful, and its BH curve is less steep in the irreversible demagnetization region. This makes it less sensitive to unwanted perturbations in the demagnetizing field, therefore facilitating more robust magnet tuning.

However, this has not been tested by measurements, because the AlNICo 6 TM measurement setup starts to vibrate when a magnetizing current is applied. This is probably due to the finite stiffness of the plastic fixture that holds the magnetic circuit components together. The back EMF resulting from the vibrations renders the measurements unusable. This issue can be solved by redesigning the measurement setup for better stiffness.

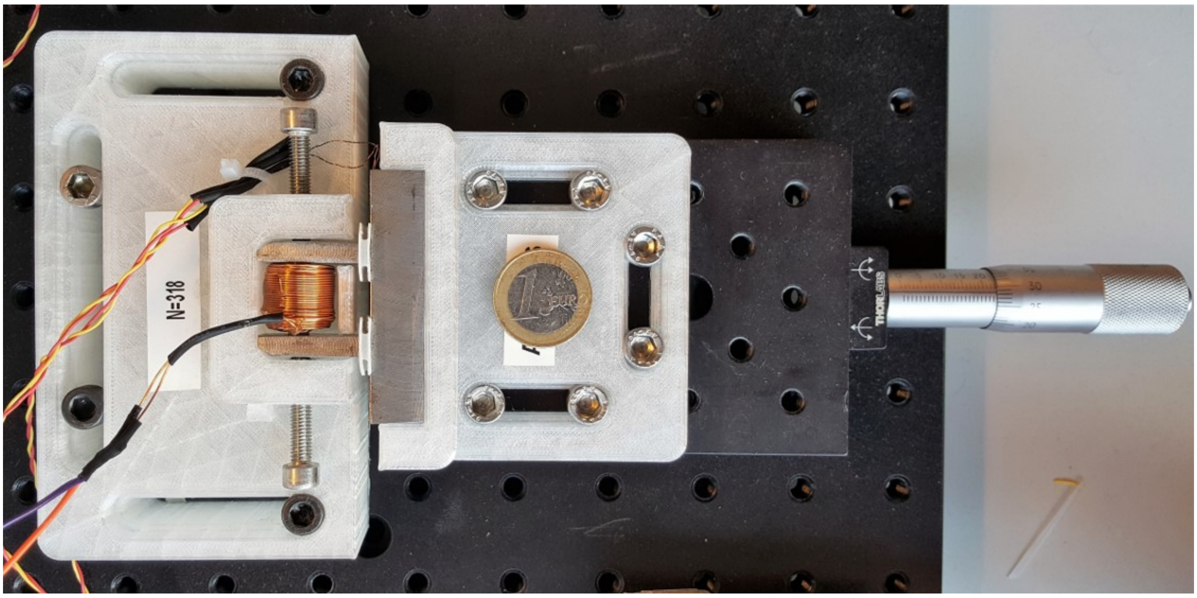

Figure B.2: AlNiCo 6 TM measurement setup

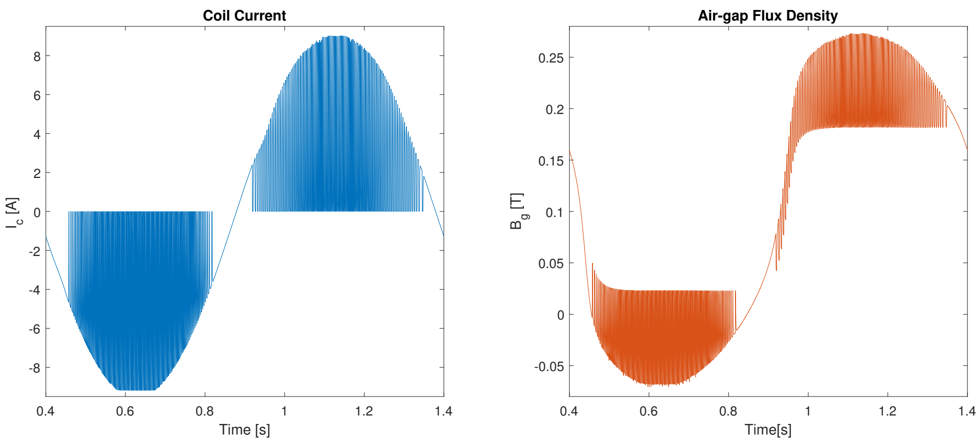

Figure B.3: AlNiCo 6 TM measurement setup response. Shown are the coil current I_c and air-gap flux B_g as a result of a sinusoidal input voltage

C

Extended Literature Review

The TM actuator concept introduced in this thesis is an example of a system that uses in-situ magnetization state tuning of permanent magnet material. This concept has a wide variety of applications, which can be subdivided into the following categories:

1. Magnetic clamping
2. Flux weakening or boosting in PM motors
3. Magnetic gearing
4. Magnetic actuation

This section will investigate the state-of-the-art in research and application of the TM concept in each of these categories.

C.1. Magnetic Clamping Applications

Magnetic clamping applications rely on a magnetic force to hold objects in place. One of the first to propose such a magnetic clamping system based on magnetization state tuning of a PM was a patent by *D. Pignataro* [49]. Inspired by this, *A.N. Knaian* introduced the concept of an *Electropermanent magnet* in his PhD thesis done at MIT, titled: *Electropermanent Magnetic Connectors and Actuators: Devices and Their Application in Programmable Matter* [26]. The main use of this concept is to provide a switchable, energy efficient magnetic connection, to be used in small universal building blocks known as *Programmable Matter*. Around the same time, [6] used the same electropermanent magnet idea in a switchable magnetic chuck, used for fixing work-pieces in place during machining.

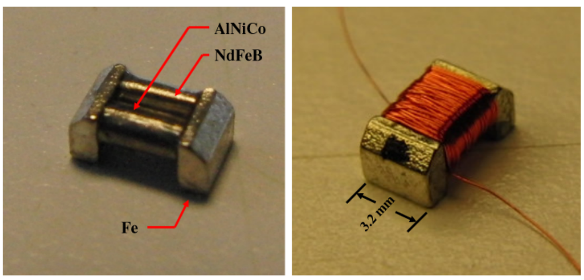

Figure C.1: Electroperment Magnet (EPM) [26]

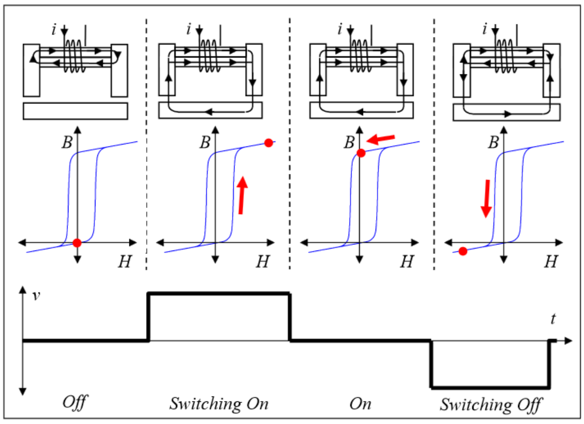

Figure C.2: EPM working principle [26]

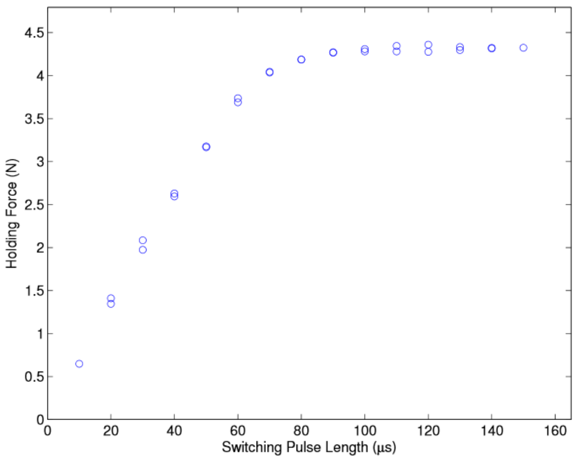

Figure C.3: Holding force of the Electropermanent magnet as a function of the length of the 20V pulses used to switch the magnet [26].

The electropermanent magnet (EPM) consists of two different PMs joint together by pole pieces of magnetically soft material (iron). One PM has a high coercivity (NdFeB) and the other a low coercivity (AlNiCo 5), both of which have approximately the same remanent flux density. Wrapped around the magnets is a copper coil (see Fig. C.1). In the off-state both magnets are oppositely polarized, meaning the flux circulates inside the two magnets and no force is exercised on the target plate. To switch on the magnet, a short voltage pulse is applied to the coil. The resulting current through the wires creates a magnetic field that changes the direction of magnetization of the AlNiCo while having no effect on the NdFeB due to its much higher coercivity. Now the two magnets are polarized in the same direction, so their flux adds up and flows through the pole pieces and the target plate, creating a magnetic attraction force. Figure C.2 shows the working principle of an EPM. Note that the hysteresis loop shown is for the combination of the AlNiCo and NdFeB magnets. They are placed in parallel, so they both see the same H-field, and their B-fields add up. The resulting BH curve is just the BH curve of AlNiCo but shifted upwards with the remanent flux density of NdFeB.

The effect of varying the switching pulse length on the holding force of the EPM is also investigated by [26] and can be seen in Fig. C.3. The force increases linearly with the switching pulse length until it saturates at a certain level. The varying force levels represent different levels of magnetization of the AlNiCo magnet. This means that the Electropermanent magnet concept described by *A.N. Knaian* not only has two stable states, its force output can also be tuned.

The EPM concept has been applied in different applications since the publication of the Ph.D. thesis by [26]. Google's project Ara, named after the author who worked there as a lead engineer, first used the EPM concept to attach different parts of a modular smartphone together. However, the whole project has recently been discontinued [16] due to commercial reasons. Other researchers have used the concept to actuate valves in microfluidic systems [37] [1] and to manipulate ferrofluids for a micro water droplet actuation system [48]. EPMs were also used in a system developed for magnetic anchoring in surgery and endoscopy [56]. To energy efficiently hold objects under MAVs, with the possibility to release them, [15] also uses the EPM magnet concept. The above applications are all millimeter or centimeter scale. However, the concept is also used on a large industrial scale as a lifting system for large metal objects [53]. EPMs are also used as a way to provide a switchable, energy efficient adhesion mechanism for robots that inspect metal structures [45, 60].

A magnetic clamping application that only uses AlNico magnets was used by [38], which describes the design of a robot that can traverse the skin of an airplane by having an inner robot and outer robot clamped together through magnetic attraction. Figure C.4 shows the robot with large copper coils, at the center of which the AlNiCo magnets are located. Magnetization is achieved by giving each separate coil on or more current pulses from a big power capacitor which is charged by a battery. To modulate the clamping force, the pulse length and thus the amount of energy transferred from the capacitor to the magnet is varied. Complete demagnetization is done by reversing the applied field, pulsing current through the magnetization coils in the opposite direction.

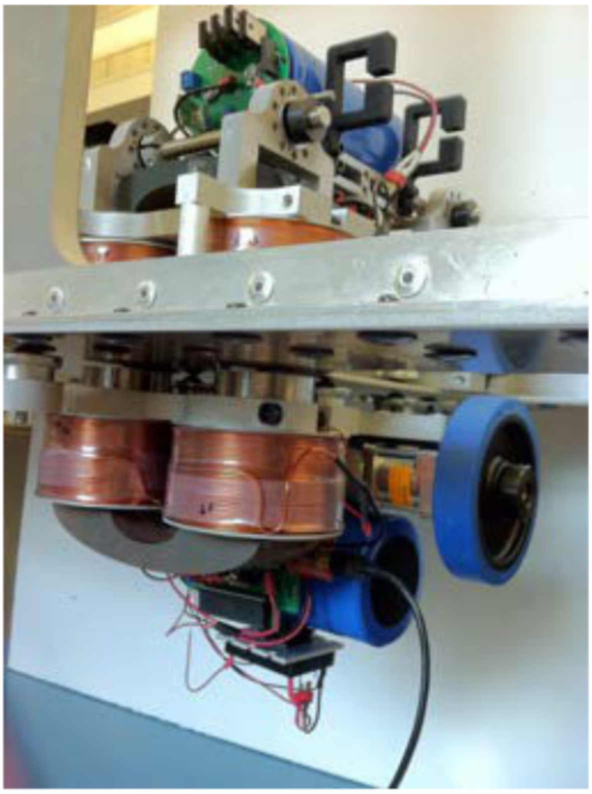

Figure C.4: Robot designed by [38] that uses only AlNiCo magnets to provide adjustable clamping force.

A very similar approach is used in the *NicaDrone Opengrab* system [24]. This is a module that can be mounted under MAV's to carry a load. The load can be locked under the module by pulse magnetizing an AlNiCo magnet that holds a steel target plate with the load attached to it. Releasing the load is then done by demagnetizing the AlNiCo through pulsing the magnet with an alternating field with decreasing amplitude until the magnetization is close to zero.

C.2. PM Motors and Gears

Other systems where in-situ changing of the magnetization state is used are permanent magnet motors.

To achieve a wide operating speed range and optimize motor efficiency over this range, flux weakening or boosting is often used. Permanent magnet motors using this technique are called Variable Flux Permanent Magnet (VFPM) Machines. Different designs are possible, but usually a coil is used with a constant current to increase or decrease the flux in the motor [47]. This constant flux altering current, however, decreases motor efficiency by adding extra copper losses to the system.

To solve this, Ostovic [46] introduced the *Memory Motor* which uses short current pulses to change the magnetization state of permanent magnets in the motor to modulate the total flux. The magnets *remember* the new remanent magnetization level where they are operating on, hence the name of this type of motor. He proposes two methods. Pole changing, where the number of motor poles is effectively varied by completely demagnetizing and/or remagnetizing permanent magnet poles. Another option is flux varying, where the magnetization of the different permanent magnets is tuned to achieve flux modulation. As a PM material, both ferrite and AlNiCo are proposed. The magnetization current in this design is supplied from the same source as the stator current. This complicates the motor control and makes the magnets vulnerable to accidental demagnetization. As a solution, [64] uses a different motor topology where separate windings supply the magnetization current, as shown in Fig. C.5. This concept is further developed in [63].

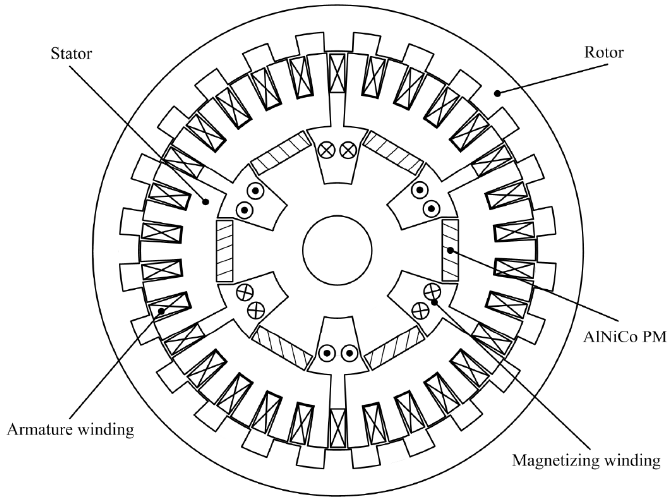

Figure C.5: Memory Motor with separate magnetization windings, as introduced by [64]

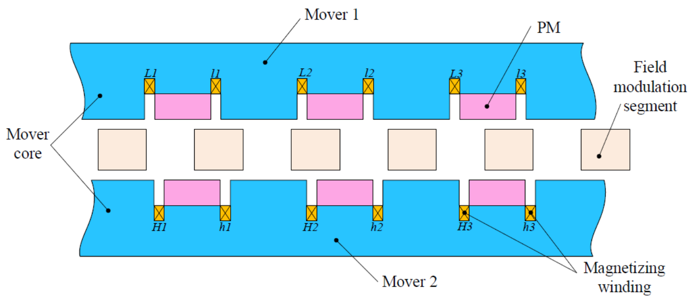

Figure C.6: Linear magnetic gear with adjustable gear ratio, as introduced by [30]

To allow for a wider range of flux weakening/boosting, [13] proposes the *Dual Memory Machine*, which uses a combination of AlNiCo and NdFeB magnets as a source of variable flux. This is effectively an application of the EPM principle [26]. An implementation of the memory machine, with a different motor topology based on the magnetic gearing topology is proposed by [59].

This same magnetic gearing motor topology is also used to implement electrically variable magnetic gears, both rotational [32, 42] and linear [30] (shown in Fig. C.6). These machines use the earlier mentioned pole changing of AlNiCo PMs to achieve various gear ratios.

C.3. Magnetic Actuators

This category contains magnetic actuators that use in-situ magnetization state tuning of a magnetic material to create a varying force. The main difference with the earlier described variable flux memory motors and derived devices is that they only use magnetization tuning to achieve flux weakening/boosting or pole changing. The main flux contribution used to produce motor force is still generated by the armature windings.

A patent by *T. Moennig* first suggests using magnetization tuning of an AlNiCo magnet to achieve precise vertical displacement adjustment in an optical element mounting system. This system is to mount a lens in the optical column of a semiconductor-lithography projection machine. The main components are schematically shown in Fig. C.8. The system consists of an magnet unit (Fig. C.7), denoted by **4**, consisting of an AlNiCo magnet (**3**) and a coil used to change its magnetization (**5**). The magnet unit is part of a lens mounting system (Fig. C.8) and exerts a force on flexures (**16**), which are attached to the lens (**13**). The flexures can displace until they make contact with the surface (**4**) beneath it. This surface has 3 distinct levels (**18, 18a, 18b**), giving the lens actuator 3 possible **Z** positions.

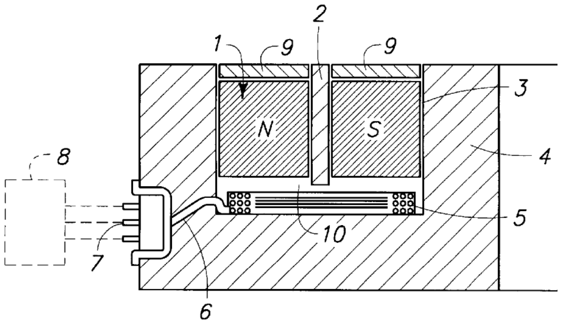

Figure C.7: Magnet unit consisting of an AlNiCo Magnet and magnetizing coil, from [40].

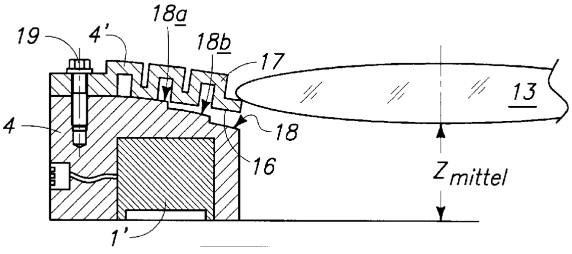

Figure C.8: Mirror mounted on flexures with magnet unit to facilitate vertical displacement adjustment, from [40].

In his PhD thesis [26] and later a patent [25] *A. N. Knaian* also proposes to use the EPM in magnetic actuators. Figure C.9 shows an EPM stepper motor, based on the wobble motor topology. It consists of a stator with 4 EPMs and around which a soft iron rotor is mounted. By using appropriately timed magnetization pulses to switch the EPMs on and off, the motor will produce rotation. The advantage of this concept is that in a situation where there is (almost) no rotation, the static motor force is entirely produced by the permanent magnets without extra energy input. This gives it an efficiency approaching 100 %, as opposed to normal stepper motors that have efficiencies approaching 0% in this situation.

The same patent also contains a proposal for an EPM linear actuator as shown in Fig. C.10. It consists of AlNiCo and NdFeB magnets (**1140, 1130**) and a magnetization coil (**1175**). The air-gaps are denoted by **1160** and **1165**, and a force is produced between the stator and the mover (**1120**). By means of the spring element (**1110**) this force results in an actuator position. By varying the magnetization pulse length as described earlier, the position of the actuator can be controlled.

Another implementation of an actuation system that makes use of in-situ magnetization state adjustment of AlNiCo is the tunable magnetic gravity compensator proposed by [17, 61]. A gravity compensator is a device to hold a certain component in place, and at the same time decouple it from its surroundings to provide vibration isolation. The gravity compensator achieves this by having a flat force-displacement characteristic, i.e., zero stiffness, in addition to providing a fixed compensation force. The magnetic gravity compensator (MGC) uses the forces between several PMs to generate this compensation force. Deviations in the load during operation, however, have to be compensated. An option could be to use an integrated Lorentz actuator in the MCG to provide the extra force, but this results in constant unwanted heat generation.

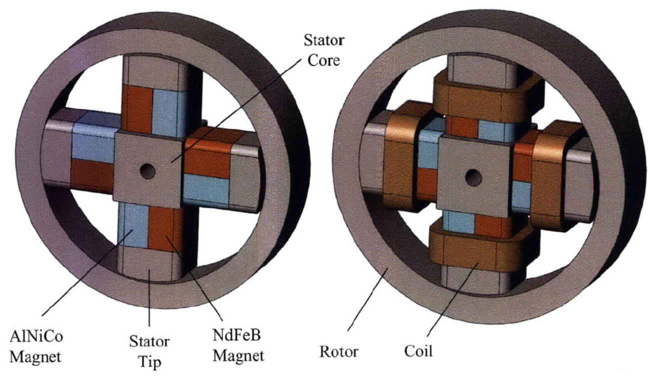

Figure C.9: Wobble stepper motor based on EPMs, as proposed by [25]

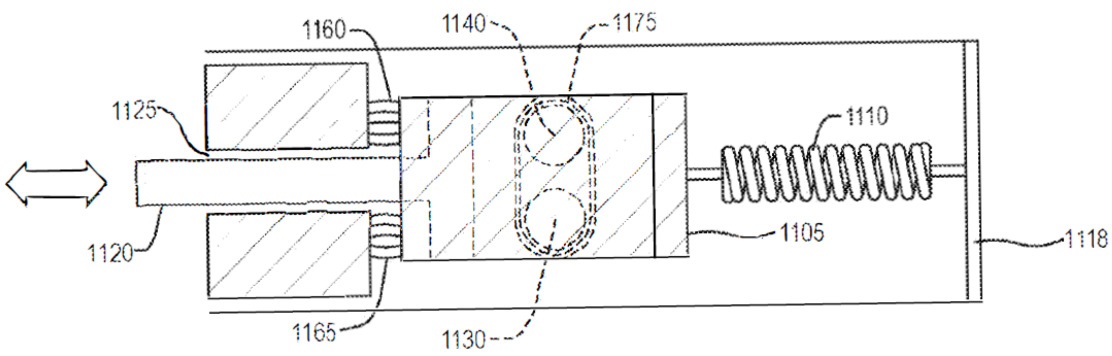

Figure C.10: EPM linear actuator, as proposed by [25].

To solve this, [17] proposes to use magnetization state tuning of AlNiCo to generate an infinitely adjustable magnetization force without power loss in the stationary situation.

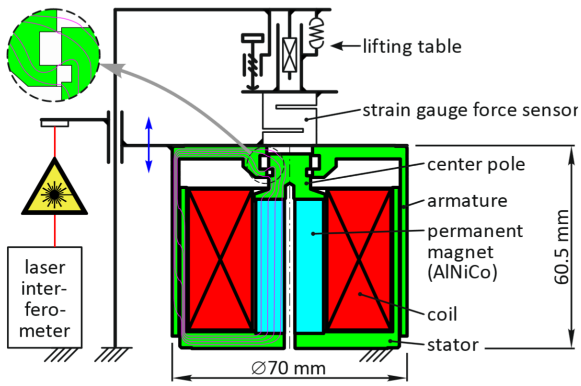

Figure C.11: Magnetic gravity compensator based on soft electro-permanent magnets for adjustable reluctance force [17].

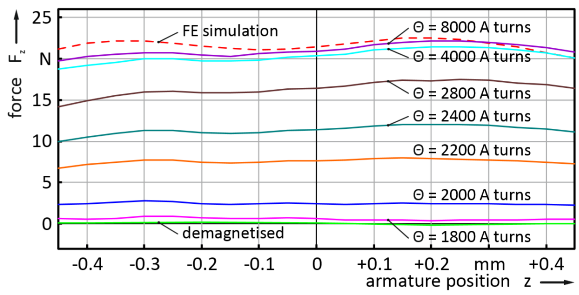

Figure C.12: Resulting force-displacement curves for different levels of magnetization of the AlNiCo magnet.

Figure C.11 shows the implementation of the gravity compensator. The **green** poles have a custom shape near the air-gap, created by FEM optimization to provide the flat force-displacement characteristic. Normally this relation would be of quadratic nature since it is a reluctance actuator. Magnetization state tuning of the AlNico magnet (**blue**) is achieved using current pulses through the coil (**red**). Figure C.12 shows the resulting force-displacement characteristics for different levels of magnetization and the required coil magnetomotive force (MMF) to reach them.

C.4. Determining Magnetization Current

Solutions in literature to the problem of determining the correct magnetizing current to reach a certain desired remanent magnetization can be divided into four main methods:

1. Measured lookup curves & tables
2. Simulated lookup curves & tables using magnetic FEA.
3. Analytic approximations
4. Flux feedback

Most of the state-of-the-art implementations use a magnetization state tuning approach that consists of one or a combination of these methods. This section will investigate the approaches used in prior research presented in the previous section and discuss their limitations and performance.

C.4.1. Switchable Magnets

For switchable magnets, i.e., magnets that only have an ”on” or an ”off” state, finding the magnetization current is straightforward. To magnetize them, the current needs to be large enough to saturate the material thoroughly, but the exact value is not important. Demagnetization to zero is harder since it has the same difficulties as tuning to every other non-saturated state. This can be easier achieved by a process called degaussing, where a sinusoidal current signal with decreasing amplitude is used to drive the magnet to zero magnetization. The same result can be achieved with a correctly chosen series of pulses with decreasing amplitude, as employed by [24]. The EPM concept [26] solves this difficulty of complete demagnetization by using the fact that AlNiCo has approximately the same remanent magnetization as NdFeB. By placing the two types of magnets in parallel, the fields reinforce when the AlNiCo is saturated with the same polarization as the NdFeB. When the AlNiCo is oppositely polarized, the fields cancel, and the magnet combination is effectively switched ”off”. Changing states in this case only requires saturating pulses, which just need to be large enough but not necessarily accurate.

C.4.2. Tunable Magnets

For TM systems that require an infinitely varying magnetization, accurately finding the right current can be difficult.

In most clamping applications, the air-gap is constant, so this only leaves the dependency on starting magnetization and magnetization direction. Saturating the magnet first to fix the starting magnetization then only requires a single characteristic for magnet tuning. This is the case for the EPM [26], where the look-up graph (Fig. C.3) shows the required pulse length in order to achieve a certain force. The same concept to modulate the clamping force is used by [38].

Figure C.13 shows the pulse length and thus energy needed to reach a certain clamping force, starting from a fully demagnetized state. The magnetization experiment for every pulse duration is repeated seven times, so some repeatability figures are given as well.

Most implementations of the *Memory Motor* use magnetic FEM analysis to determine the right current for their flux modulation. To model the AlNiCo hysteresis behavior, [63] introduces a parallelogram shaped, BH curve approximation. This model (Fig. C.14a) is able to represent the major hysteresis loop, as well as recoil-lines using piece-wise continuous linear curves. Coupling this model with FEM analysis of the motor topology (Shown in Fig. C.5) gives the look-up graph needed to determine the correct magnetizing MMF, shown in Fig. C.14b. Note the different curves for each magnetization direction. It is not clear from the paper what initial magnetization condition is being assumed for this look-up graph. The same parallelogram shaped AlNiCo BH approximation is used by [59], in combination with a simple magnetic circuit model to derive an analytical expression for estimating the required demagnetization and remagnetization current.

These methods are both based on an approximation of the AlNiCo hysteresis characteristic. Therefore they only give a rough estimate of the required magnetization current. A distinct advantage that PM motors have, however, is the immediate and easy feedback on the realized magnetization by means of the generated back EMF. Figure C.15 shows this simulated for the memory motor implementation from Fig. C.5 by [63]. After a demagnetizing current pulse, the amplitude of the induced back EMF decreases since the air-gap flux has diminished. This feedback mechanism thus provides a way to precisely calibrate the magnetization current and gives the possibility of real-time air-gap flux control. None of the literature on memory motor implementations gives any data as to the accuracy or precision of magnetization state tuning achieved.

The most elaborate and robust magnetization state tuning method so far is proposed by [17] for their adjustable magnetic gravity compensator (MGC). It consists of the following three steps:

1. Magnetize the AlNiCo above saturation
2. Completely demagnetize the AlNiCo with a reversed polarity current
3. Magnetize to the desired level

Magnetizing Scenarios		
Pulse Duration (ms)	Δ Stored Cap. Energy (J)	B_g (mT)
7	5.18 ± 1.57	191 ± 6
11	13.21 ± 1.05	295 ± 3
15	21.12 ± 2.39	376 ± 6
19	31.51 ± 2.22	431 ± 3
23	42.49 ± 1.33	469 ± 3
27	52.44 ± 1.69	498 ± 3
31	66.08 ± 2.76	522 ± 2
35	79.85 ± 1.81	542 ± 1

(a) Magnetization current pulse look-up table.

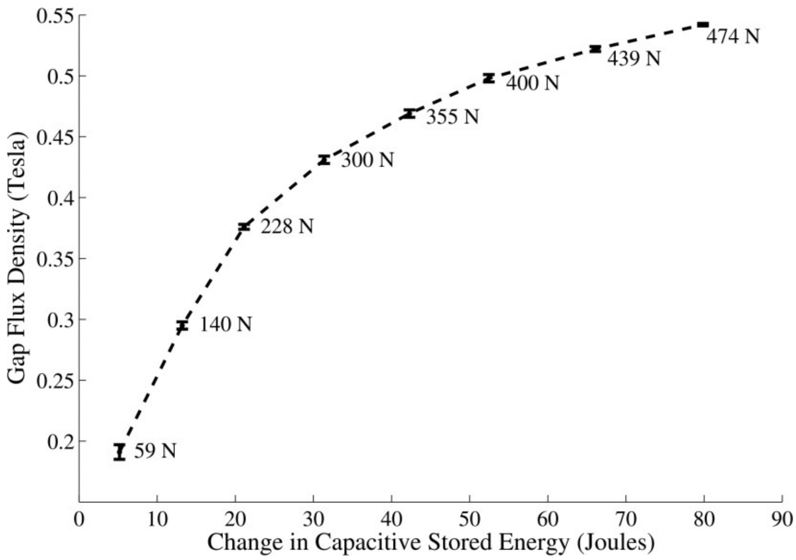

(b) Magnetization energy look-up graph.

Figure C.13: Measurement data from [36] to determine the magnetization pulse length and/or energy needed to achieve a required clamping force at a fixed air-gap. Initial magnetization before each measurement was stated as fully demagnetized.

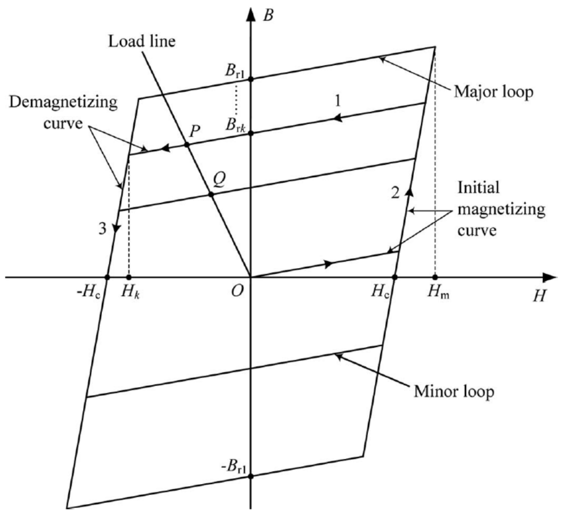

(a) Parallelogram shaped BH curve approximation

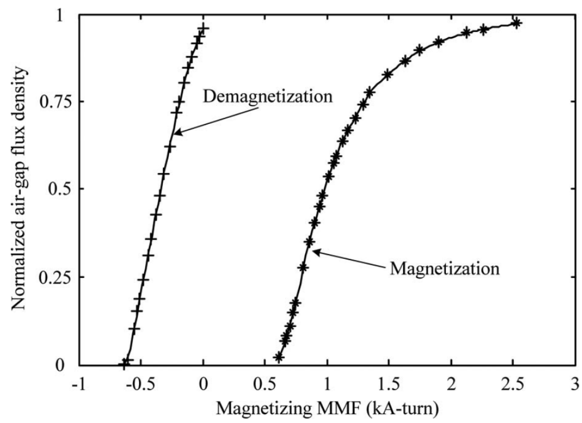

(b) Magnetization MMF look-up graph with different curves for demagnetization and remagnetization.

Figure C.14: Method of determining magnetization current as introduced by [63]. The parallelogram BH curve approximation is coupled to a magnetic FEM analysis of the motor topology to determine the magnetization look-up graph.

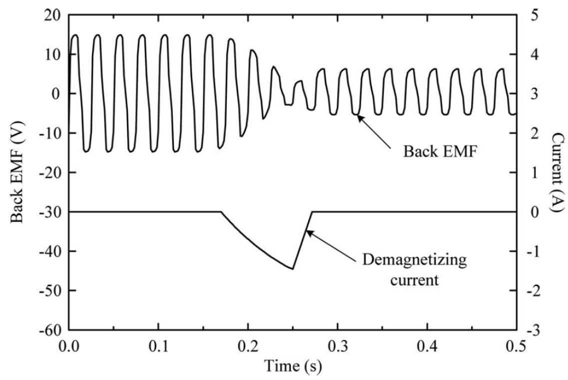

Figure C.15: Back EMF waveform during flux weakening for the memory motor implementation of Fig. C.5, as simulated by [63].

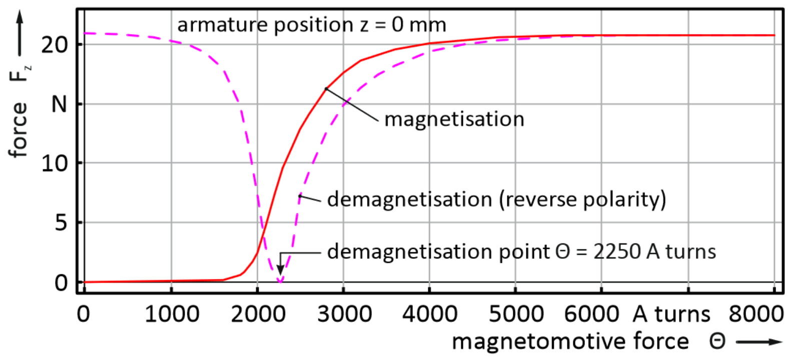

Figure C.16: Magnetization and Demagnetization characteristics for the adjustable magnetic gravity compensator shown in Fig. C.11 [17].

The advantage of this method is that for the final magnetization step only a single look-up table is necessary because the saturation and complete demagnetization step accurately fix the starting magnetization. The reason for starting the final accurate magnetization step in zero instead of, for example, saturation is not elaborated in the paper. The achieved repeatability is stated as within the bounds of the measurement accuracy of the force sensor which is 0.2 % for a range of 100 N. Thus the minimum achieved force tuning repeatability is approximately 0.2 N.

C.4.3. Conclusion

Table C.1 sums up the most important properties of relevant prior applications where some form of in-situ tuning of the magnetization of AlNiCo is being used to modulate an air gap flux or force.

System Characteristics			Magnet tuning performance			
Ref.	**Application**	**Tuning Method**	**Magnet length [mm]**	**Tuning time [ms]**	**Repeatability**	**Allows for variable reluctance?**
[26]	clamping, actuation	look-up graph	3.2	0.1	n/p	no
[38]	clamping	look-up table	76.2	232	6 mT	no
[63]	flux weakening/boosting	analytic approximation, FEM, look-up graph, flux feedback	n/p	n/p	n/p	yes
[59]	flux weakening/boosting	analytic approximation, feedback	n/p	n/p	n/p	yes
[17]	actuation	3 step algorithm with Look-up graph	≈ 60	3000	0.2 N	no

Table C.1: Summary of the magnetization tuning methods used in prior research and their tuning performance.

The tuning method of [17] has the most potential to be used in an actuation application, since it is the most systematic approach and provides the best repeatability. However, the 3-step tuning algorithm does not accommodate magnetization tuning under a varying system reluctance.

D

Measurement Setup Design

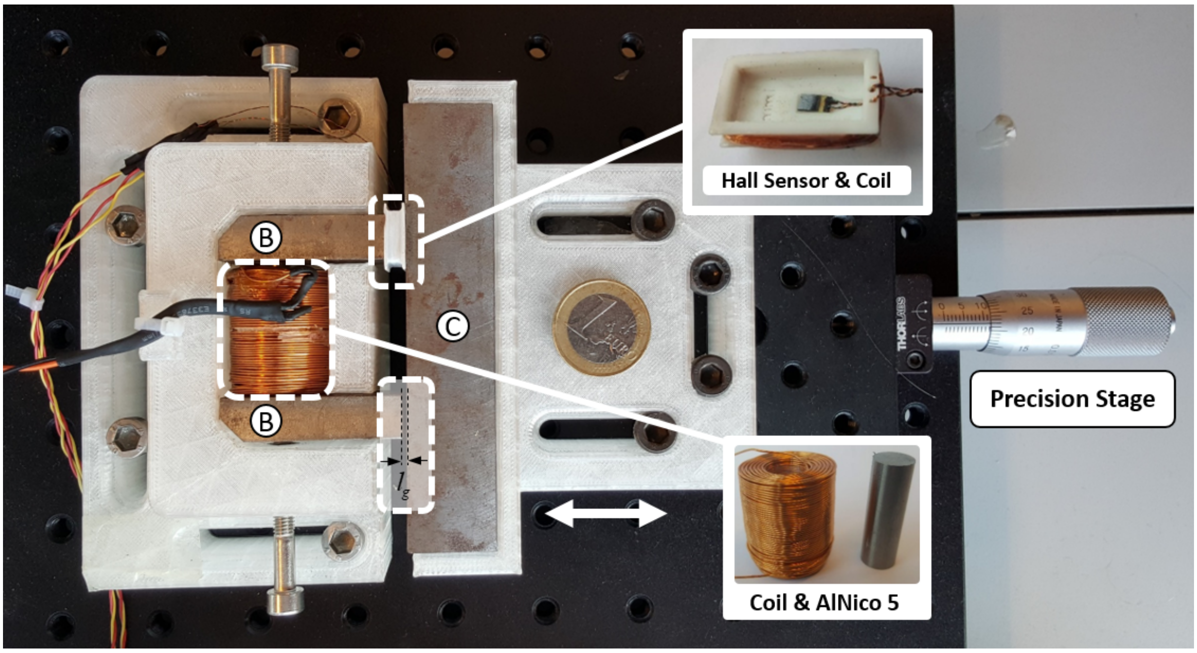

Figure D.1: AlNico 5 TM measurement setup. Annotated are pole pieces [B] and mover [C].

Figure D.1 shows the realized measurement setup for the AlNiCo 5 TM. The associated schematic drawing with required sensors to measure and control the magnetization state is shown in Fig. D.2. This section will go into the design and dimensioning of the measurement setup, the sensors, and electronics. A complete overview of the setup and all dimensions and parameter values can be found in App. E.

D.1. Magnetic Circuit

The magnetic circuit, consisting of the pole pieces [B] and the mover [C] is machined out of St. 37. The pieces are then placed in a 3D printer plastic fixture and clamped to the AlNiCo magnet [A] with plastic screws. The mover part is mounted on a linear precision stage [55] with a resolution of $10\,\mu m$, to be able to precisely adjust the air-gap (shown in Fig. D.1).

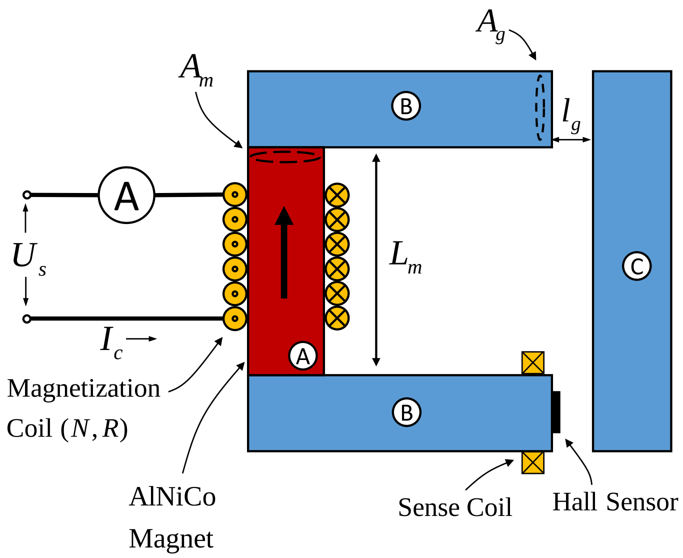

Figure D.2: Schematic view of the TM reluctance actuator measurement setup. The magnetization coil is driven by a voltage source U_s and the current I_c is measured by a current sensor. Magnetic flux density in the air-gap is measured by a sense coil and a hall sensor. Denoted are the AlNICo magnet [A], the pole pieces [B] and mover [C].

D.2. Magnetizing Coil

The magnetizing coil has to provide enough magnetizing MMF to the magnet without too much heat dissipation.

Magnetizing MMF

The required magnetizing MMF can be calculated by taking the Load-Line equation [57], and substituting saturation values for the magnet fields, i.e. $H_m = H_s$ and $B_m = B_r + \mu_0 H_s$. It is necessary to be able to saturate the magnet since this is one of the steps used in the proposed magnetization state tuning method [57]. The saturating MMF can be expressed in system parameters as:

$$\mathcal{F}_s = NI_c = L_m \left[H_s + 2\left(\frac{k_2}{k_1}\right)\left(\frac{A_m l_{g,max}}{A_g L_m}\right)\left(H_s + \frac{B_r}{\mu_0}\right)\right] \tag{D.1}$$

Apart from the general system parameters (Tab. E.1), the required MMF depends on the maximum expected air-gap of the system $l_{g,max}$ and the required magnetic field intensity H_{sat} to saturate the material. This saturation field is not a very well defined quantity, but a rule-of-thumb says that 3 to 5 times the coercivity H_c is enough to completely saturate a magnetic material [8].

Coil Resistance

Next, we derive the coil resistance in terms of system parameters. The resistance of a wire with length l_w is calculated as:

$$R = \rho_c \frac{l_w}{A_w} \tag{D.2}$$

where A_w is the wire cross-section, and ρ_c the resistivity of the wire material. For a magnetizing coil with N turns as shown in Fig. D.3, the total wire length can be expressed using the average coil diameter d_c as:

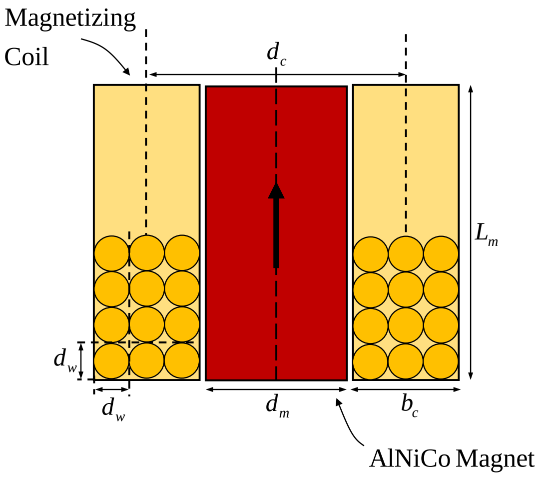

Figure D.3: Cross section of magnetizing coil with AlNiCo PM.

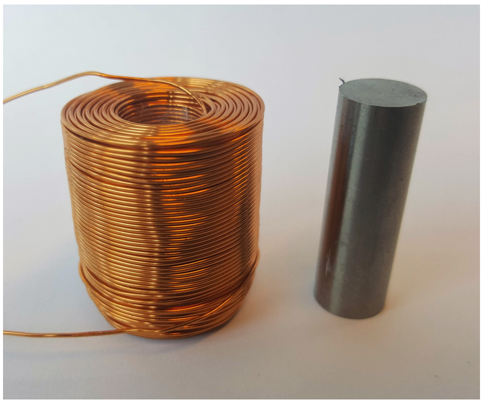

Figure D.4: Realized magnetizing coil and AlNiCo 5 PM

$$l_w = N\pi d_c = (b_c + d_m) \tag{D.3}$$

Assuming square wire packing with a fill factor of γ, we relate the cross-section of the coil $b_c \times L_m$ to the cross diameter of a single wire as:

$$\gamma\, b_c\, L_m = N\frac{1}{4}\pi d_w^2 \tag{D.4}$$

By combining (D.2), (D.3) and (D.4) and assuming that $\gamma = 0.5$ [43], the total coil resistance can be written as:

$$R = 8\frac{\rho_c N^2}{L_m}\left(1 + \frac{d_m}{b_c}\right) \tag{D.5}$$

Equation (D.5) shows that we can decrease the coil resistance by increasing the coil width b_c. However, if b_c is made larger then the magnet diameter d_m, we get diminishing returns when it comes to the decrease in resistance. Therefore we fix $b_c = d_m$, which makes the coil resistance:

$$R = 16\frac{\rho_c N^2}{L_m} \tag{D.6}$$

Coil Dimensioning

First, (D.1) is used to find the MMF required to saturate the AlNiCo magnet. The maximum air-gap width is $l_{g,max} = 1.5\,\text{mm}$. This provides enough air-gap range for testing the magnetization state tuning, while not needing too much saturation current. Combining (D.1), (D.5) and the fact that $U_s = I_c \cdot R$ we can now plot the coil current I_c and supply voltage U_s needed to create a saturating MMF for a coil with a fixed cross section of $d_m \times L_m$ and a variable amount of turns. This relation is shown in Fig. D.5. For the available power supply of $U_s = 30V$, the required number of turns is $N = 525$ with a current of $I_c = 9.72\,\text{A}$. The resulting required wire diameter d_w is evaluated using (D.4) as $d_w = 0.6\,\text{mm}$. Table D.1 summarizes the coil design values for the AlNiCo 5 TM. The realized magnetizing coil is shown in Fig. D.4.

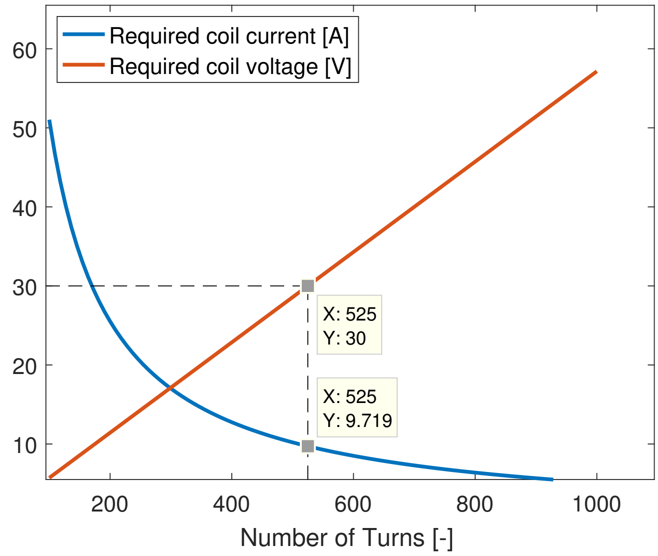

Figure D.5: Design graph showing the relation between the number of coil turns, as well as the voltage and current required to produce a saturating MMF. Valid for the AlNiCo 5 TM actuator setup.

$\mathcal{F}_s$	I_c	N	b_c	d_c	R
5.102×10^3AT	9.72 A	525	10 mm	20 mm	3.1Ω

Table D.1: AlNiCo 5 magnetizing coil dimensioning.

D.3. Driving Electronics

There are two basic ways to control current through an inductive load. Using an H-bridge or a linear power amplifier. This section will investigate their respective properties and choose a suitable concept for driving the TM. The driving circuit has to provide enough bi-directional current to saturate the AlNiCo magnet both ways. This saturation current is derived in the last section (Tab. D.1). The coil drive electronics also need to be able to control the current with a fine enough resolution, as this directly influences the achievable resolution of the magnetization state tuning. The goal is to achieve magnetization state tuning with mT precision.

Figure D.6 shows the 2nd quadrant major BH curve for AlNiCo 5 with a tangent line at maximum magnetization sensitivity. Taking this sensitivity into account, we can estimate the necessary resolution of the current. The effect of a small change in magnetization current on the flux density can be described by [57]:

$$dI = \frac{L_m}{N}\frac{dB}{dH}^{-1} dB \tag{D.7}$$

where dI and dB are small changes in current and magnet flux density. The magnetization sensitivity value is denoted by $\frac{dB}{dH} = \mu_{r,max}\,\mu_0$. Evaluating (D.7) for $dB = 1\,\text{mT}$ yields a value for the current controller resolution of $dI \approx 0.1\,\text{mA}$.

The design requirements of the current drive electronics can be summarized as:

- Current range: $\pm 10\,\text{A}$
- Resolution: $\approx 0.1\,\text{mA}$

The current range is enough to saturate the magnetic material (Tab. D.1), with a little redundant current.

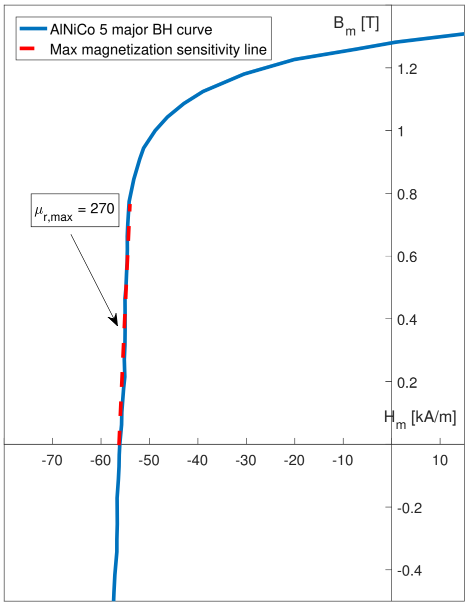

Figure D.6: 2nd quadrant major BH curve of AlNico 5 with maximum sensitivity line. Data from [7]

H-bridge

An H-bridge uses MOSFETs to switch the voltage on the load between zero and the power supply voltage (Fig. D.7). By using Pulse Width Modulation (PWM), the effective (average) voltage on the load can be controlled. H-bridges are very efficient since they only dissipate power internally when the voltage is switched on. This way they can handle very high currents. An example H-bridge is shown in Fig. D.8. It can handle 21A of continuous current without a heatsink while being just $33 \times 20\,\mathrm{mm}$. However, since it uses switching to regulate the voltage, a ripple is imposed on the resulting current signal that is dependant on the PWM switching frequency and the inductance of the load. The peak-to-peak current ripple assuming unipolar PWM can be calculated as [41]:

$$\left(\Delta I_{pp}\right)_{max} = \frac{U_s}{8Lf_{PWM}} \tag{D.8}$$

where U_s is the power supply voltage, L the load inductance and f_{PWM} the PWM switching frequency.

Assuming the magnet relative permeability $\mu_r = 1$, which is the worst case in terms of switching ripple, the minimum magnet inductance can be calculated using [57] as being $L = 1.3\,\mathrm{mH}$. A typical PWM switching frequency is $f_{PWM} = 20\,\mathrm{kHz}$. Using (D.8), this results in a maximum peak-to-peak switching ripple in the current signal of $\left(\Delta I_{pp}\right)_{max} = 139\,\mathrm{mA}$. This is a worst case scenario, as the effective TM inductance will be larger and the current ripple calculated by (D.8) only occurs at a duty cycle of 0.5. Still, with a ripple that is three orders of magnitude higher than the ideal resolution, it is clear that the H-bridge is not good for precise magnetization state tuning.

Linear Power Amplifier

The alternative is to use a linear power amplifier. This is an Op-Amp that has been optimized for large voltages and currents, which can be used in a standard amplifier configuration. The downside of using linear amplifiers is that they are not very efficient, especially at high power supply voltages. The power associated with the difference between the output voltage and the supply voltage is internally dissipated

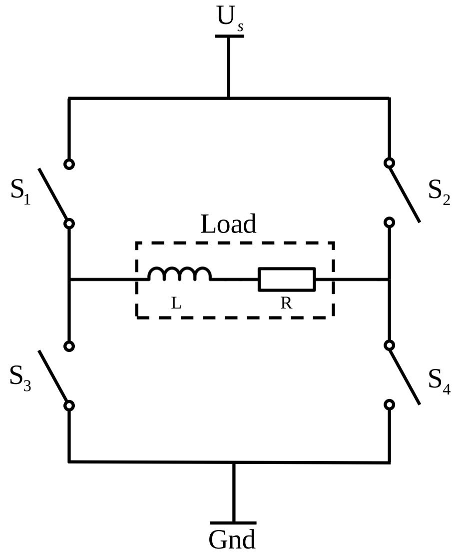

Figure D.7: Schematic of H-bridge with inductive load. Switches $S_1 - S_4$ are usually implemented using MOSFETs

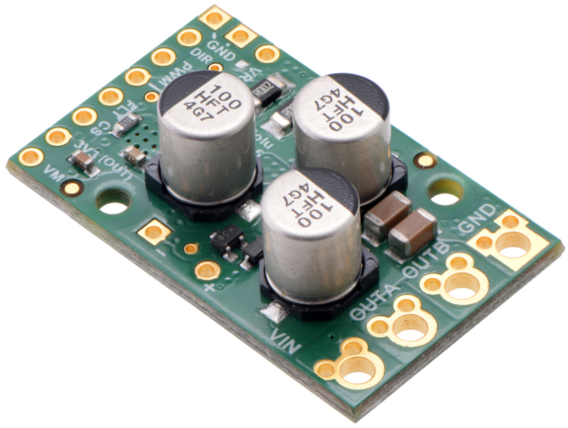

Figure D.8: An example H-bridge from Pololu [50], capable of supplying 21 A without a heatsink while being just $30 \times 33\mathrm{mm}$.

as heat. They do however supply a continuous current, of which the resolution is only limited by the DAC used to generate the amplifier drive signal and the added noise of the amplifier itself. The used linear power amplifier described in App. E.

D.4. Sensors and Signal Conditioning

Figure D.2 shows a 2D schematic of the TM reluctance actuator with added sensors. To track the magnetization state of the material and to implement the proposed magnetization state tuning method, the coil current I_c and air-gap flux density B_g need to be measured [57]. This section will discuss the required sensor characteristics.

First, we will define three important sensor properties:

- **Range:** Range of the input that can be measured by the sensor.
- **Resolution:** Smallest detectable increase in the measured quantity. Resolution is fundamentally limited by the noise level, in the case of an analog sensor signal. When measuring in real-time, the resolution is best specified by the peak-to-peak noise level [31]. At any moment in time, the measured quantity can at most vary by this value. When digitizing a measurement signal, the ADC converter can also limit the resolution of the measurement. However, the ADC of the dSPACE RTI has a resolution of 16-bits over a range of ± 10 V which comes down to a minimum voltage step of $\Delta V = 20 \cdot 2^{-16} = 0.3$ mV, which is usually well within the noise level.
- **Bandwidth:** The bandwidth of a sensor determines up to what frequency changes in the measured quantity can still be detected. It is usually given by the -3 dB cut-off frequency. In a sampled system, the maximum signal frequency that can be represented is limited by the sampling frequency as: $f_{max} = \frac{1}{2} f_s$. This is the known as the *Nyquist–Shannon sampling theorem* [43].

With these definitions, the requirements for the current en magnetic field sensor are summarized in Tab D.2.

The ranges should be enough to measure the saturation current (Tab. D.1) and associated air-gap flux density. The resolution should be good enough to facility a magnetization state tuning resolution in the mT range, as derived in Sec.D.3. However, this is an unrealistic value for a sensor with this measuring range. Even if the noise requirements would be met, the resolution will be limited by the ADC resolution. Therefore 1 mA is chosen as a design requirement. The sampling frequency of the

Sensor	Range	Resolution	Bandwidth
Current	± 10 A	1 mA	≤ 5 kHz
Magnetic Field	± 0.5 T	1 mT	≤ 5 kHz

Table D.2: Sensor design requirements.

dSPACE RTI is $f_s = 10$ kHz, therefore the signal bandwidth of all sensors can be max $f_{-3dB} = 5$ kHz.

Magnetic Field Sensor Fixture

For measuring the magnetic field in the air-gap, a combination between 2 sensing principles is proposed. A hall sensor for measuring the constant field values and a sense coil to measure the changes in the magnetic field. The signals can be combined using a method like the hybrid flux estimator proposed by [35].

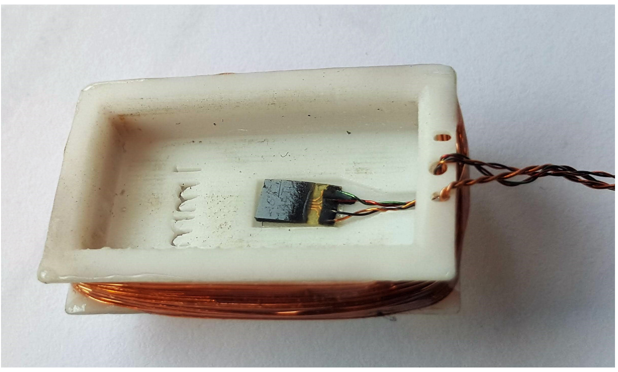

Figure D.9: Sensor fixture with hall sensor and sense coil.

Figure D.10: Sensor fixture placed over pole face.

The sensors are placed in a 3D printed fixture as shown in Fig.D.9. The fixture is used to house the sensors but also to fix the nominal air-gap width. It can be placed over the actuator pole face such that the plastic in which the hall sensor is embedded fills the air-gap (Fig. D.10. This layer is printed with an accurate thickness of 1.00 mm.

E

Measurement Setup Specifications

This chapter provides specifications and datasheets for the different parts that make up the measurement setup, as well as an evaluation of each component.

E.1. Setup Overview

Figure E.1 shows an overview of the measurement setup containing the AlNiCo 5 and AlNiCo 6 TMs, the sensors and signal conditioning board. The coil is driven by a custom-designed linear power amplifier or an H-bridge. The setup is connected to a dSPACE Real-Time Interface to record the measured signals and implement the magnetization state tuning for the TMs.

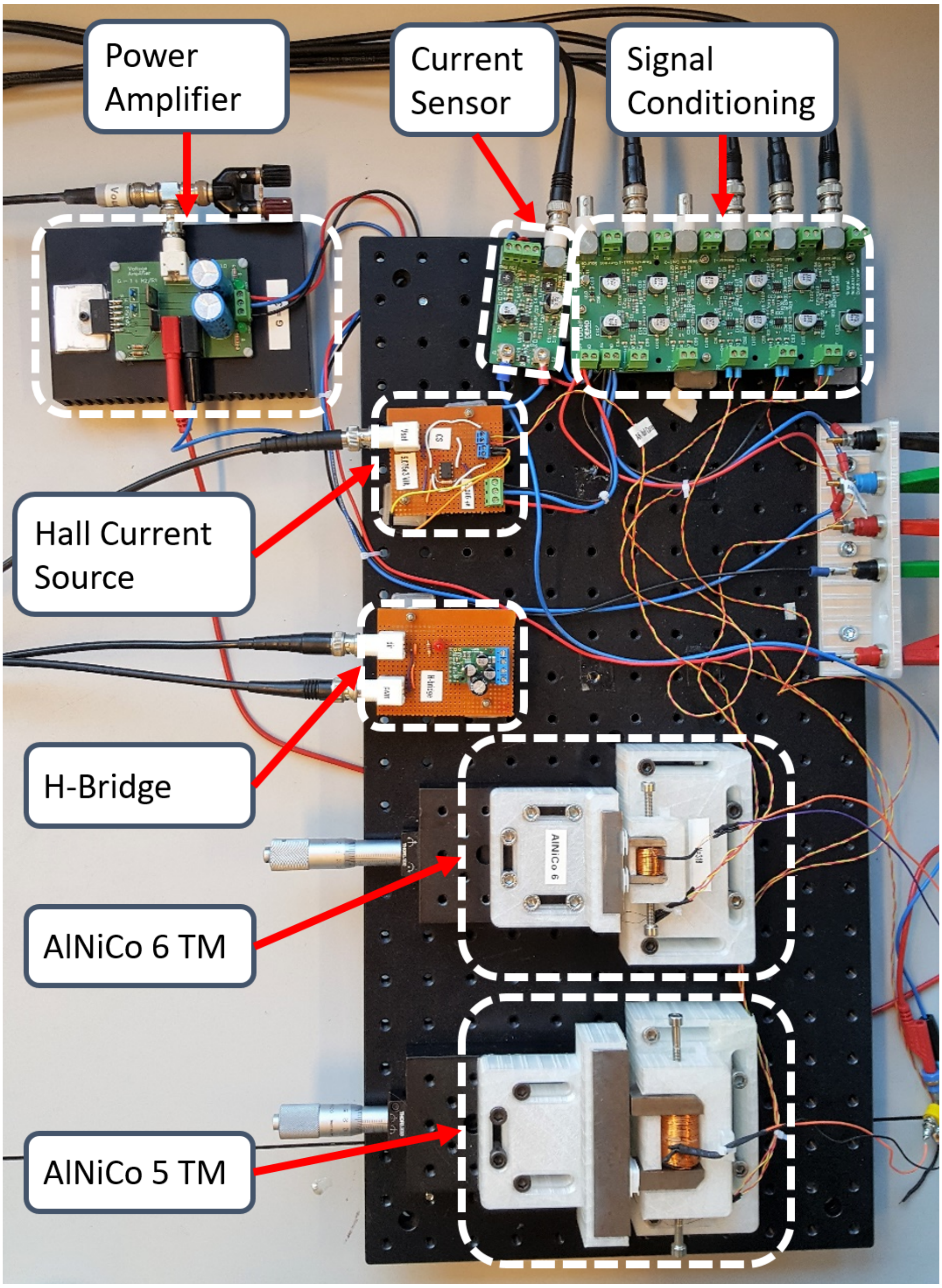

Figure E.1: Overview of the TM measurement setup.

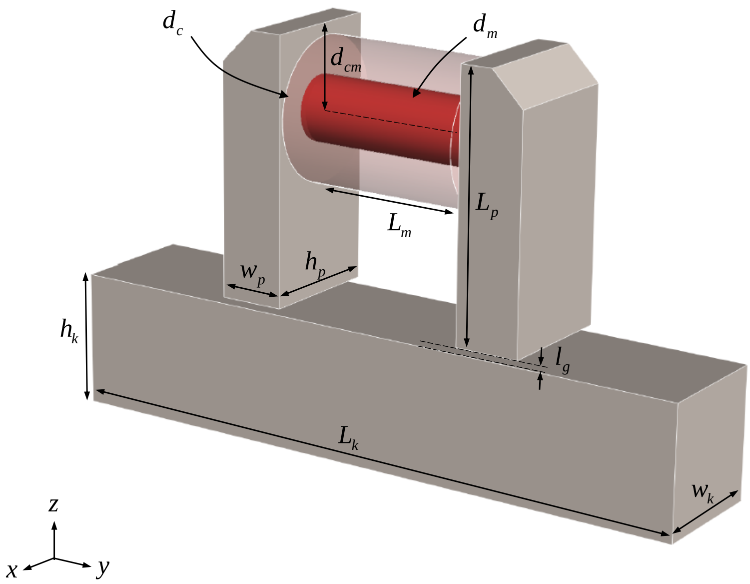

Figure E.2: TM actuator with AlNiCo magnet and magnetizing coil.

E.2. Tunable Magnets

Figure E.2 shows a CAD model of the TM actuator with annotated parameters. The values of these parameters can be found in Tab. E.1 and E.2 for the AlNiCo 5 and AlNiCo 6 TMs respectively.

AlNiCo 5 Test Setup Parameters			
Parameter	Value	Comment	Source
AlNiCo 5 Magnet		Other names: LNG44, Alcomax 3	Appendix I
L_m	30.2 mm	Magnet length	
d_m	9.83 mm	Magnet diameter	
B_r	1.25 T	Remanent flux density	Appendix I
H_c	50 kA m^{-1}	Coercive force	Appendix I
H_s	150 kA m^{-1}	Saturation field intensity	$3 \times H_c$ [8]
$\mu_{r,max}$	270	Maximum permeability	[7]
Magnetization Coil			
L_c	28.2 mm	Coil length	
d_c	21.5 mm	Coil outer diameter	
d_w	0.45 mm	Copper wire diameter	
N	668	Number of coil windings	
ρ_c	2.09×10^{-9} Ω m	Copper wire resistance	
St.37 Magnetic Circuit			
L_p	39.9 mm	Pole piece length	
w_p	10.0 mm	Pole piece width	
h_p	20.0 mm	Pole piece height	
L_k	100 mm	mover length	
w_k	20.0 mm	mover width	
h_k	20.0 mm	mover height	
$\mu_{r,avg}$	1000	Average relative permeability	Appendix I
Setup			
l_g	1.00 mm	nominal air-gap width	
d_{cm}	12.3 mm	magnet position w.r.t. pole piece	

Table E.1: Test setup parameter values for the AlNiCo 5 TM.

AlNiCo 6 Test Setup Parameters			
Parameter	Value	Comment	Source
AlNiCo 6 Magnet		Other names: LNG28, Alcomax 4	Appendix I
L_m	16.0 mm	Magnet length	
d_m	4.74 mm	Magnet diameter	
B_r	1.15 T	Remanent flux density	Appendix I
H_c	58 kA m^{-1}	Coercive force	Appendix I
H_s	174 kA m^{-1}	Saturation field intensity	$3 \times H_c$ [8]
Magnetization Coil			
L_c	14.6 mm	Coil length	
d_c	16.7 mm	Coil outer diameter	
d_w	0.45 mm	Copper wire diameter	
ρ_c	2.09×10^{-9} Ω m	Copper wire resistance	
N	318	Number of coil windings	
St.37 Magnetic Circuit			
L_p	23.7 mm	Pole piece length	
w_p	11.9 mm	Pole piece width	
h_p	4.7 mm	Pole piece height	
L_k	56.1 mm	mover length	
w_k	11.9 mm	mover width	
h_k	11.9 mm	mover height	
$\mu_{r,avg}$	1000	Average relative permeability	Appendix I
Setup			
l_g	1.00 mm	nominal air-gap width	
d_{cm}	7.8 mm	magnet position w.r.t. pole piece	

Table E.2: Test setup parameter values for the AlNiCo 6 TM.

E.3. dSPACE RTI

A dSPACE RTI (Fig. E.3) is used to record sensor signals and and implement the magnetization state tuning method proposed in this thesis. The system consists of DS1005 Power PC combined with a DS2004 A/D and DS2102 D/A board (Tab. E.3).

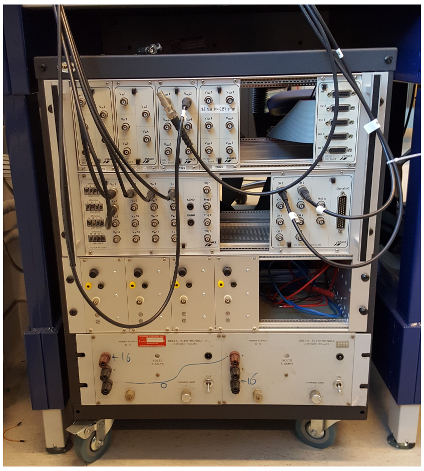

Figure E.3: dSPACE RTI unit.

Hardware	I/O range	Resolution	Sampling
DS1005 PPC Board			10 kHz
DS2004 A/D Board	±10 V	16-bit	10 kHz
DS2102 D/A Board	±10 V	16-bit	10 kHz

Table E.3: dSPACE hardware properties

Evaluation: The sampling rate of the dSPACE RTI has been tested up to 10 kHz, running the magnetization state tuning method proposed in this thesis. Higher sampling rates are probably possible but limited by the complexity of the program that needs to run real-time.

E.4. Current Sensor

The current sensor was custom designed by the electronic and mechanical support division of the University (DEMO). It combines a large range with a high resolution. This is achieved by accurately amplifying the voltage drop over a small value sense resistor to determine the current. To prevent aliasing, the sensor contains an integrated low-pass filter, limiting the bandwidth of the output signal. It can be used to measure currents through a load directly inside an H-bridge, because of its ability to handle large common-mode voltages. See the schematics (Fig. E.5) for more details.

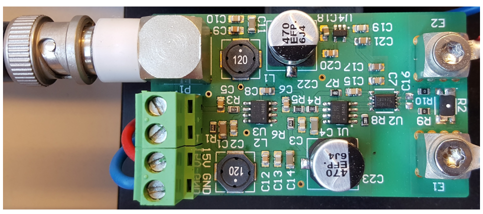

Figure E.4: Current Sensor

Parameters	Value	Comment
Range	±10 A	
Sensitivity	$2\,\mathrm{A\,V^{-1}}$	
Resolution	≈ 5 mA	ΔI_{pp}
Bandwidth	3 kHz	integrated LPF
Input voltage	15 V	Max

Table E.4: Current Sensor properties

Evaluation: The instrumentation OpAmp that amplifies the voltage over the sense resistor is very sensitive. Running a current through the circuit containing the coil and the sensor and suddenly disconnecting the leads can cause a voltage spike over the sense resistor that burns out the amplifier chip. Therefore **only interrupt the coil circuit when there is no current running**.

Current Sensor Schematics

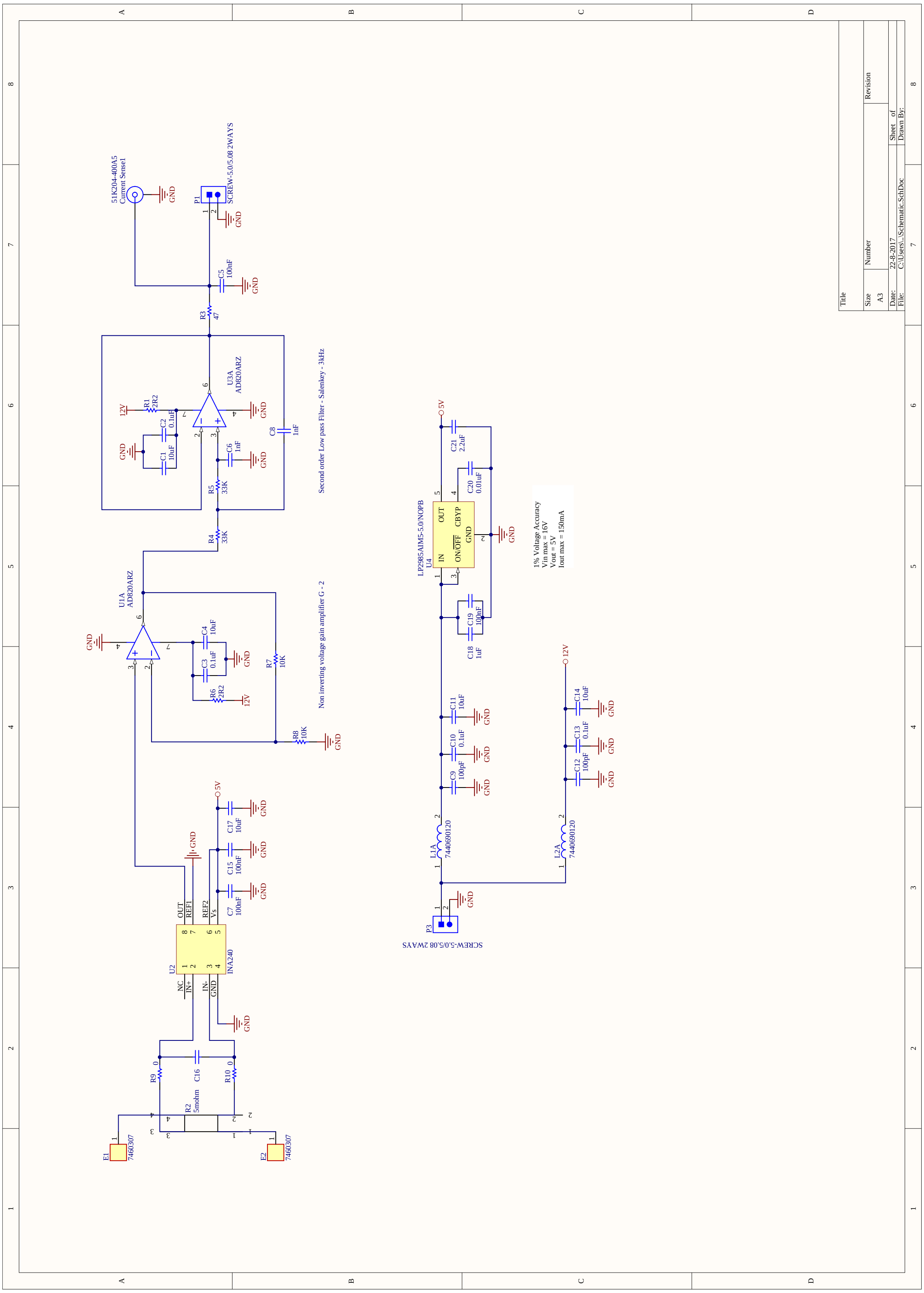

Figure E.5: Current Sensor Schematics, designed by DEMO

E.5. Magnetic Field Sensor Fixture

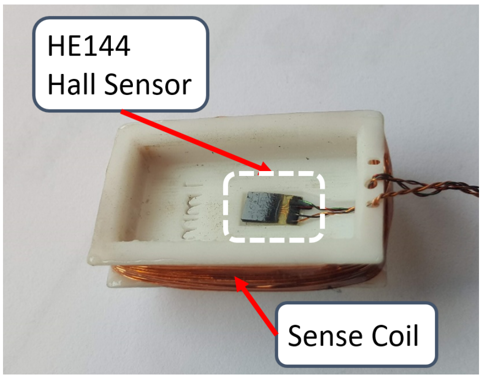

Figure E.6: Sensor fixture with hall sensor and sense coil

Parameters	Value	Comment
Hall Sensor		
Range	± 1.5 A	Calibrated range
Sensitivity	5.131 T/V	Measured sensitivity
Resolution	sub mT	Datasheet (Fig. E.8)
Bandwidth	100 kHz	Communication with supplier
Sense Coil (AlNiCo 5 TM)		
Sensitivity	$\frac{1}{N_s A_g}$ T/s/V	$N = 50$, $A_g = 2 \times 10^{-4}$ m^2

Table E.5: Magnetic field sensor properties.

Figure E.6 shows the sensor fixture with the hall sensor inside and the sense-coil around it. It is 3D printed such that it fits over the TM pole face. The part in which the hall sensor is embedded is precisely 1.00 mm, to fix the nominal air-gap width.

The hall sensor is a HE144 sensor from [2], and the datasheet is shown in Fig. E.8. To calibrate the hall sensor, we used the highly stable and homogeneous magnetic field of a vibrating sample magnetometer (VSM). The hall sensor was placed exactly parallel with the pole face of the VSM and the hall voltage recorder for several magnetic field values. The sensor was calibrated using a hall current of 1.00 mA. Figure E.7 shows the resulting calibration curve. It shows that the sensor has excellent linear behavior.

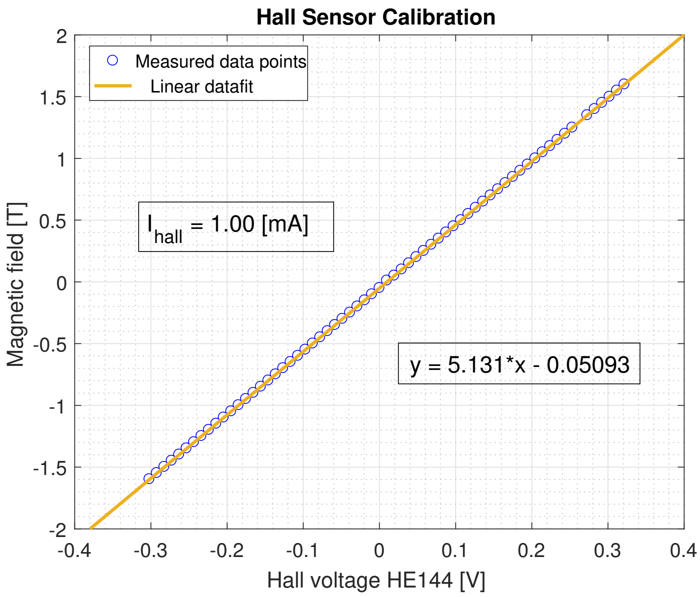

Figure E.7: HE144 hall sensor calibration curve.

Evaluation: In this research, only the hall sensor was used to measure the magnetic flux density in the air-gap, because the lack of time to implement the hybrid flux sensing scheme [35] and because the hall sensor measurement provides enough bandwidth.

Datasheet HE144

HE144

Advanced Sensor Technology

Linear High Precision

Analog Hall Sensor HE144

Features

- Large magnetic field range - below milli-Tesla to over 10 Tesla
- Very small linearity error - typically 0,1 % up to 1,5 T
- Optimized for low Hall sensor current - typical 1000 Ohm and 0,2 Volt/Tesla at 1 mA
- Very high sensitivity
- Low noise
- Low drift
- Low inductive zero component, low EMC pickup
- Low temperature coefficients
- Very wide operating temperature range
- Very low PHE, Planar Hall Effect Error
- Very flat miniature package
- Pin compatible with Siemens®/Infineon® KSY14 and KSY44

Deviation from linearity at 1mA, 20 °C
Comparison with Infineon KSY44

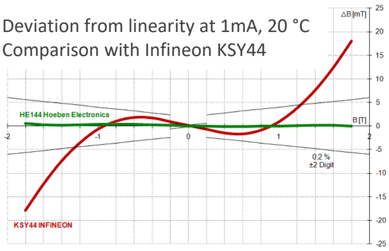

Our products are lead free devices, compliant with RoHS, REACH and 'Japan green' demands.

Typical applications

- Magnetic field measurements
- Oil drill measurement
- Position and rotation sensing
- Distance and thickness measurements
- Aerospace
- Current and power measurement
- Multi-sensor and differential usage
- Control of motor flux strength
- Windmills
- Movement sensing

Asensor Technology AB
Maskinvägen 6
746 30 Bålsta
Sweden

When Performance Matters

E-mail: hallsensor@asensor.eu
Phone: +46 8 590 755 10
Phone (NL): +31 6 515 900 81
www.asensor.eu

Specifications HE144

Electrical specifications		Values
Advised supply current		0,1 to 2,0 mA recommended 1 mA*
Open-circuit Hall voltage B=1 T		typical 200 mV at I=1 mA min 180 to max 360
Temperature coefficient of open-circuit Hall voltage B=1 T, at 25°C		typical -0,015 %/K at I=1 mA min -0,02 to max 0,02
Ohmic offset voltage B=0 T		≤± 12 mV at I=1 mA typical 10 mV **
Temperature coefficient of ohmic offset voltage B=0 T		typical 40 ppm/K (6,7 µT/K) at I=1 mA
Linearity of Hall voltage at I=1 mA	B = ± 0 to 1 T	≤± 0,2 % typical ≤± 0,1 %
	B = ± 1 to 2,4 T	Limit not specified typical ≤± 0,2 %
Supply side internal resistance B=0 T		900 to 1250 Ω typical 1000 Ω
Hall side internal resistance B=0 T		900 to 1700 Ω typical 1000 Ω
Thermal conductivity in air		≥ 1,5 mW/K
Thermal conductivity soldered		≥ 2,2 mW/K
Bandwidth		Not specified (contact us)

* Optimal signal to noise ratio and low power consumption
** Variations within the same production batch are very small.

Absolute maximum ratings		Values
Supply current		10 mA
Operating temperature	**P-version**	-40 to +170 °C
	SH-version	-40 to +125 °C
	T-version	-40 to +125 °C
	HT-version	-40 to +200 °C

For very low (cryogenic down to a few Kelvin) or very high (over 200 °C) temperature applications, contact us for more information.

Figure E.8: HE144 hall sensor datasheet, from [2].

E.6. Signal Conditioning

The signal conditioning PCB provides four differential input channels for sensor signal amplification and filtering. Two differential channels are for the HE144 hall sensors and the other two for the sense coils, both having the appropriate gains. To provide current for the hall sensors, the board has a regulator that provides a stable $1\,\mathrm{mA}$ current. Since the magnetizing coil can become hot, the board also has a connection for a temperature sensor to watch the coil temperature. The sensor should be a temperature dependent resistor since it is connected in a voltage divider on the PCB.

Figure E.9 shows the finished PCB and Fig. E.10 the associated schematics. The PCB can handle an input voltage up to $\pm 15\,\mathrm{V}$.

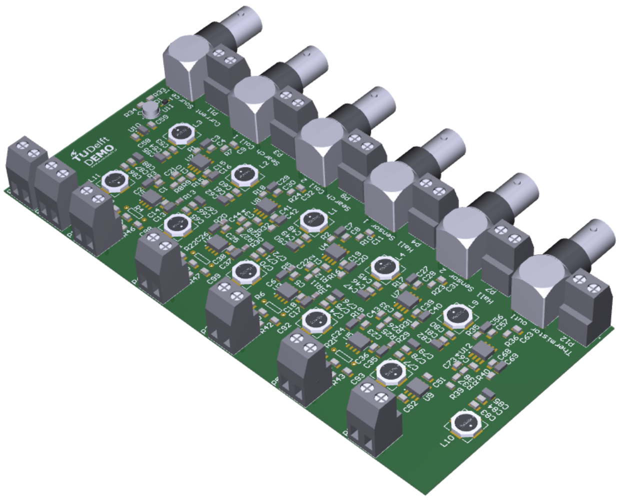

Figure E.9: Signal Conditioning PCB.

Channel	Input	Gain	LPF	Noise (ΔV_{pp})	Comments
Sense Coil 1	Differential	1.01	$3\,\mathrm{kHz}$	$\approx 1\,\mathrm{mV}$	Gain at $100\,\mathrm{Hz}$
Sense Coil 2	Differential	0.99	$3\,\mathrm{kHz}$	$\approx 1\,\mathrm{mV}$	Gain at $100\,\mathrm{Hz}$
Hall 1	Differential	23.85	$3\,\mathrm{kHz}$	$\approx 1\,\mathrm{mV}$	Gain at $100\,\mathrm{Hz}$
Hall 2	Differential	23.85	$3\,\mathrm{kHz}$	$\approx 1\,\mathrm{mV}$	Gain at $100\,\mathrm{Hz}$
Temperature	Half bridge resistor	n/p	$3\,\mathrm{kHz}$	n/p	in-situ bridge resistor is $33\,\mathrm{k\Omega}$
Current source	n/a	n/a	n/a	n/a	stable $1\,\mathrm{mA}$ current source

Table E.6: Specifications of the channels on the signal conditioning board. Board power supply is max $\pm 15\,\mathrm{V}$.

Evaluation: The board works fine except for the hall current source. It is not able to provide a $1\,\mathrm{mA}$ hall current through the sensor's internal resistance of $\approx 1\,\mathrm{k\Omega}$. This can be solved by replacing the current regulator chip on the PCB.

Signal Conditioning Schematics

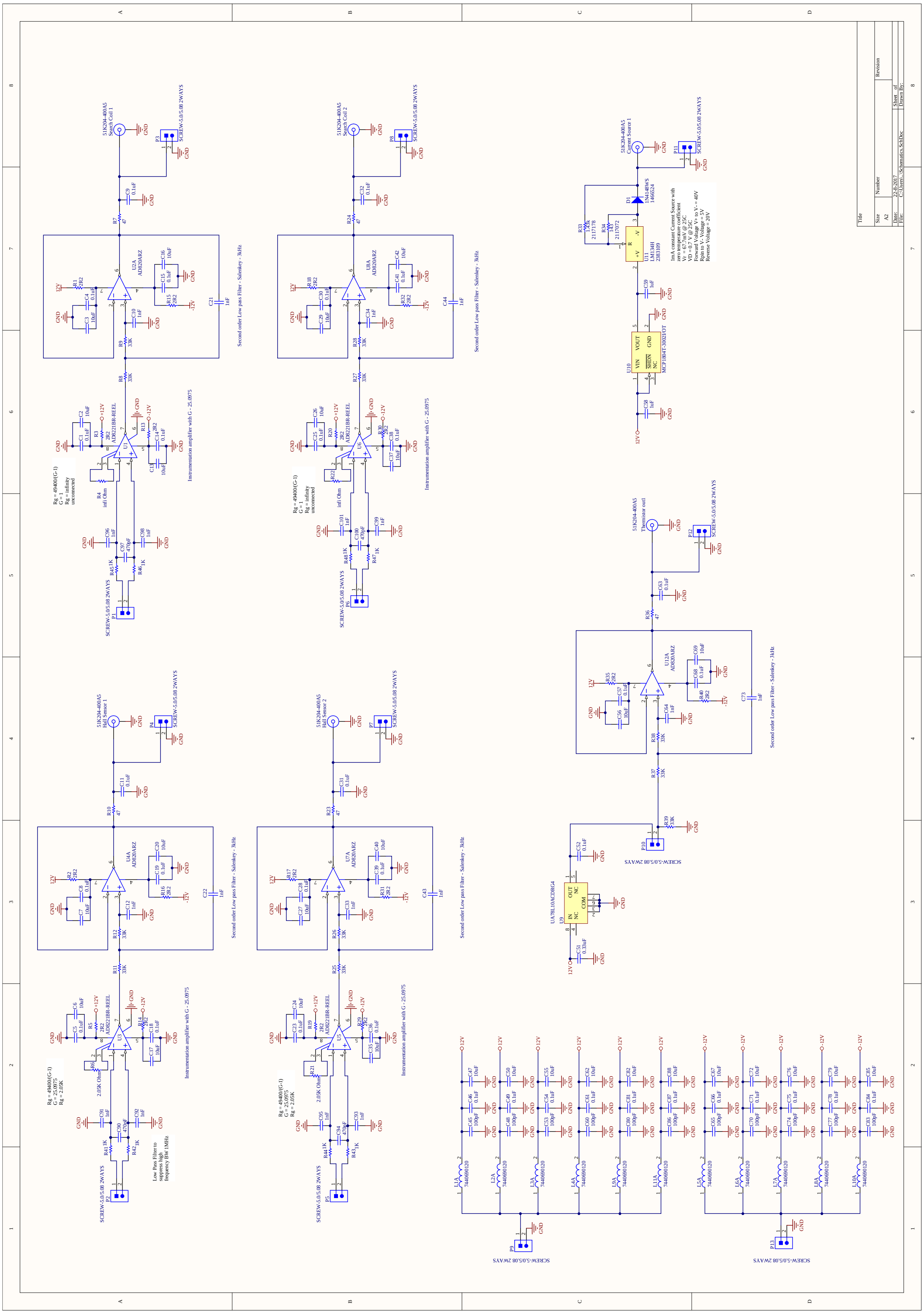

Figure E.10: Signal conditioning board schematics, designed by DEMO.

E.7. Linear Power Amplifier

The linear power amplifier consists of a TI OPA549 OpAmp in a non-inverting amplifier configuration. It can deliver 8 A continuous and 10 A peak current at an approximate output voltage of ± 25 V, slightly lower than the supply voltage. The actually available voltage swing depends on how much current is being supplied.

Figure E.13 shows the schematics of the amplifier PCB, adapted from the example implementation in the datasheet [54]. The diodes at the output protect the OpAmp from potential voltage spikes associated with driving inductive loads. The capacitors are used to stabilize the power supply. The PCB layout is shown in Fig. E.12. It shows the ceramic capacitors as close to the chip as possible and the large electrolytic ones close to the screw terminals connecting the PCB to the external voltage source. High current paths in the PCB are made as wide as possible to prevent heating.

Fig. E.11 shows the assembled amplifier PCB, mounted on a heat sink.

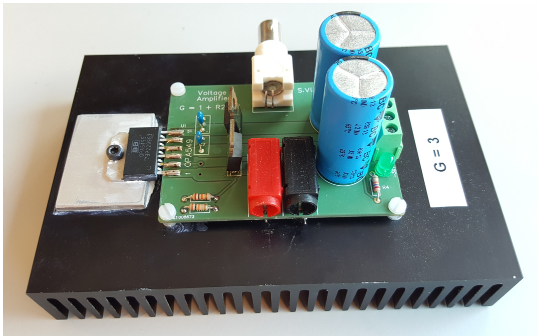

Figure E.11: Linear Power Amplifier

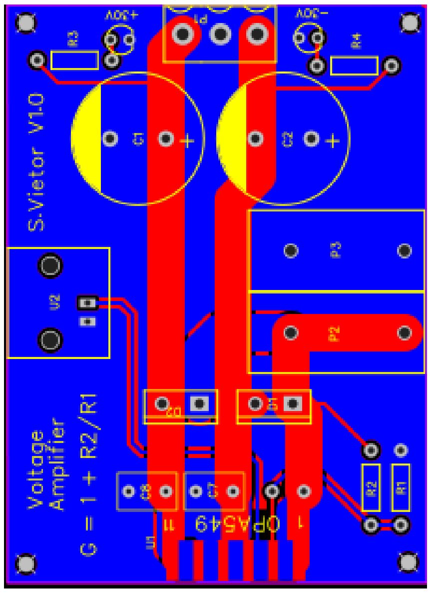

Figure E.12: Amplifier PCB Layout. Blue is the bottom layer and red the top layer.

Parameters	Value	Comment
Output current	± 8 A	Continuous
Output voltage	± 25 V	Approx.
Supply voltage	± 30 V	Max.
Amplifier Gain	3	

Table E.7: Amplifier properties

Evaluation: The linear power amplifier functions as expected. However, it becomes very hot after minutes of continuous operating, even with the heat-sink. The OPA549 has internal over-temperature protection that limits the output once the chip becomes too hot, but this affects the output signal. A larger heat sink solves this problem.

Also, the signal input of the amplifier is not tied to ground via a pull-down resistor. Therefore, if the input cable is not connected, the amplifier will start to float and output all kinds of non-zero voltages. This can be solved by connecting an external pull-down resistor or always leave the input cable connected when powered on.

Linear Power Amplifier Schematics

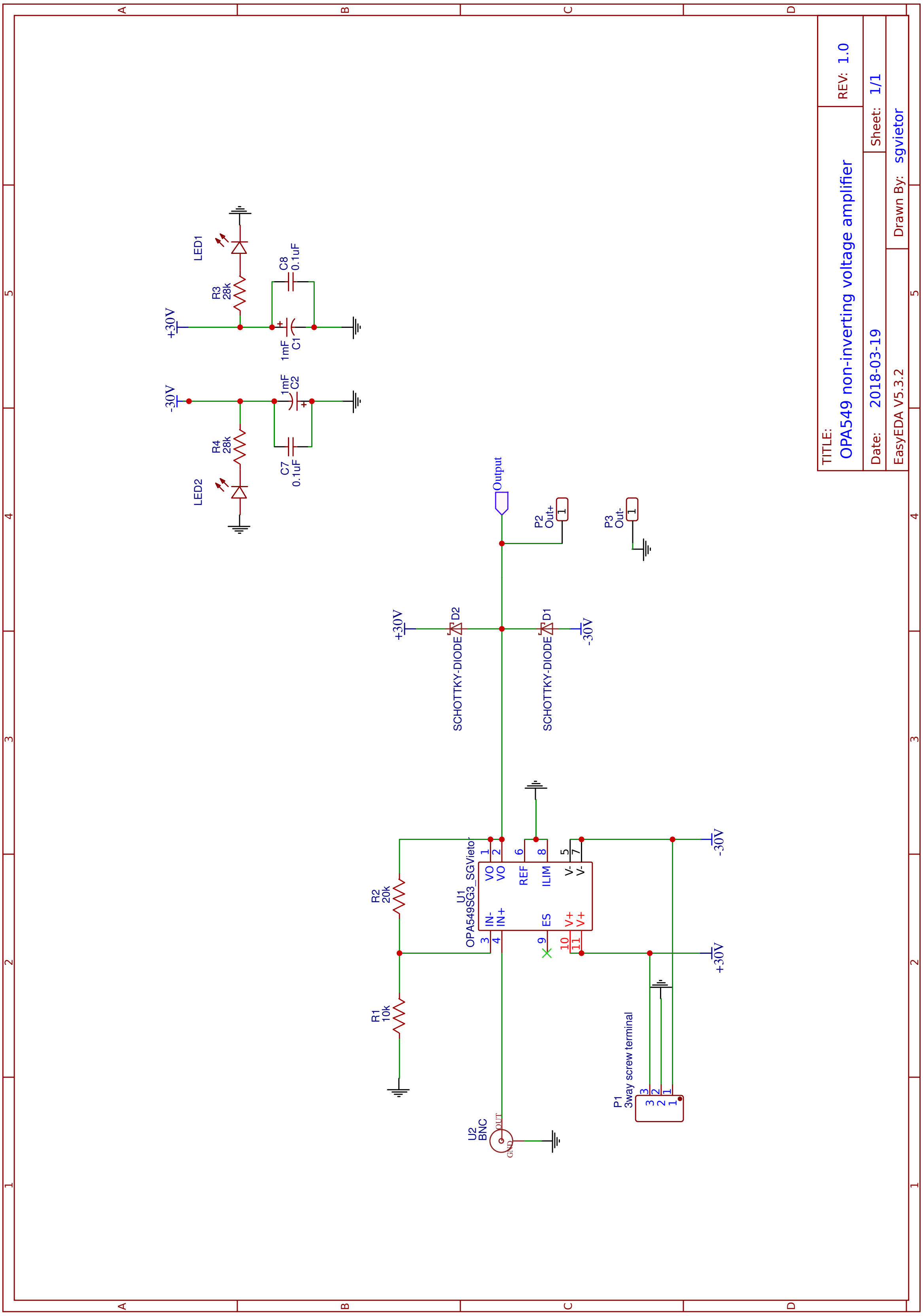

Figure E.13: OPA549 power amplifier schematics.

E.8. H-bridge

The measurement setup also contains an H-bridge to drive the magnetizing coils.

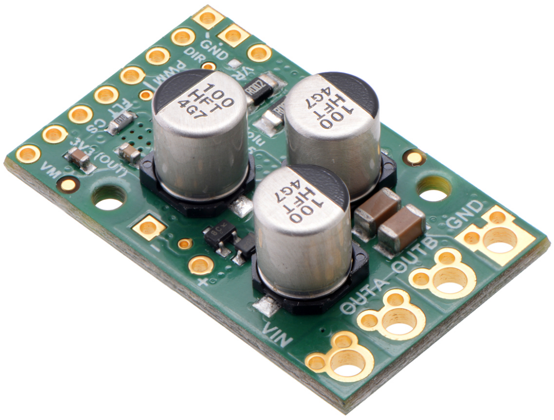

Figure E.14: H-bridge from [50].

Parameters	Value	Comment
Output current	$\pm 21\,\mathrm{A}$	Continuous
Output voltage	$\pm 40\,\mathrm{V}$	
PWM frequency	$\leq 100\,\mathrm{kHz}$	

Table E.8: H-bridge properties.

Evaluation: As calculated in Sec. D.2, the H-bridge has a large current ripple that makes it not suitable for precise magnetization state tuning.

F

Modeling Hysteresis

In this chapter, we describe the theory, derivation, and implementation of the hysteresis model used to simulate the ferromagnetic hysteresis behavior of AlNiCo.

In general, there are two types of hysteresis models: phenomenological models and physical models. Physical models are based on the physical principles underlying the hysteresis phenomena they describe. The most widely used physical model to describe ferromagnetic hysteresis is the Jiles-Atherton model [22]. This is also the model implemented in COMSOL for simulating the hysteresis behavior of ferromagnetic materials. Phenomenological models, on the other hand, are mathematical functions and relations that attempt to model hysteresis behavior without regard to the physical functioning of the material or process they describe. One of the most widely used phenomenological models is the Preisach Model [39], first developed by F. Preisach in 1935 [51].

To model the ferromagnetic behavior of AlNiCo, we will use the relative simple Classical Scalar Preisach Model [35]. Though more elaborate variants exist, we are only interested in modeling general ferromagnetic behavior of AlNiCo to gain an understanding of how TMs behaves and to test magnetization state tuning methods. For this, the basic version of the Preisach model suffices.

F.1. Preisach Model Derivation

This section will give a derivation of the basic Preisach model, and discuss its most important properties. A more detailed analysis can be found in the sources frequently mentioned in this section [3, 21, 34]

Hysterons & The Preisach Plane

The basic building block of the Preisach model is the so called *Preisach Hysteron* shown in Fig. F.1. It is a mathematical relay of which the input-output relation is defined by [21]:

$$v(t) = \gamma_{\alpha,\beta}(u(t)) = \begin{cases} -1 & \text{if } u(t) \leq \beta \\ 1 & \text{if } u(t) \geq \alpha \\ v(t-1) & \text{if } \beta < u(t) < \alpha \end{cases} \tag{F.1}$$

Where $\gamma_{\alpha,\beta}$ is the hysteron defined by thresholds α and β, with $\alpha \geq \beta$. If the input $u(t)$ at time t is greater then α or smaller then β, the output $v(t)$ will be 1 or -1 respectively. When $u(t)$ lies within range (β, α), the output $v(t)$ remains unchanged and is equal to the previous output $v(t-1)$.

The Preisach hysteresis model, also called Preisach Operator, is a weighted sum of an infinite amount of *hysterons* as shown in figure F.2. In that sense, it can be seen as a mathematical approximation of the magnetic domains that are the basis of hysteresis behavior in a ferromagnetic material [3].

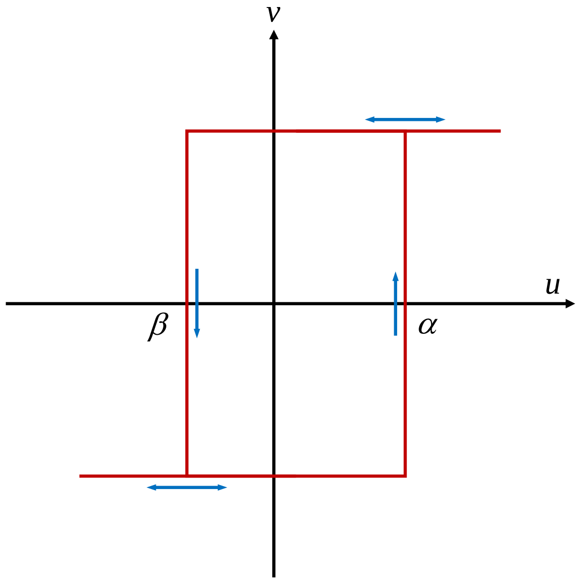

Figure F.1: *Preisach Hysteron*. Basic mathematical relay characterized by the thresholds α and β. The output v(t) is +1 if the input is larger then α and -1 if it is smaller than β. When the input is in range (β, α) the output remains unchanged.

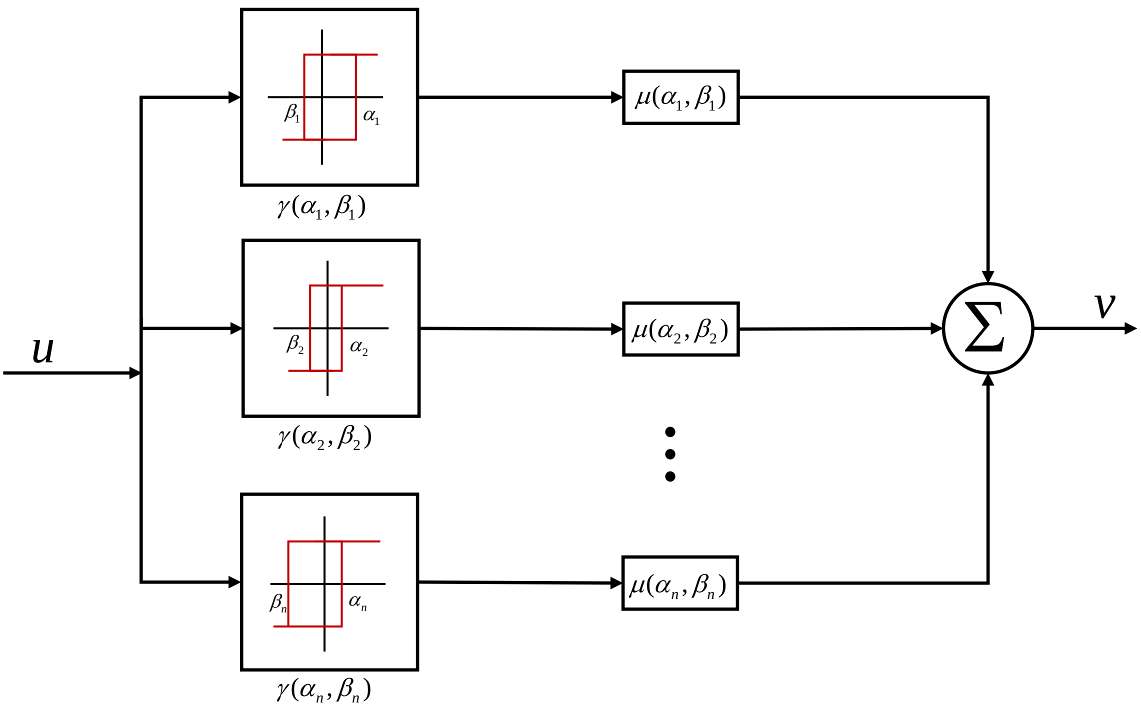

Figure F.2: Preisach hysteresis model described by a superposition of infinite hysterons, each weighted with Preisach density function $\mu(\alpha_n, \beta_n)$. The subscript n denotes that the thresholds belong to the n-th hysteron, with $n = 1 \ldots \infty$

This weighted summation of infinite Preisach hysterons can be described by the following integral [21]:

$$u(t) = \iint_{\alpha \geq \beta} \mu(\alpha,\beta)\gamma_{\beta,\alpha}\left(v(t)\right) d\beta d\alpha \tag{F.2}$$

where $\mu(\alpha,\beta)$ is known as the Preisach density function, which determines the weighting of the individual hysterons. Identifying a Preisach model means specifying and determining the density function.

The working of the Preisach operator is best understood graphically using the α,β plane, also known as the Preisach plane, shown in Figs. F.3, F.4 and F.5. The red triangle represents the integration domain of (F.2). It is bounded by $\alpha = \beta$, and the lines $\alpha = u_{max}$ and $\beta = u_{min}$, which represent the minimum an maximum possible input.

The triangle is split into two regions, marked P_{-} and P_{+}, where the output of the hysterons as determined by their thresholds (α,β) is -1 or 1 respectively. Outside the triangle, the value of the hysterons is undefined. The boundary between regions P_{-} and P_{+} is called the *Preisach Memory Curve* because it stores the relevant extrema of prior inputs to the Preisach operator. This can be best illustrated by an example.

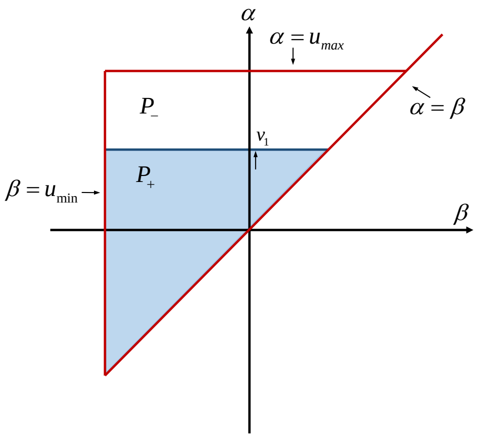

Figure F.3: Effect of an monotonic increase of input $v(t)$

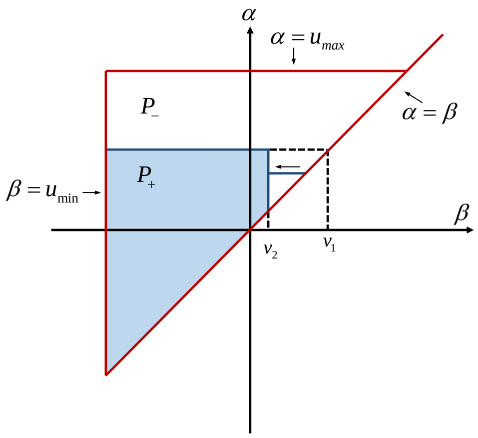

Figure F.4: Effect of a monotonic decrease of input $v(t)$

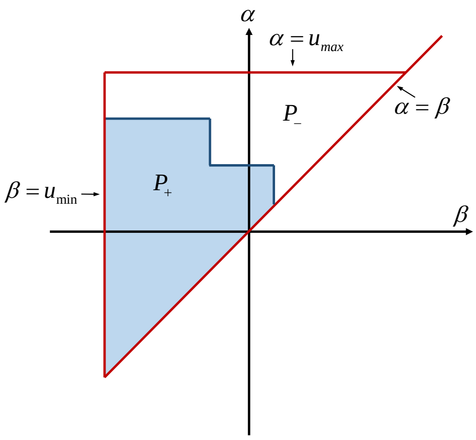

Figure F.5: Preisach plane with memory curve

Suppose that the input v(t) increases monotonically to v_1. This represents an upward shift of the horizontal boundary between P_{-} and P_{+}, as shown in Fig. F.3. The hysterons that have an upper threshold $\alpha \leq v_1$ will have switched their value to $+1$. Next, when the input monotonically decreases from v_1

to v_2, resulting in a leftward shift of the vertical boundary between P_- and P_+ as shown in Fig. F.4). The hysterons that have a lower threshold $\beta \geq v_2$ now switch their output to -1. This sequence of inputs creates a staircase shaped curve, as shown in Fig. F.5. This is called to Preisach memory curve because it stores the effect of previous inputs on the hysteresis operator. The corners of the staircase represent the dominant extrema of the input value in the past that define the current state of the Preisach operator.

Recognizing that the output of the individual Preisach hysterons is either 1 or minus 1, F.2 can be rewritten as [21]:

$$v(t) = \iint\limits_{P_+(t)} \mu(\beta,\alpha) d\beta d\alpha - \iint\limits_{P_-(t)} \mu(\beta,\alpha) d\beta d\alpha \tag{F.3}$$

This shows that the output of the Preisach operator is calculated by integrating the weighting function $\mu(\beta,\alpha)$ over the triangular Preisach plane. The value $v(t)$ of the output depends on the size of regions P_- and P_+, which in turn depends on the minima and maxima that are reached by past inputs.

F.2. Preisach Model Properties

Next, we will discuss some important properties of the Preisach operator.

Rate Independence

Rate independence means that the output is independent on how fast the input changes. Equation F.3 shows that the output of Preisach operator is determined only by the density function and the regions $P_-(t)$ and $P_+(t)$ on the Preisach plane. These regions are defined by the Preisach memory curve, which is only dependent on past inputs as shown in Fig. F.5. This means that the Preisach model is rate independent, so it does not model possible dynamic behavior between the input and the output.

Wiping-out Property

The output of the Preisach operator is defined by it current and past inputs. More specifically by the sequence of past reversal points, that is local minima and maxima reached by the succession of inputs. Even this is a redundant description [3]. The system state is completely defined by a set of monotonically decreasing input maxima, $u_{M_1} > u_{M_2} > ...u_{M_n}$ and a set of monotonically increasing input minima, $u_{m_1} < u_{m_2} < ...u_{m_n}$ reached in time in an alternating sequence, meaning $t_{m1} < t_{M1} < t_{m2} < t_{M2} < ...t_{mn} < t_{Mn}$. This is visualized in Fig. F.6.

Since the state is only defined by the set described above, the in-between extrema do not affect the outcome.

Figure F.7 shows a part of the input curve of F.6. The signal is first increased to u_1, then decreased to u_2 and then increases again. If it were to reach u_2 for the second time, the output will be the same as the case where the input would have increased further from the first time it reached u_1. In other words, the in-between oscillation does not have any effect on the subsequent behavior. This is called the wiping - out property since the memory of the in-between oscillation is wiped out. These oscillations in the input correspond to the traversal of a minor loop in the hysteresis graph, therefore this property is also called minor loop closure [21].

The wiping out property can also be visualized using the Preisach plane, were a large enough input can wipe out the entire staircase shaped memory curve, thereby removing the effect of past input minima and maxima.

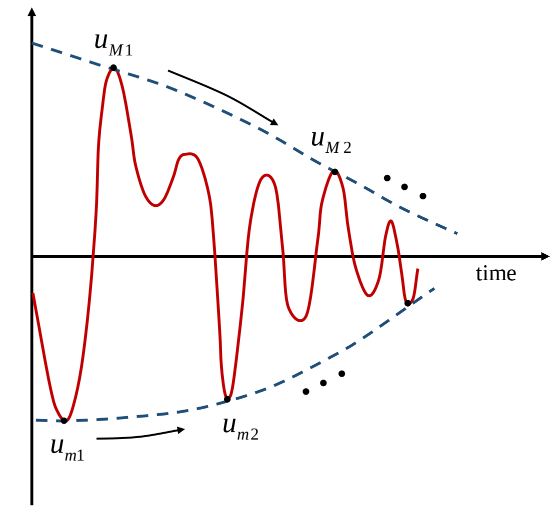

Figure F.6: Reversal point sequence that determines the state of the Preisach operator. Adapted from [3]

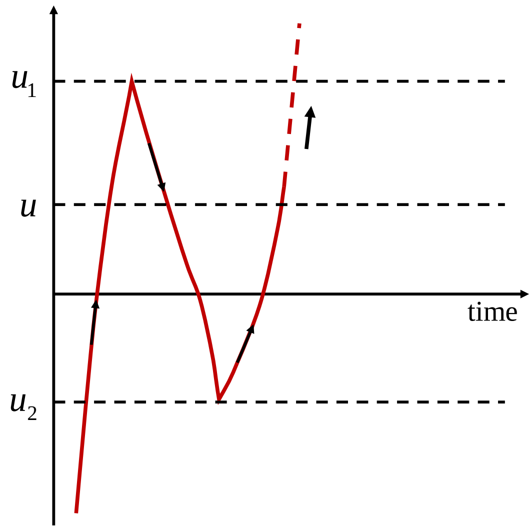

Figure F.7: Wiping-out property illustrated. Adapted from [3]

Applicability to AlNiCo Hysteresis Modeling

As mentioned in the introduction, the Preisach model is widely used in the modeling of ferromagnetic hysteresis, which is the effect that AlNiCo magnets exhibit. It can also simulate minor loops which makes it extra suitable for modeling TMs. Furthermore, the whole mathematical structure of the Preisach operator, being the superposition of hysterons with different switching levels, is similar to the behavior of magnetic domains found in ferromagnetic materials. However, the Preisach model has some limitations as to what behavior can be described. The most important limitation is that it can only describe rate-independent hysteresis. In reality, the rate of change of the applied magnetizing field affects the realized magnetization [3]. Therefore the Preisach operator is only valid for modeling quasi-static ferromagnetic hysteresis behavior.

F.3. Hui Implementation

A simple implementation of the Preisach model is proposed by Hui [18] and used in [34]. It is easy to implement since it only requires measurement data of the major hysteresis loop for identification.

This also means that, since no minor loop data is required, that its description of such loops is not very accurate. However, for the simulation of TM behavior, we are more interested in the general, qualitative behavior, for which this Preisach model implementation suffices.

Model Equations

The derivation of the Hui implementation, starting from the integral expression of the Preisach operator (F.3), can be found in detail in [18] and [35]. This section will only describe the resulting equations. The Hui implementation of the Preisach model describes the relation between the magnetic field intensity H and the resulting magnetic flux density B inside a ferromagnetic material as [18]:

$$B(H) = \begin{cases} B_n + 2T(H, H_n) & \text{for } dH > 0 \\ B_n - 2T(H_n, H) & \text{for } dH < 0 \end{cases} \tag{F.4}$$

Where dH is the direction of the input H and (B_n, H_n) the magnetization state at the last relevant reversal point as explained in Sec. F.2, where the general input u and output v are now replaced by H and B.

The function $T(H_1, H_2)$ is defined as:

$$T(H_1, H_2) = \frac{B_a(H_1) - B_d(H_2)}{2} + F(H_1)F(-H_2) \tag{F.5}$$

With $F(x)$ being:

$$F(H) = \begin{cases} \frac{B_d(H) - B_a(H)}{2\sqrt{B_a(H)}} & \text{for } H \geq 0 \\ \sqrt{B_d(-H)} & \text{for } H \leq 0 \end{cases} \tag{F.6}$$

Here, $B_a(H)$ and $B_d(H)$ denote the ascending and descending branches of the major hysteresis loop.

The initial magnetization curve is derived in [18] as:

$$B_i(H) = [F(-H) - F(H)]^2 \tag{F.7}$$

Simulation

Figure F.8 shows the flow diagram of the model routine. A stack is created to store the input history, containing the relevant reversal point sequence as described in Fig. F.6. If a reversal in the input signal is detected, this gets pushed into the stack. For every new value for input H that does not create a reversal point itself, the stack is checked if it contains any past reversal points that should be wiped out. Next, the last reversal point in the stack (H_n, B_n) is used to calculated the new value for B using (F.4), (F.5) and (F.6). If the stack is empty, that means there is no input history and magnet operates over its virgin curve (F.7).

Identification

The identification of the Hui implementation of the Preisach model is straightforward as mentioned earlier since it only needs the major loop data $B_a(H)$ and $B_d(H)$ to be specified. However, a few things need to be considered when identifying the model. Firstly, the major hysteresis loop needs to be symmetrical. This can be achieved by mirroring, for example, the measured ascending curve in both the H and B axis. Another option is to extend the model equations by using the asymmetric

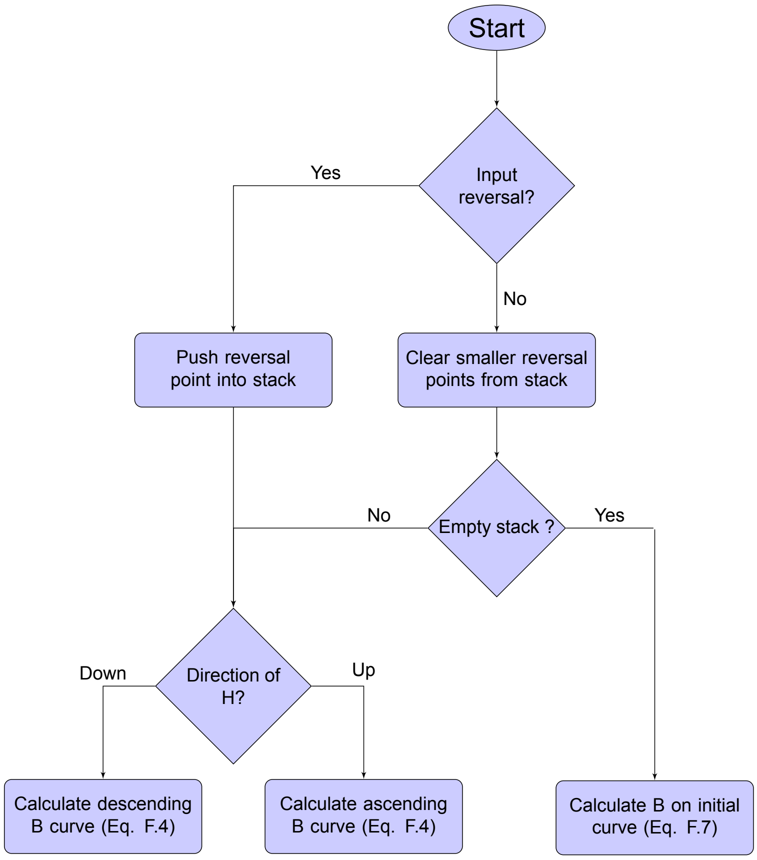

Figure F.8: Flow diagram of Preisach model implementation. Adapted from [19]

implementation described by [35]. Secondly, to create a smooth characteristic, we use a fitting function to fit the major loop measurement data. Simply using a look-up table that interpolates the measurement values for $B_a(H)$ and $B_d(H)$ works as well, but the quality of the output then depends on the how good the measurement data is.

The following function has been found to be a good fit for the ascending and descending branches of the AlNiCo 5 BH curve:

$$B(H) = a \cdot \arctan(b \cdot \mu_0 H + c) + d \cdot \mu_0 H \tag{F.8}$$

where a, b, c and d are the fitting coefficients.

Figure F.9 shows the ascending and descending hysteresis curves for AlNiCo 5 based on measurements by [7] and the curve fit using (F.8). The fitting coefficients for the ascending and descending curves are listed in Tab. F.1

	a	b	c	d
$B_a(H)$	-0.83	337.44	24.56	1.19
$B_d(H)$	-0.83	389.44	-28.20	1.08

Table F.1: Identified coefficients of (F.8) for the ascending and descending AlNiCo 5 major BH curves.

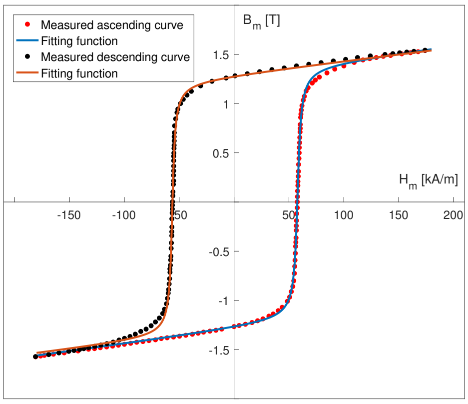

Figure F.9: Measured AlNiCo 5 ascending and descending hysteresis curves from [7], fitted with (F.8).

F.4. Results & Conclusion

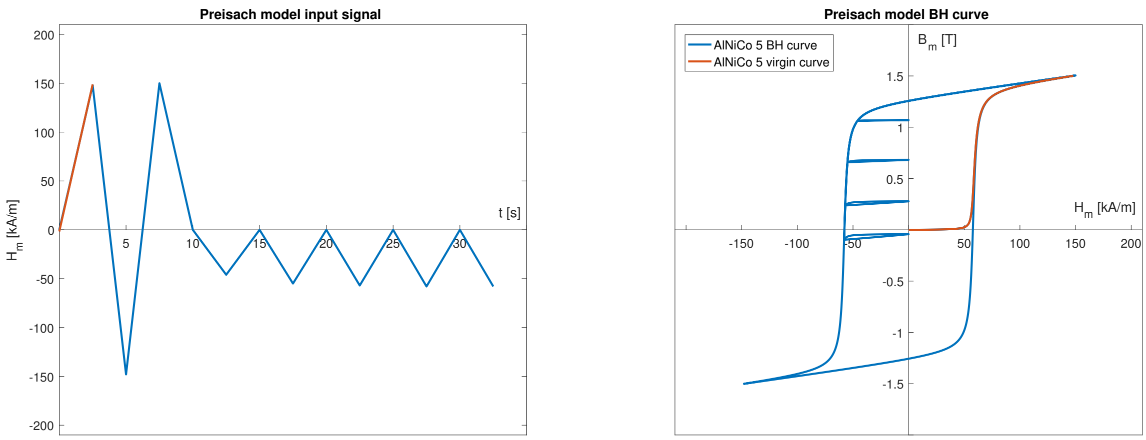

Figure F.10: AlNiCo 5 magnetization state trajectory (blue) for specified input signal. The model is initialized at zero magnetization, so it starts on the virgin BH curve (brown).

Figure F.10 shows the output of the identified Preisach model for a specified input signal. Note that the model is initialized at zero magnetization, so the BH output starts at the origin and follows the virgin curve to saturation. After that, the major BH curve is traced out as well as some recoil-lines. The recoil-lines are actually small loops, which is consistent with ferromagnetic material behavior. They are however different in shape depending on their position in the 2nd or third quadrant. This is most likely a shortcoming of the Preisach implementation used. Since no recoil-loop data is used to identify the Preisach density function, the simulation of these is not very accurate.

However, this Preisach model implementation is good enough to provide a general understanding of ferromagnetic hysteresis behavior of AlNiCo magnets. It can be incorporated in the TM model to test possible magnetization state tuning methods.

F.5. Matlab Code

The Hui implementation of the Preisach model can be implemented using Simulink, resulting in the block diagrams shown in Figs. F.11 and F.12. The code used for the various functions within the blocks is also listed in this section.

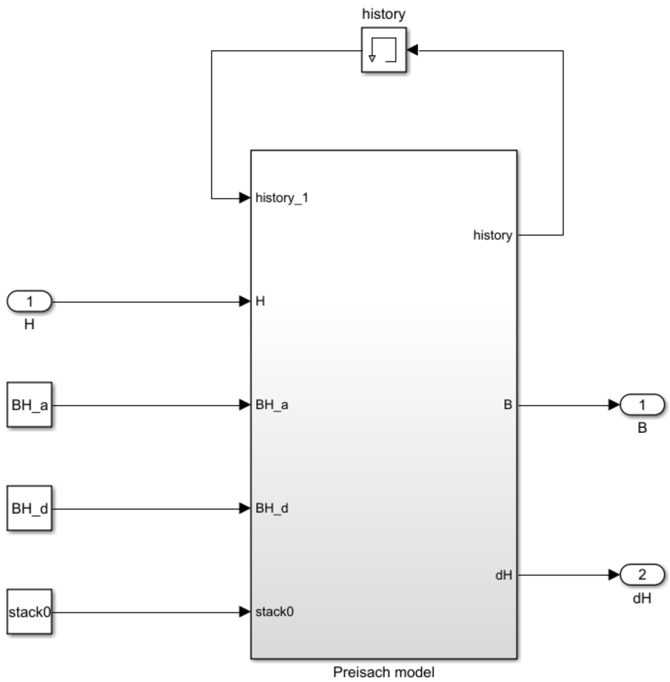

Figure F.11: Simulink implementation of the Preisach model (basic overview).

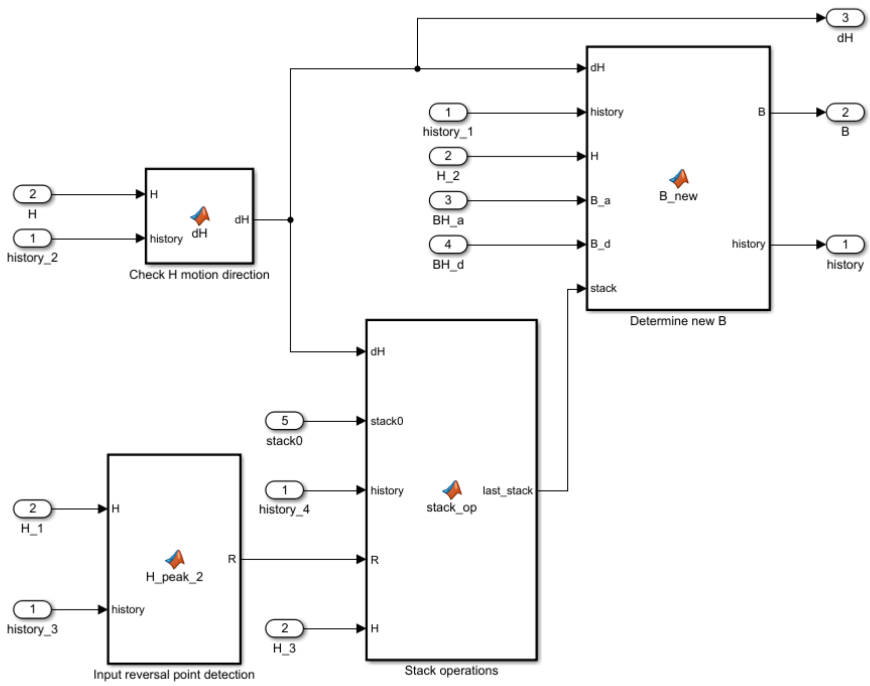

Figure F.12: Simulink implementation of the preisach model (details).

```matlab
%% Check H motion direction
function dH = dH(H,history)

H0 = history(1);

if H > H0
    dH = 1;
elseif H < H0
    dH = -1;
else
    dH = 0;
end
```

```matlab
%% Input Reversal-point Detection
function R  = H_peak_2(H,history)

persistent dir

H0 = history(1);

if isempty(dir) % initilize direction
    dir = history(2);
end

R = 0; % makes sure R is always defined

if dir == -1 % H decreasing during previous time step

    if H > H0 % reversal in direction, local minimum
        R = -1;
        dir = 1;
    end

elseif dir == 1 % H increasing during previous time step

    if H < H0 % reversal in direction, local maximum
        R = 1;
        dir = -1;
    end
end

end
```

```
%% Stack Operations
function last_stack = stack_op(dH,stack0,history,R,H)

H0 = history(1);
B0 = history(3);

persistent stack

if isempty(stack)
    stack = stack0;
end


if R % add reversal point (previous point) to the stack
    stack = [[H0 B0 R];stack(1:end-1,:)];

end

% Last nonzero stack entry
k = find(stack(:,3)==0,1)-1;


if k > = 2

    % check validity of the stack

    if stack(1,3) ≠ -stack(2,3)
        error('wrong extrema sequence')
    end


    if dH > 0

        LastMax = stack(2,1); % get last maximum from stack

        while H > = LastMax  % H higher then last local maximum

            stack(1:end-2,:) = stack(3:end,:); % remove minor loop ...
               from stack
            k = find(stack(:,3)==0,1)-1;

            if k > = 2
                LastMax = stack(2,1); % get next maximum from stack
            else
                break
            end
        end

    elseif dH < 0

        LastMin = stack(2,1); % get last minimum from stack

        while H < = LastMin % H lower then last local minimum

            stack(1:end-2,:) = stack(3:end,:); % remove minor loop ...
```

```
               from stack
           k = find(stack(:,3)==0,1)-1;

           if k > = 2
               LastMin = stack(2,1); % get next minimum from stack
           else
               break
           end
        end
    end

end

last_stack = stack(1,:);
```

```
%% Determine New B
function [B,history] = B_new(dH,history,H,B_a,B_d,stack)

H0 = history(1);
B0 = history(3);
dBdH_0 = history(4);

% Check validity of H
if H > max(B_a(:,1)) || H < min(B_a(:,1))
    error('Input H out of bounds of measured data')
end

% BH values of last reversal point
Hn = stack(1);
Bn = stack(2);

%% Update B
if not Hn && not Bn % virgin curve
    if dH == 1
        B = (F(-H,B_a,B_d)-F(H,B_a,B_d))^2;
    elseif dH == -1
        B = -(F(-H,B_a,B_d)-F(H,B_a,B_d))^2;
    else
        B = B0;
    end

elseif dH == 1 % ascending
    B = Bn + 2*T(H,Hn,B_a,B_d);

elseif dH ==-1 % descending
    B = Bn - 2*T(Hn,H,B_a,B_d);
else           % stationary
    B = B0;
end

% update history
history = [H dH B dBdHOut]';

end
```

```
%% T(H1,H2)
function [T] = T(H1,H2,B_a,B_d)
%T
T = 0.5*(interp1(B_a(:,1),B_a(:,2),H1,'linear','extrap')...
    -interp1(B_d(:,1),B_d(:,2),H2,'linear','extrap'))...
    + F(H1,B_a,B_d)*F(-H2,B_a,B_d);
end

%% F(H)
function [F] = F(x,B_a,B_d)
%F

if x> =0
    F = (interp1(B_d(:,1),B_d(:,2),x,'linear','extrap')...
    - interp1(B_a(:,1),B_a(:,2),x,'linear','extrap'))...
    /(2*sqrt(interp1(B_d(:,1),B_d(:,2),x,'linear','extrap')));
else
    F = sqrt(interp1(B_d(:,1),B_d(:,2),-x,'linear','extrap'));
end

end
```

G

Model identification

The behaviour of a Tunable Magnet, consisting of an AlNico PM combined with a magnetization coil, implemented in a reluctance actuator topology can be described by the following equations [57]:

$$B_m A_m = k_1 \, B_g A_g \tag{G.1}$$

$$H_m L_m + 2\, k_2 \, H_g l_g = N I_c \tag{G.2}$$

$$B_g = \mu_0 H_g \tag{G.3}$$

Determining the flux-leakage coefficient k_1 and MMF loss factor k_2 can be a tedious exercise however [8]. There exists a way to estimate the leakage flux analytically by predicting probable fringing and leakage flux paths. [52]. However, this leads to complicated and non-linear equations.

In this thesis we opted to identify k_1 and k_2 by using magnetic FEA in COMSOL. The analysis is first performed in 3D to be as accurate as possible. To determine how good these estimates represent the physical setup, a sensitivity study is performed in 2D. By varying different geometric and material values, we can determine the robustness of the estimate against manufacturing imperfections and uncertainty in parameters.

Next, the BH curve for AlNiCo is estimated by combining measurements performed with the experimental setup (App. D) with the identified model. Based on this, the value for k_1 is fine tuned such that remanence of the estimated BH curve better matches the value of the specific AlNiCo 5 used (see datasheet in appendix I.

G.1. Model Identification in COMSOL

Simulation Setup

For the simulation, the COMSOL physics package *Magnetic Fields no Currents* is used. The AlNiCo magnet is simply modeled as a material with specified remanence flux B_r along its axial direction. The B field is thus related to the H field by the following function:

$$B = \mu_r \mu_0 H + B_r \tag{G.4}$$

The relative permeability μ_r is assumed to be 1 (the case where the magnet is saturated). The model is identified at the nominal air-gap of $1\,\mathrm{mm}$. Figure E.2 shows the 3D model used in the simulation, with annotated geometrical parameters. Values for these parameters for the AlNiCo 5 TM actuator are listed in Tab. E.1.

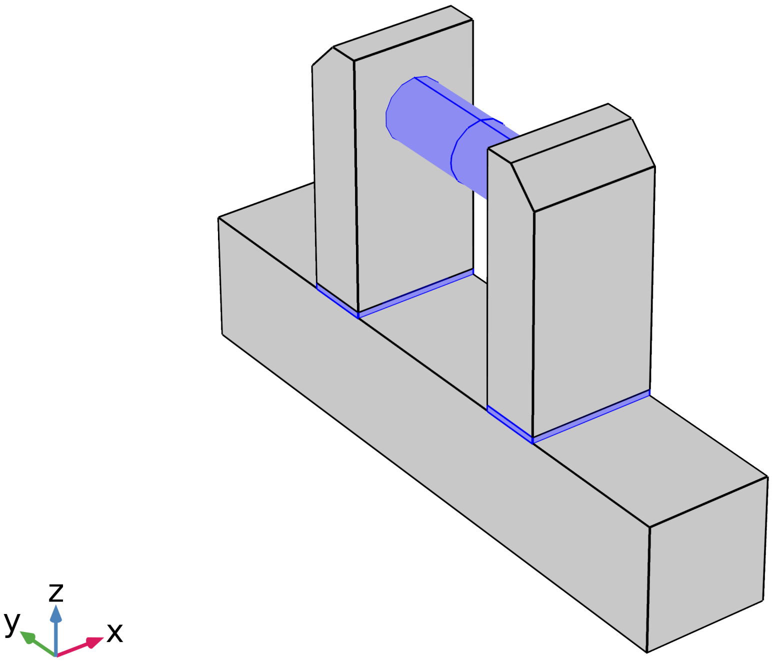

Figure G.1: 3D model with magnet and air-gap domains (marked in blue), used to evaluate flux and field values.

Results

To evaluate parameters k_1 and k_2, (G.1) and (G.2) are rewritten to:

$$k_1 = \frac{\phi_m}{\phi_g} \tag{G.5}$$

$$k_2 = \frac{H_m}{H_g}\frac{L_m}{2l_g} \tag{G.6}$$

where ϕ_m and ϕ_g are the fluxes in going through the magnet and the air-gap respectively. Values for these can be extracted from COMSOL by running the simulation and averaging the flux values over their respective domains, shown in blue in Fig. G.1. The same is done for the magnetic field intensities H_m and H_g.

Simulating the model yields a flux density distribution as shown in Fig. G.2. The average flux and field in intensity values and the resulting model coefficients are shown in Tab. G.1.

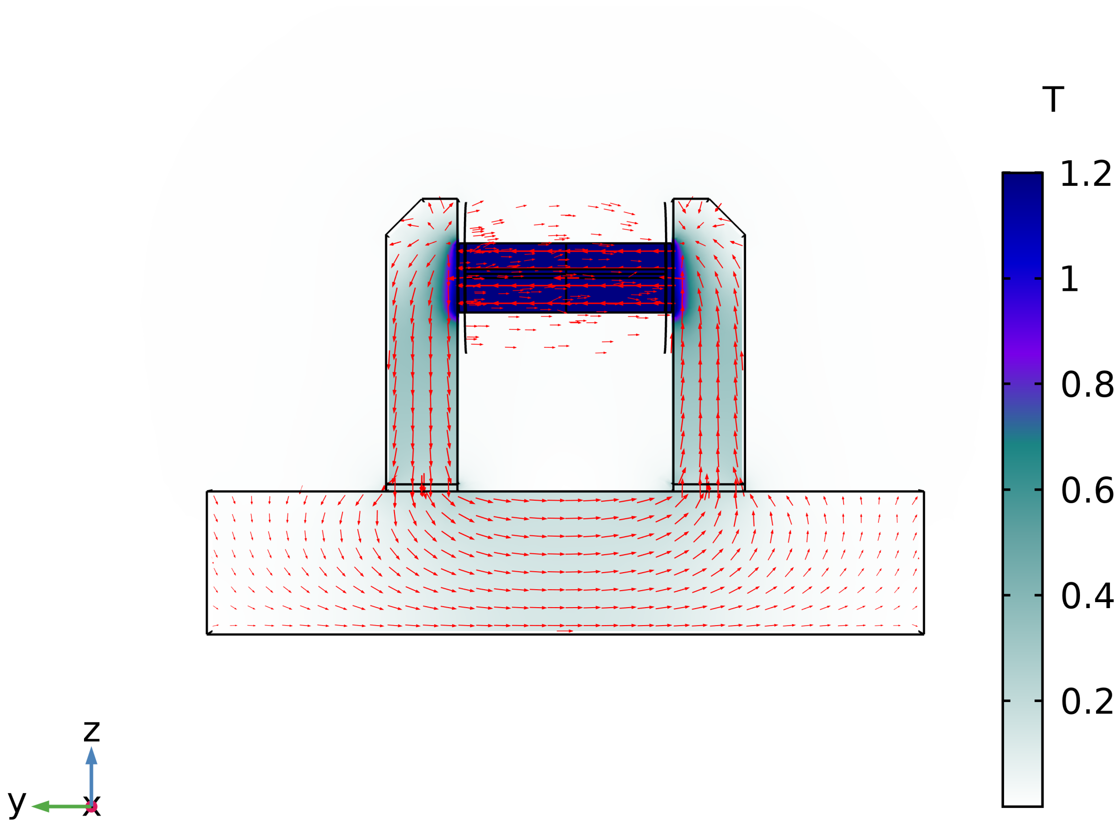

Figure G.2: Slice plot of the 3D model after simulation with flux density distribution (color scale) and direction (arrows).

Parameter	Value	Comment
$\phi_{m,avg}$	9.3909×10^{-5} Wb	Average magnet flux
$\phi_{g,avg}$	3.5004×10^{-5} Wb	Average air-gap flux
$H_{m,avg}$	10.086 kA m^{-1}	Average magnet field intensity
$H_{g,avg}$	140.18 kA m^{-1}	Average air-gap field intensity
k_1	2.68	Flux leakage coefficient
k_2	1.09	MMF loss factor

Table G.1: COMSOL identification results.

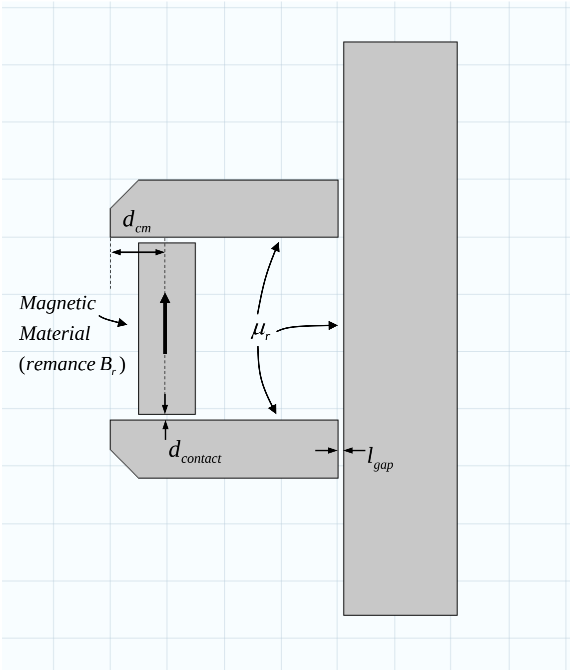

Figure G.3: 2D COMSOL model for parameter sensitivity study.

G.2. Parameter Sensitivity Study

Simulation Setup

To evaluate the sensitivity of the estimated values, a parameter study is performed, using a simplified 2D model of the setup. In this case, we are only interested in a relative change of k_1 and k_2, which we can estimate with a 2D model simulation. This still provides enough accuracy and is computationally much more efficient. The approach to implementing the simulation and evaluating k_1 and k_2 is similar to the 3D case. Figure G.3 shows the simulation model with the parameters varied in the study. These parameters are the most likely to be different in the physical setup than in the simulation. Table G.2 gives an overview of the parameters, their description, and their nominal value.

Parameter	Nominal Value	Comment
B_r	1.2 T	Remanent flux density in axial direction
μ_r	1000	Relative permeability of magnetic circuit material (St.37)
$d_{contact}$	0 mm	Contact spacing between magnet and pole pieces
d_{cm}	12.25 mm	Magnet position with respect to pole pieces
l_g	1 mm	Air-gap width

Table G.2: Nominal values for parameters in sensitivity study.

Results

The sensitivity of k_1 and k_2 on the variation of each parameter is simulated while keeping the rest of the parameters at their nominal values. The results are shown in Figs. G.4 and G.5. All parameters are normalized w.r.t their nominal values. The dotted red lines represent a deviation of $\pm 2\%$ from that nominal value.

Looking at the results, we see that k_1 is only very sensitive to the air-gap width l_g.

The MMF loss factor k_2 obviously changes with the relative permeability of the magnetic circuit components. The lower the circuit permeability, the higher the reluctance and consequently the MMF over

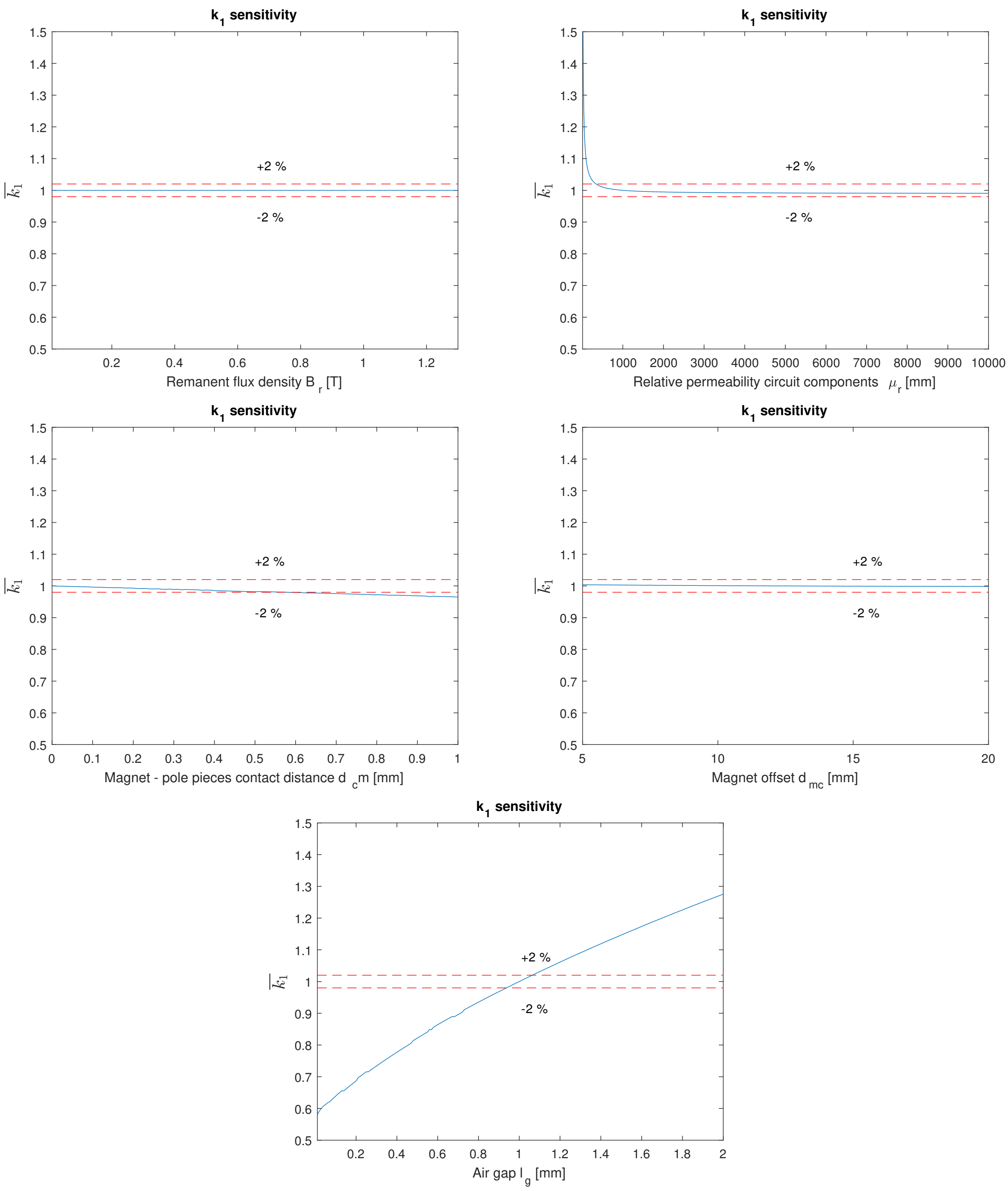

Figure G.4: Sensitivity of k_1 on different parameters, specified in Fig. G.3

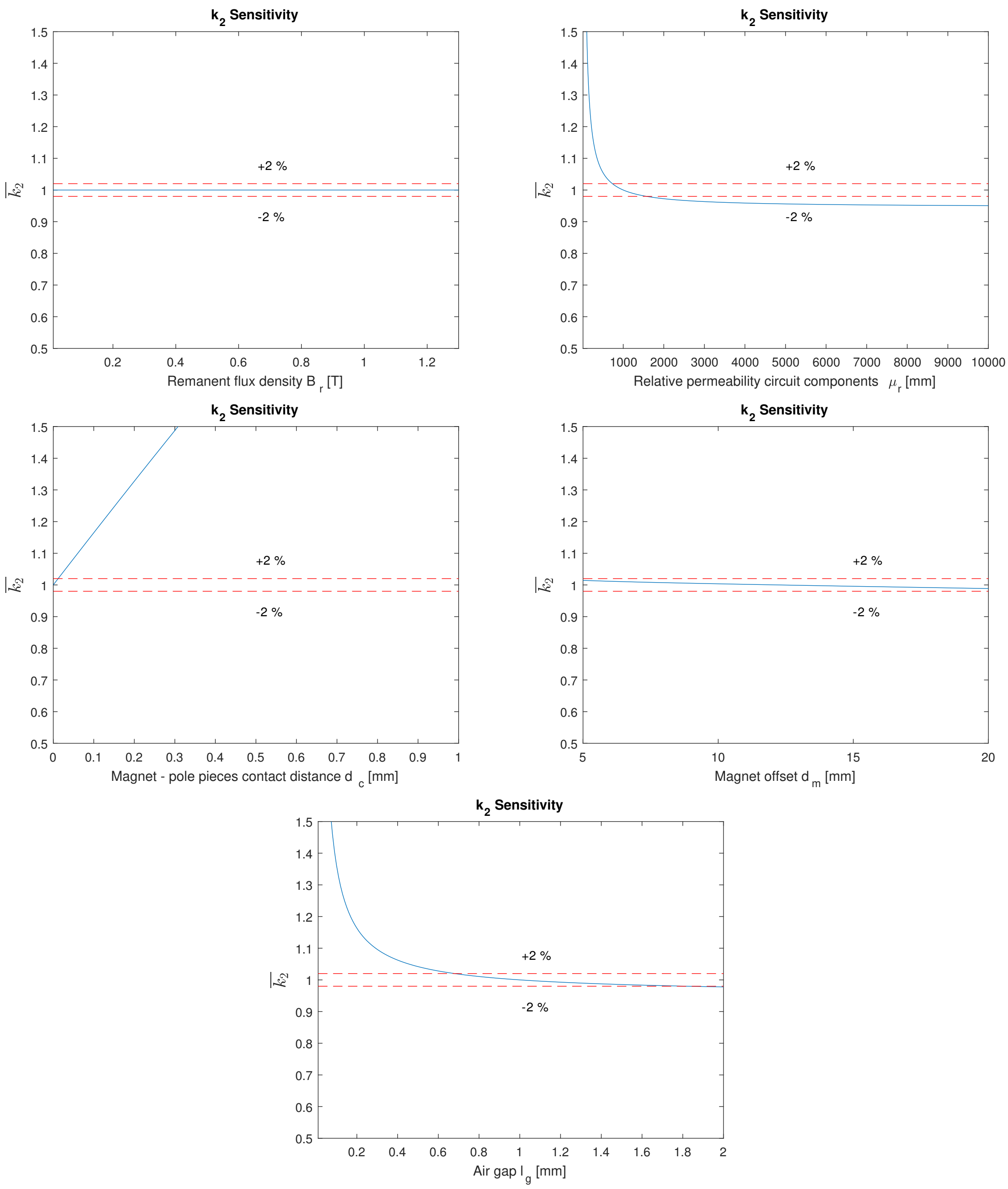

Figure G.5: Sensitivity of k_2 on different parameters, specified in Fig. G.3

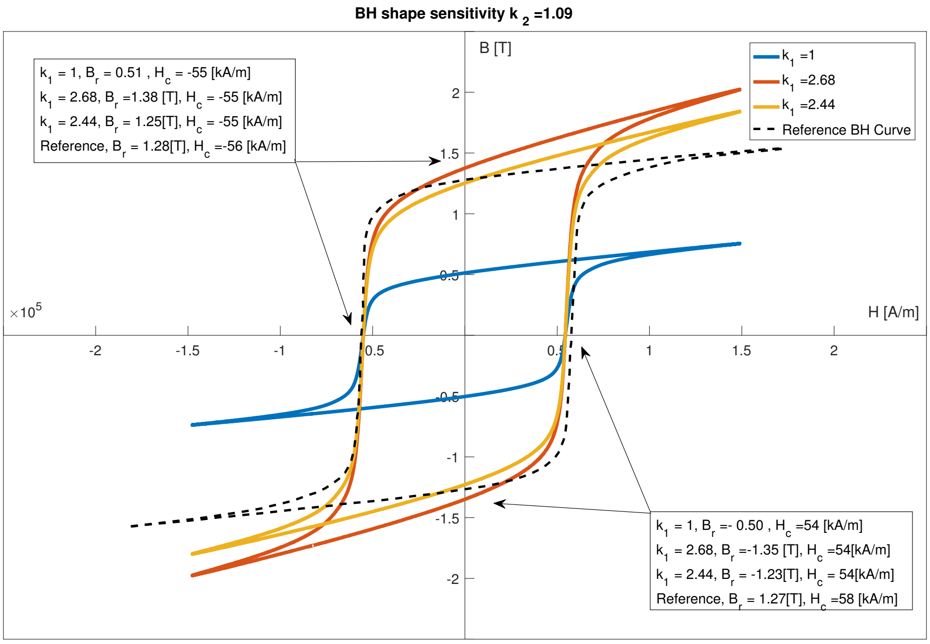

Figure G.6: Estimated AlNiCo 5 hysteresis curves based on measurement data, for different values of k_1 and $k_2 = 1.09$. The reference curve is based on data taken from [7]

each component. However, at some point, the curve levels off. At the nominal value found in literature of $\mu_r = 1000$, k_2 is still quite sensitive to differences between this value and the actual μ_r of the material. The loss factor is also very sensitive to the contact spacing of the pole pieces and the magnet. This is obvious as a non-zero value effectively means an extra air-gap in the circuit. To avoid this effect, the contact surfaces should be as flat as possible and the magnet and pole pieces preferably clamped together.

It must be noted that the sensitivity of k_2 on the air-gap becomes invalid at small values of l_g. Equations (G.6) will go to infinity if l_g approaches zero, and the value of k_2 becomes irrelevant.

G.3. Measurement Based Identification

To validate the identified model, (G.1), (G.2) and (G.3) are used to estimate the AlNiCo 5 BH curve, based on measurements of the coil current I_c and air-gap flux density B_g.

Flux leakage coefficient

Figure G.6 shows these curves for different values of k_1 at $k_2 = 1.09$, together with a reference BH curve from [7]. It is clear that the BH curve estimate using the identified value of $k_1 = 2.68$ does not yield the correct value for B_r. This is to be expected because k_1 is very sensitive to the value of l_g and there is an unavoidable difference in air-gap width l_g between the physical setup and the COMSOL simulation.

Tweaking the flux leakage coefficient to $k_1 = 2.44$, leads to a positive $B_r = 1.25$ and a negative $B_r = -1.23$, which readily correspond to the datasheet value of the specific material used (Tab. E.1). The difference between the positive and negative values is because of a slight asymmetry in the BH curves.

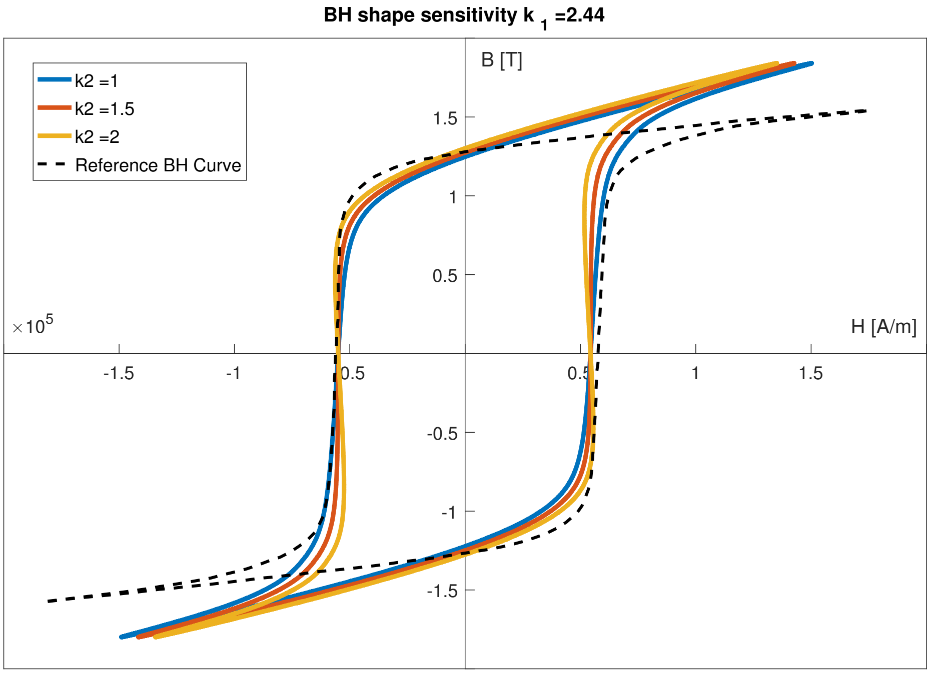

Figure G.7: Estimated AlNiCo 5 hysteresis curves based on measurement data, for different values of k_2 and $k_1 = 2.44$. The reference curve is based on data taken from [7].

MMF loss factor

Analyzing (G.1), (G.2) and (G.3) shows that the value for H_c is not influenced by either k_1 or k_2. Therefore H_c cannot be used as a reference point for identification. This is confirmed by Fig. G.7, which shows estimated BH curves for different k_2, at $k_1 = 2.44$. Increasing the value for k_2 makes the resulting BH curve increasingly skewed, which does not make it match the reference curve better. If anything, the match gets worse. Therefore, this graphical identification method is not suitable to estimate the value of k_2. However, looking at the results of the earlier sensitivity analysis, k_2 is only likely to vary a lot with the contact distance between the AlNiCo magnet and the pole pieces. Since these are clamped together in the measurement setup (App. D), the actual value for k_2 is likely to be similar to the simulation.

General BH curve shape

Comparing the general shape of the estimated BH curves in Figs. G.6 and G.7 with the reference it shows that the estimated curves (with $k \neq 1$) are to steep at positive and negative saturation. This is, however, a limitation imposed by the simplified way of expressing the leakage and fringing flux as being proportional to the magnet flux. To prove this, we write (G.1), (G.2) explicit for the fields in the magnet as:

$$B_m = k_1 \frac{A_g B_g}{A_m} \tag{G.7}$$

$$H_m = NI - k_2 \frac{2 B_g l_g}{\mu_0} \tag{G.8}$$

Calculating the differential of both B_m and H_m with respect to the measured quantities B_g and I yields:

Parameter	COMSOL	Measurement based
AlNiCo 5 setup		
k_1	2.68	2.44
k_2	1.09	1.09

Table G.3: Identified model coeffients

$$dB_m = \frac{\partial B_m}{\partial B_g} dB_g + \frac{\partial B_m}{\partial I} dI = k_1 \frac{A_g}{A_m} dB_g \tag{G.9}$$

$$dH_m = \frac{\partial H_m}{\partial B_g} dB_g + \frac{\partial H_m}{\partial I} dI = \frac{N}{L_m} dI - k_2 \frac{2l_g}{\mu_0 L_m} dB_g \tag{G.10}$$

(G.11)

Next, we take the quotient of both expressions, which gives the slope of the $B_m(H_m)$ curve as a function of the slope of the measured $B_g(I)$ curve. As expected, this slope is proportional to k_1.

$$\frac{dB_m}{dH_m} = k_1 \frac{\frac{A_g}{A_m} \frac{dB_g}{dI}}{\frac{N}{L_m} - k_2 \frac{2l_g}{\mu_0 L_m} \frac{dB_g}{dI}} \tag{G.12}$$

G.4. Conclusion

In this section, the flux leakage factor k_1 and MMF loss factor k_2 for the AlNiCo 5 experimental setup where identified using both magnetic FEA in COMSOL and a graphical method based on measurements. The value for k_1, obtained in COMSOL was refined using measurements, such that the remanence value of the resulting estimated BH curve matched the datasheet value for the AlNiCo 5 used (Tab. E.1). The discrepancy between the obtained value for k_1 in the simulation and the measured data can be explained by its high sensitivity on the air-gap width l_g. The effective air-gap width in the physical system is inevitably different than the value used in the simulation. The value of k_2 cannot be fine-tuned using measurement data. However, it has a lower sensitivity, so the match between the value from COMSOL and the actuator value will be better. The identified values for k_1 and k_2 are listed in Tab.

The general shape of the estimated BH curve does not match reference data from literature [7]. It is to steep in the positive and negative saturation regions. This is caused by the fact that we use a constant value to describe leakage and fringing flux effects. In reality, this is not an accurate description, and the value for k_1 is dependent on, among others, the field intensity H_m.

H

Recommended Literature

The theory describing permanent magnets is already old an well established. This thesis, however, provides only the necessary information to understand the concept of a Tunable Magnet. For more in-depth information on the workings of permanent magnets, from the quantum effects that is ultimately the basis of magnetism to the microscale phenomena that govern hysteresis behavior, a reading list is provided:

- **Permanent magnet materials and their application** - by *Peter Cambell* [8].
  The best introduction to permanent magnets.
- **Permanent Magnet and Electromechanical Devices : Materials, Analysis, and Applications** - by *Edward P. Furlani* [14].
  Also a very good introduction to permanent magnets and their applications.
- **Introduction to magnetic materials** - by *B. D. Cullity, C. D. Graham* [11].
  Good overview of magnetic materials. Provides a complete overview of the different phenomena that govern magnetization dynamics.
- **Magnetic actuators and sensors** - by *John R. Brauer* [4].
  Gives a good description of the transient behavior of magnetic actuators. Including a timeline of the dynamic effects that are involved in magnetizing a magnetic material, and in what order they occur.
- **Hysteresis in magnetism : for physicists, materials scientists, and engineers** - by *Giorgio Bertotti* [3].
  An excellent treatise on the origin of magnetic hysteresis and how to model it. The book is quite theoretical.
- **Electromagnetic devices** - by *H.C. Roters* [52].
  Legendary book from 1944 concerning the design of electromagnetic devices. Describes equations to analytically model flux leakage and fringing effects, that cannot be found elsewhere. The book is still cited in recent literature such as [35].

It is recommended to start with the book by *Peter Cambell*, since it gives a concise but complete, and well-written introduction to permanent magnets.

Material Data

I.1. Steel 37

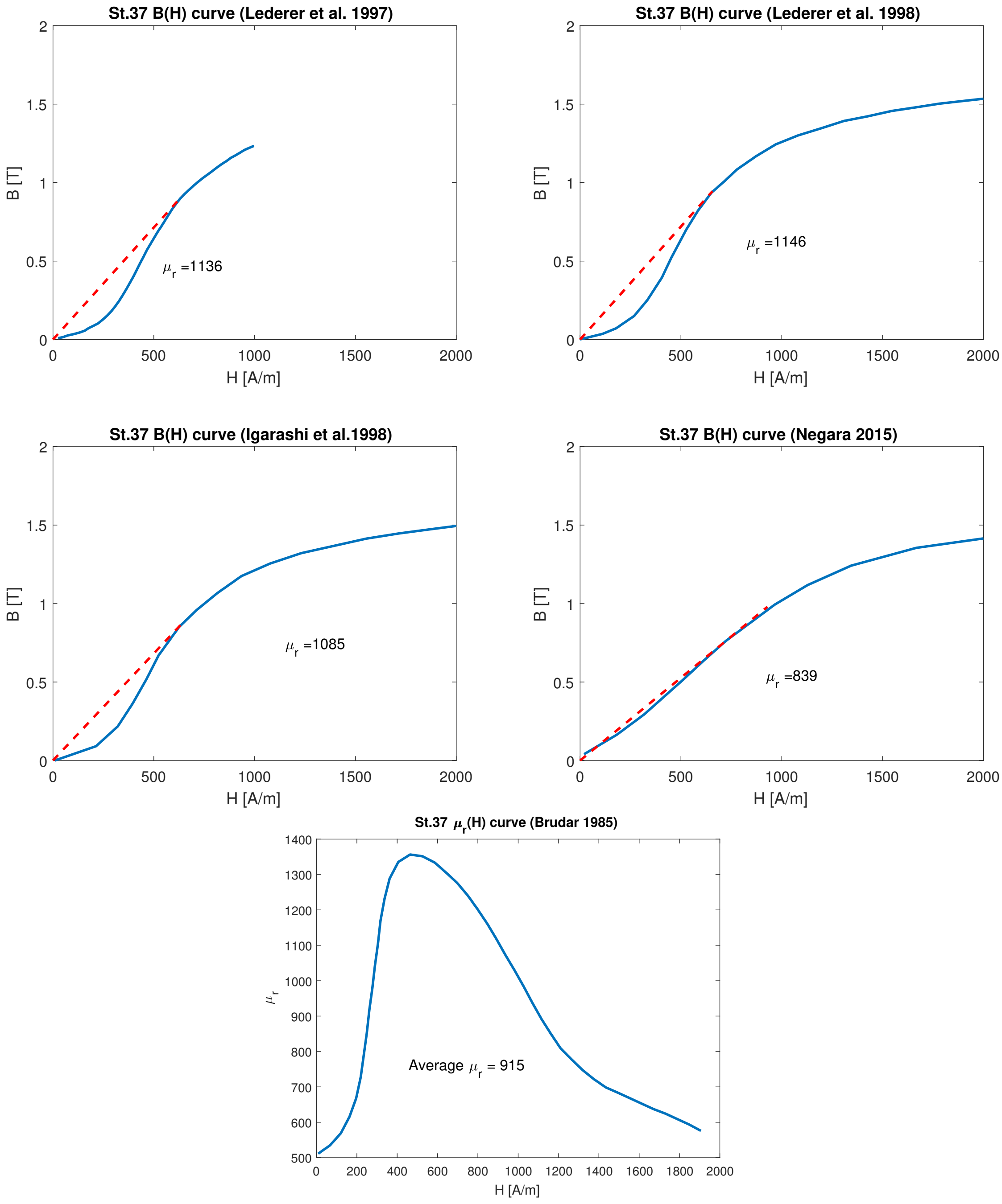

Figure I.1: St.37 magnetization curves from literature to evaluate μ_r [5, 20, 28, 29, 44]

I.2. AlNiCo

Technical Data Sheet - Alnico Magnets

Alnico Magnets

Alnico magnets have the best temperature coefficients of any magnet material.
Alnico magnets should be regarded as the best choice in extremely high temperature applications.
Alnico magnets can be produced by Casting or Sintering. Alnico is also rarely made by Bonding within a binder.
Cast Alnico is the most common form of Alnico magnet. Casting is often used to get "near net shape" Alnico magnets.
Casting Alnico is cost effective for both low and high volume, for small and very large magnets.
Sintered Alnico is cost effective for medium to high volume runs due to tooling cost. The parts are generally small to medium.
Sintered Alnico magnets are not so commonly used due to lower magnetic performance and limitation to simpler shapes.
Anisotropic magnets have the direction of magnetisation (DoM) permanently within the structure and give the maximum performance.
Isotropic magnets can be magnetised in many ways as they have no preferred direction of magnetisation but give reduced performance.
Cast Alnico 5 is the most common grade of Alnico, with the LNG44 variant of Alnico 5 (Alcomax 3) being the most popular.
Alnico5, Alnico 8 and Alnico 9 all exist with several sub-grades with differing performance characteristics.
Where the shape is new, tooling charges may apply. It is common for the magnet pole faces to be machined to finish.
Alnico produced to specific Br, Hc, Hci and BHmax may be possible but at extra cost. Keeping within normal grades is advised.
Custom or bespoke magnet shapes may carry an additional tooling cost and even a minimum order charge.
Alnico Assemblies are also possible.

ECLIPSE MAGNETICS

Anisotropic Cast Alnico

Typical Range of Values

Material	Br		Hc (Hcb)		Hci (Hcj)		BHmax	
	T	kG	kA/m	kOe	kA/m	kOe	kJ/m^3	MGOe
Alnico 5 (Alnico5_LNG34)	1.10	11.0	50	0.63	52	0.65	34	4.25
Alnico 5 (Alnico5_LNG37)	1.18	11.8	50	0.61	51	0.64	37	4.63
Alnico 5 (Alnico5_LNG40)	1.20	12.0	50	0.63	52	0.65	40	5.00
Alnico 5 (Alnico5_LNG44)	1.25	12.5	50	0.65	54	0.68	44	5.50
Alnico 6 (Alnico6_LNG28)	1.15	11.5	58	0.73	60	0.75	28	3.50
Alnico 5DG (Alnico5DG_LNG52)	1.30	13.0	56	0.70	58	0.73	52	6.50
Alnico 5-7 (Alnico5-7_LNG60)	1.35	13.5	58	0.73	60	0.75	60	7.50
Alnico 8 (Alnico8_LNGT38)	0.80	8.0	110	1.38	112	1.4	38	4.75
Alnico 8 (Alnico8_LNGT40)	0.85	8.5	115	1.44	117	1.46	40	5.00
Alnico 8 (Alnico8_LNGT44)	0.90	9.0	115	1.44	117	1.46	44	5.50
Alnico 8HC (Alnico8HC_LNGT36J)	0.72	7.2	150	1.88	152	1.90	36	4.50
Alnico 9 (Alnico9_LNGT60)	1.00	10.0	110	1.38	112	1.4	60	7.50
Alnico 9 (Alnico9_LNGT72)	1.05	10.5	115	1.44	117	1.46	72	9.00
Alnico 9 (Alnico9_LNGT80)	1.08	10.8	120	1.50	122	1.53	80	10.00

Alnico 5 (LNG44) = Alcomax 3 = Alnico 500 = LNG44
Alnico 6 (LNG28) = Alcomax 4 = Alnico 400 = LNG28
Alnico 5DG (LNG52) = Alcomax 3SC = Alnico 600 = LNG52
Alnico 5-7 (LNG60) = Columax = Alnico 700 = LNG60
Alnico 8 (LNGT44) = Hycomax 3 = Alnico 8HE = LNGT44
Alnico 8 (LNGT40) = Hycomax 2 = Alnico 8H = LNGT40
Alnico 8 (LNGT38) = Alnico 8B = LNGT38
Alnico 8HC (LNGT36J) = Alnico 8HC = LNGT36J

Anisotropic Sintered Alnico

Typical Range of Values

Material	Br		Hc (Hcb)		Hci (Hcj)		BHmax	
	T	kG	kA/m	kOe	kA/m	kOe	kJ/m^3	MGOe
Alnico 5 (Alnico5_FLNG34)	1.15	11.5	48	0.60	50	0.63	34	4.25
Alnico 6 (Alnico6_FLNG28)	1.10	11.0	58	0.73	60	0.75	28	3.50
Alnico 8HC (Alnico8HC_FLNG36J)	0.72	7.2	150	1.88	152	1.90	36	4.50
Alnico 8 (Alnico8_FLNGT38)	0.80	8.0	110	1.38	112	1.40	38	4.75
Alnico 8 (Alnico8_FLNGT44)	0.85	8.5	120	1.50	122	1.53	44	5.50
Alnico 8 (Alnico8_FLNGT48)	0.92	9.2	125	1.56	127	1.59	48	5.50

Isotropic Cast Alnico

Typical Range of Values

Material	Br		Hc (Hcb)		Hci (Hcj)		BHmax	
	T	kG	kA/m	kOe	kA/m	kOe	kJ/m^3	MGOe
Alnico 3 (Alnico3_LN10)	0.65	6.5	38	0.48	40	0.50	10	1.25
Alnico 2 (Alnico2_LNG12)	0.75	7.5	45	0.56	46	0.58	12	1.50
Alnico 8 (Alnico8_LNG18)	0.55	5.5	90	1.13	97	1.21	18	2.25

Isotropic Sintered Alnico

Typical Range of Values

Material	Br		Hc (Hcb)		Hci (Hcj)		BHmax	
	T	kG	kA/m	kOe	kA/m	kOe	kJ/m^3	MGOe
Alnico 3 (Alnico3_FLN10)	0.65	6.5	40	0.50	42	0.53	10	1.25
Alnico 2 (Alnico2_FLNG12)	0.75	7.5	45	0.56	46	0.58	12	1.50
Alnico 8 (Alnico8_FLNGT18)	0.60	6.0	95	1.19	98	1.23	18	2.25
Alnico 8 (Alnico8_FLNGT20)	0.62	6.2	100	1.25	105	1.31	20	2.50

Bonded Alnico

Typical Range of Values

Material	Br		Hc (Hcb)		Hci (Hcj)		BHmax	
	T	kG	kA/m	kOe	kA/m	kOe	kJ/m^3	MGOe
Alnico_BLN7	0.31	3.1	79	1.00	103	0.85	6.77	0.86
Alnico_BLN8	0.34	3.4	83	1.05	107	1.00	7.96	1.00

Physical Characteristics (Typical)

Characteristic	Symbol	Unit	Value
Density	D	g/cc	6.9-7.3
Vickers Hardness	Hv	D.P.N	520-700
Curie Temperature	Tc	°C	800
Compression Strength	C.S	N/mm^2	300-400
Coefficient of Thermal Expansion	C//	10^{-6}/°C	11.5-13
	C⊥	10^{-6}/°C	11.5-13
Electrical Resistivity	ρ	μ Ω.cm	45-70
Tensile Strength	σ_{UTS} or S_U	x10^6 Pa	20-450 (37 LNG44)
Hardness		Rockwell	45-55
Curie Temperature	Tc	°C	810-860

Max Working Temperature
(Please note - your application will affect the performance available)

Material	Maximum recommended temperature
Alnico 2	450 degrees C
Alnico 3	450 degrees C
Alnico 5	525 degrees C
Alnico 6	525 degrees C
Alnico 5DG	525 degrees C
Alnico 5-7	525 degrees C
Alnico 8	550 degrees C
Alnico 8HC	550 degrees C
Alnico 9	550 degrees C
Bonded Alnico	150-200 degrees C (binder limiting)

Corrosion Resistance

Alnico is regarded as having very good to excellent corrosion resistance for most applications.
Because iron exists within the Alnico alloy, corrosion may be seen during prolonged exposure to water.
Alnico can be coated or painted (e.g. Red Paint) but this is often only for aesthetic purposes.

Temperature coefficients

Rev.Temp.Coef. of Induction (Br), α, %/°C	Rev.Temp.Coef. of Intrinsic Coercivity (Hci), β, %/°C
-0.03 (Alnico 2, Cast)	-0.02 (Alnico 2, Cast)
-0.035 (Alnico 2, Sintered)	-0.025 (Alnico 2, Sintered)
-0.035 (Alnico 3, Cast)	-0.025 (Alnico 3, Cast)
-0.03 (Alnico 3, Sintered)	-0.02 (Alnico 3, Sintered)
-0.02 (Alnico 5, Cast and Sintered)	+0.01 (Alnico 5, Cast and Sintered)
-0.02 (Alnico 6, Cast and Sintered)	+0.03 (Alnico 6, Cast and Sintered)
-0.02 (Alnico 5DG, Cast)	+0.03 (Alnico 5DG, Cast)
-0.02 (Alnico 5-7, Cast)	+0.03 (Alnico 5-7, Cast)
-0.025 (Alnico 8, Cast and Sintered)	+0.01 (Alnico 8, Cast and Sintered)
-0.025 (Alnico 8HC, Cast and Sintered)	+0.01 (Alnico 8HC, Cast and Sintered)
-0.025 (Alnico 9, Cast and Sintered)	+0.01 (Alnico 9, Cast and Sintered)

Example Alnico second quadrant demagnetisation BH curve

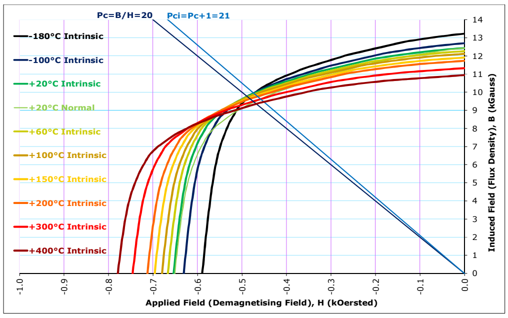

Additional Information

The magnet shape, its environment, and the actual application affect how the Alnico magnet will perform.
The Intrinsic curve (not the Normal curve, although similar in shape for Alnico) is needed to assist in determining magnet suitability.
For Alnico, it is important to keep the working point above the "knee" of the Intrinsic curve to avoid severe demagnetisation.
Rotating machines and generators using Alnico need careful design due to the varying air gap during rotor rotation.
We can assist in designing in resistance to demagnetisation. We can guide you with your design options.
A length to diameter (L/D) ratio of at least 4 or 5 is a rule of thumb guide when using Alnico. A high L/D ratio is important for resisting demagnetising.
External demagnetising factors such as other magnets and electromagnets must be taken into account. They will put a field onto the magnet risking demagnetising it.
Even pushing two Alnico magnets in repulsion into each other can weaken their output. However careful handling will quickly resolve this. Alnico can be remagnetised.
The risk of demagnetisation of Alnico is reduced by improving the working point (e.g. use a longer magnet, increase the L/D ratio, use a higher Hc, introduce magnetic steel to the circuit, etc).
Alnico magnets have the best temperature coefficients of any magnet type. Alnico has the least change in field output over a change in temperature. They can also operate at the highest temperatures of any magnet.
Cast Alnico can have a blackened surface - this is the "As Cast" finish with the surface texture coming from the sand cast mold. Machining of the Alnico (e.g. precision ground pole faces) leaves a bright silvery metallic finish.
Very small air holes may be seen from time to time within the structure of cast Alnico magnets. This is natural for cast magnets (due to the casting process) and cannot be avoided.
If you have any more questions, require technical assistance and would like a quotation, simply contact us.
Although we have made every attempt to provide accurate information, we do reserve the right to change any of the information in this document without notice.
We cannot accept any responsibility or liability for any errors or problems caused by using any of the information provided.

www.eclipsemagnetics.com
sales@eclipsemagnetics.com
Tel: +44 (0)114 225 0600
Fax: +44 (0)114 225 0610

Figure I.2: AlNiCo material datasheet from [12].

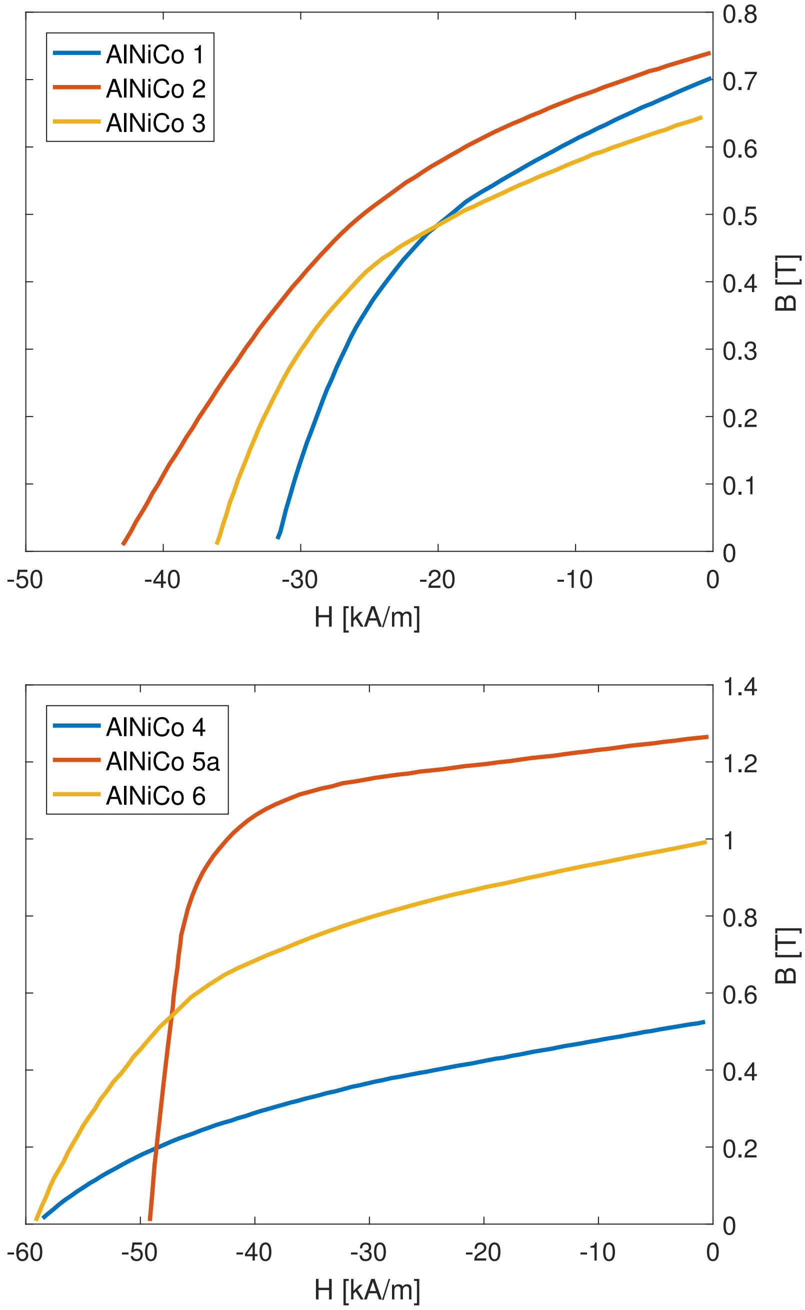

Figure I.3: Demagnetization curves of AlNiCo 1 t/m 6. Data from [62].

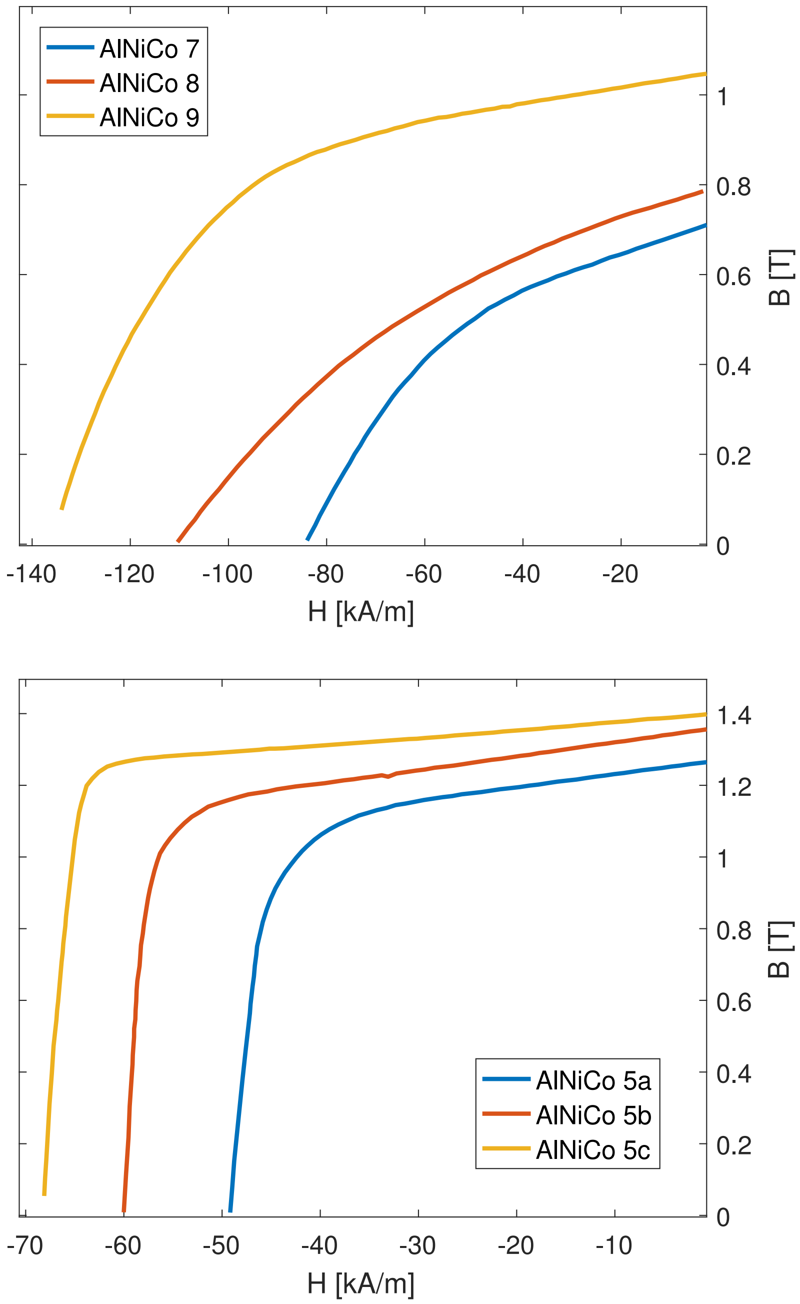

Figure I.4: Demagnetization curves of AlNiCo 5a, 5b, 5c and 7 t/m 9. Data from [62].

Bibliography

[1] D. K. Abeywardana, A. P. Hu, and Z. Salcic. Electropermanent magnet based wireless microactuator for microfluidic systems: Actuator control and energy consumption aspects. In *2016 IEEE SENSORS*, pages 1–3. IEEE, 10 2016.

[2] Asensor Technology AB. Linear High Precision Analog Hall Sensors.

[3] Giorgio. Bertotti. *Hysteresis in Magnetism : For Physicists, Materials Scientists, and Engineers.* Elsevier Science, 1998.

[4] John R Brauer. *Magnetic Actuators and Sensors*. Wiley-IEEE Press, 2006. ISBN 9780471731696.

[5] B. Brudar. Magnetic leakage fields calculated by the method of finite differences. *NDT International*, 18(6):353–357, 1985. doi: 10.1016/0308-9126(85)90166-X.

[6] Jan Bydžovský, Mojmír Kollár, Klement Ondreička, and Jozef Paľa. Design and Experimental Examination of New Type of Electro-Permanent Magnetic Chuck. *Journal of ELECTRICAL ENGINEERING*, 61(7):152–155, 2010.

[7] P. Campbell and S. Al-Murshid. A model of anisotropic Alnico magnets for field computation. *IEEE Transactions on Magnetics*, 18(3):898–904, 1982.

[8] Peter Campbell. *Permanent Magnet Materials and their Design*. Cambridge University Press, 1994. ISBN 052124996.

[9] Chunhua Liu, K. T. Chau, and Chun Qiu. Design and Analysis of a New Magnetic-Geared Memory Machine. *IEEE Transactions on Applied Superconductivity*, 24(3):1–5, 6 2014.

[10] Bruno Cugny, Nikos Karafolas, Zoran Sodnik, S Kuiper, N Doelman, T Overtoom, E Nieuwkoop, T Russchenberg, M Van Riel, J Wildschut, M Baeten, H Spruit, S Brinkers, and J Human. Electromagnetic deformable mirror for space applications. In *International Conference on Space Optics—ICSO 2016*, volume 10562. International Society for Optics and Photonics, 2016.

[11] B. D. Cullity and C. D. Graham. *Introduction to Magnetic Materials.* Wiley, 2011. ISBN 9781118211496.

[12] Eclips Magnetics. Technical Data Sheet - AlNiCo Magnets. Technical report. URL `www.eclipsemagnetics.com`.

[13] Fuhua Li, K. T. Chau, Chunhua Liu, J. Z. Jiang, and Winson Yong Wang. Design and Analysis of Magnet Proportioning for Dual-Memory Machines. *IEEE Transactions on Applied Superconductivity*, 22(3):4905404–4905404, 6 2012.

[14] Edward P. Furlani. *Permanent Magnet and Electromechanical Devices*. Elsevier Science, 1 edition, 2001. ISBN 9780122699511.

[15] Abel Gawel, Mina Kamel, Tonci Novkovic, Jakob Widauer, Dominik Schindler, Benjamin Pfyffer Von Altishofen, Roland Siegwart, and Juan Nieto. Aerial picking and delivery of magnetic objects with MAVs. In *Proceedings - IEEE International Conference on Robotics and Automation*, pages 5746–5752. IEEE, 2017.

[16] Harrison Weber. The dream of Ara: Inside the rise and fall of the world's most revolutionary phone, 2017. URL `https://venturebeat.com/2017/01/10/inside-project-ara-googles-revolutionary-modular-phone/`.

[17] Thorsten Hüfner, Oliver Radler, Tom Ströhla, Thomas Sattel, Jasper Wesselingh, Alexander Vogler, and Dirk Eicher. A note on electromagnetic gravity compensation actuators based on soft electro- permanent magnets for adjustable reluctance force. In *17th International EUSPEN Conference Proceedings*, Hannover, 2017. EUSPEN. URL `www.euspen.eu`.

[18] S.Y.R. Hui and J. Zhu. Numerical modelling and simulation of hysteresis effects in magnetic cores using transmission-line modelling and the Preisach theory. *IEE Proceedings - Electric Power Applications*, 142(1):57–62, 1995.

[19] S.Y.R. Hui, J.G. Zhu, and V.S. Ramsden. A generalized dynamic circuit model of magnetic cores for low- and high-frequency applications. II. Circuit model formulation and implementation. *IEEE Transactions on Power Electronics*, 11(2):251–259, 3 1996.

[20] H Igarashi, D Lederer, A Kost, T Honma, and T Nakata. A numerical investigation of Preisach and Jiles models for magnetic hysteresis. *COMPEL – The International Journal for Computation and Mathematics in Electrical and Electronic Engineering*, 173(12):357–363, 1998.

[21] Ram V. Iyer and Xiaobo Tan. Control of hysteretic systems through inverse compensation. *IEEE Control Systems*, 29(1):83–99, 2 2009.

[22] D C Jiles and D L Atherton. Theory of ferromagnetic hysteresis. *Journal of Magnetism and Magnetic Materials*, 61(1-2):48–60, 9 1986.

[23] Winfried Kaiser and Peter Kuerz. EUVL - Extreme Ultraviolet Lithography. *Optik & Photonik, Wiley-VCH Verlag*, 2008.

[24] Pavel Kirienko. NicaDrone OpenGrab EPM v3, 2018. URL `https://docs.zubax.com/opengrab_epm_v3`.

[25] ARA KNAIAN and NEIL GERSHENFELD. Electropermanent magnet-based motors, 2014. URL `https://patents.google.com/patent/US8674576`.

[26] Ara Nerses Knaian. *Electropermanent magnetic connectors and actuators : devices and their application in programmable matter*. PhD thesis, Massachusetts Institute of Technology, 2010.

[27] Stefan Kuiper, Niek Doelman, Evert Nieuwkoop, Ton Overtoom, Tjeerd Russchenberg, Martijn van Riel, Justin Wildschut, Max Baeten, Jet Human, Helma Spruit, Sanneke Brinkers, and Matthew Maniscalco. Electromagnetic deformable mirror development at TNO. In *Proc.SPIE*, pages 9912 – 9912 – 7, 2016.

[28] Dieter Lederer and Arnulf Kost. Modelling of Nonlinear Magnetic Material using a Complex Effective Reluctivity. *IEEE TRANSACTIONS ON MAGNETICS*, 34(5):3060–3063, 1998.

[29] Dieter Lederer, Hajime Igarashi, and Arnulf Kost. Modelling of Nonlinear Magnetic Material using an Effective Permeability Comparison between Different Formulations. 1997.

[30] Wenlong Li, K.T. Chau, Christopher H.T. Lee, T.W. Ching, Mu Chen, and J.Z. Jiang. A new linear magnetic gear with adjustable gear ratios and its application for direct-drive wave energy extraction. *Renewable Energy*, 105:199–208, 5 2017.

[31] LION PRECISION. Understanding Sensor Resolution Specifications and Performance. Technical report, 2014. URL `http://www.lionprecision.com/tech-library/technotes/article-0010-sensor-resolution.html`.

[32] Chunhua Liu and K. T. Chau. Electromagnetic design of a new electrically controlled magnetic variable-speed gearing machine. *Energies*, 7(3):1539–1554, 2014.

[33] E A Lomonova. Advanced Actuation Systems -State of the Art: Fundamental and Applied Research. In *International Conference on Electrical Machines and Systems (ICEMS), 2010*, pages 13–24, Incheon, 2010. IEEE.

[34] Ian MacKenzie and David L. Trumper. Real-Time Hysteresis Modeling of a Reluctance Actuator Using a Sheared-Hysteresis-Model Observer. *IEEE/ASME Transactions on Mechatronics*, 21(1): 4–16, 2016.

[35] Ian Ross Mackenzie. *Design and control methods for high-accuracy variable reluctance actuators*. PhD thesis, Massachusetts Institute of Technology, 2015.

[36] Adrew D Marchese. *Controlling the Locomotion of a Separated Inner Robot from an Outer Robot using Electropermanent Magnets*. PhD thesis, Massachesetts Institute of Technology, 2012.

[37] Andrew D. Marchese, Cagdas D. Onal, and Daniela Rus. Soft robot actuators using energy-efficient valves controlled by electropermanent magnets. In *2011 IEEE/RSJ International Conference on Intelligent Robots and Systems*, pages 756–761. IEEE, 9 2011.

[38] Andrew D. Marchese, Harry Asada, and Daniela Rus. Controlling the locomotion of a separated inner robot from an outer robot using electropermanent magnets. In *2012 IEEE International Conference on Robotics and Automation*, pages 3763–3770. IEEE, 5 2012.

[39] Isaak D Mayergoyz. *Mathematical models of hysteresis and their applications*. Academic Press, 2003.

[40] Thomas Moennig. Optical element housing or mounting connector, 4 2001. URL `https://patents.google.com/patent/US6445515B2/en`.

[41] N. Mohan and T.M Undeland. *Power electronics: converters, applications, and design*. John Wiley & Sons, 2007.

[42] Mu Chen, K. T. Chau, Wenlong Li, Chunhua Liu, and Chun Qiu. Design and Analysis of a New Magnetic Gear With Multiple Gear Ratios. *IEEE Transactions on Applied Superconductivity*, 24 (3):1–4, 6 2014.

[43] R. Munnig Schmidt, G. Schitter, A. Rankers, and J. Van Eijk. *The Design of High Performance Mechatronics*. Ios Press, 2nd edition, 2014.

[44] I. M. Yulistya Negara, Dimas A. Asfani, Daniar Fahmi, Shandy Baskoro, and Arief K. Budi. Materials and Cutting Method Effects of Three Phase Transformer-Core on Magnetization Curve and Inrush Current: Simulation Approach. *International Review on Modelling and Simulations (IREMOS)*, 8(3):370–376, 2015.

[45] Francisco Ochoa-Cardenas and Tony J. Dodd. Design of an active magnetic wheel with a varying Electro-Permanent Magnet adhesion mechanism. In *IEEE International Conference on Intelligent Robots and Systems*, pages 3340–3345. IEEE, 2015.

[46] V. Ostovic. Memory motors-a new class of controllable flux PM machines for a true wide speed operation. In *Conference Record of the 2001 IEEE Industry Applications Conference. 36th IAS Annual Meeting*, volume 4, pages 2577–2584. IEEE, 2001.

[47] Richard Owen, Z. Q. Zhu, J. B. Wang, D. A. Stone, and I. Urquhart. Review of variable-flux permanent magnet machines. In *2011 International Conference on Electrical Machines and Systems*, pages 1–6. IEEE, 8 2011.

[48] José I Padovani, Stefanie S Jeffrey, and Roger T Howe. Electropermanent magnet actuation for droplet ferromicrofluidics. *Technology*, 4(2):110–119, 6 2016.

[49] Dominic F Pignataro. Electrically Switchable Magnet System, 2001.

[50] Pololu Corporation. Pololu G2 High-Power Motor Driver 24v21. URL `https://www.pololu.com/product/2995`.

[51] F. Preisach. Über die magnetische Nachwirkung. *Zeitschrift für Physik*, 94(5-6):277–302, 5 1935.

[52] Herbert C. Roters. *Electromagnetic Devices*. Willey, 1941.

[53] SGM Magnetics Corporation. Electro Permanent Lifting Magnets. URL http://sgmmagnets.com/1/electrop.html.

[54] Texas Instruments Incorporated. OPA549 - High-Voltage, High-Current Op Amp. URL http://www.ti.com/product/OPA549.

[55] Thorlabs Inc. Thorlabs Linear Translation Stage, 2018. URL https://www.thorlabs.com/thorproduct.cfm?partnumber=XR25C/M.

[56] Josef Tugwell, Philip Brennan, Conor OShea, Kilian ODonoghue, Timothy Power, Michael OShea, James Griffiths, Ronan Cahill, and Padraig Cantillon-Murphy. Electropermanent Magnetic Anchoring for Surgery and Endoscopy. *IEEE Transactions on Biomedical Engineering*, 62(3):842–848, 3 2015.

[57] Silvan G. Vietor, Spronck Jo W., and S. Hassan HosseinNia. Tunable Magnets: modeling and validation for dynamic and precision applications. Master's thesis, Delft University of Technology, 2018.

[58] N. H. Vrijsen, J. W. Jansen, and E. A. Lomonova. Comparison of linear voice coil and reluctance actuators for high-precision applications. In *Proceedings of EPE-PEMC 2010 - 14th International Power Electronics and Motion Control Conference*, pages 6–8, 2010.

[59] Qingsong Wang and Shuangxia Niu. Electromagnetic design and analysis of a novel fault-tolerant flux-modulated memory machine. *Energies*, 8(8):8069–8085, 2015.

[60] Peter Ward and Dikai Liu. Design of a high capacity Electro Permanent Magnetic adhesion for climbing robots. In *IEEE International Conference on Robotics and Biomimetics (ROBIO)*, pages 217–222. IEEE, 2012.

[61] J Wesselingh. Anordnung zur Halterung eines Bauteils in einer Lithographieanlage sowie Lithographieanlage, 7 2015. URL https://google.com/patents/DE102015201096A1.

[62] E. P. Wohlfarth. *Ferromagnetic Materials Volume 3*. North-Holland Publishing Company, 1982. ISBN 0444863788.

[63] Chuang Yu and K. T. Chau. Design, Analysis, and Control of DC-Excited Memory Motors. *IEEE Transactions on Energy Conversion*, 26(2):479–489, 6 2011.

[64] Chuang Yu, K. T. Chau, Xinhua Liu, and J. Z. Jiang. A flux-mnemonic permanent magnet brushless motor for electric vehicles. *Journal of Applied Physics*, 103(7):07F103, 4 2008.